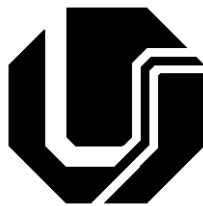# LEANDRO JOÃO DA SILVA

NEAR-IMMERSION ACTIVE COOLING
FOR WIRE + ARC ADDITIVE MANUFACTURING:
FROM CONCEPT TO APPLICATION

UNIVERSIDADE FEDERAL DE UBERLÂNDIA
FACULDADE DE ENGENHARIA MECÂNICA
2019

LEANDRO JOÃO DA SILVA

NEAR-IMMERSION ACTIVE COOLING FOR WIRE + ARC ADDITIVE MANUFACTURING: FROM CONCEPT TO APPLICATION

Thesis submitted to the Post-Graduation Program in Mechanical Engineering of the Federal University of Uberlândia as part of the requirements for obtaining the degree in **DOCTOR OF MECHANICAL ENGINEERING.**

Concentration area: Materials and Manufacturing Processes

Supervisor: Prof. Américo Scotti, Ph.D.
Co-supervisor: Prof. Ruham Pablo Reis, Dr. Eng.

UBERLÂNDIA - MG
2019

UNIVERSIDADE FEDERAL DE UBERLÂNDIA
Coordenação do Programa de Pós-Graduação em Engenharia Mecânica
Av. João Naves de Ávila, nº 2121, Bloco 1M, Sala 212 - Bairro Santa Mônica, Uberlândia-MG, CEP 38400-902
Telefone: (34) 3239-4282 - www.posgrad.mecanica.ufu.br - secposmec@mecanica.ufu.br

ATA DE DEFESA - PÓS-GRADUAÇÃO

Programa de Pós-Graduação em:	Engenharia Mecânica
Defesa de:	Tese de Doutorado, nº 280, COPEM
Data:	vinte e cinco de outubro de dois mil e dezenove — Hora de início: 14:00 — Hora de encerramento: 17:00
Matrícula do Discente:	11523EMC006
Nome do Discente:	Leandro João da Silva
Título do Trabalho:	NEAR-IMMERSION ACTIVE COOLING FOR WIRE+ARC ADDITIVE MANUFACTURING: FROM CONCEPT TO APPLICATION
Área de concentração:	Materiais e Processos de Fabricação
Linha de pesquisa:	Processos de Fabricação (Usinagem e Soldagem)
Projeto de Pesquisa de vinculação:	Manufatura aditiva por processos a arco

Reuniu-se na Sala 206 - Bloco 1M, Campus Santa Mônica, da Universidade Federal de Uberlândia, a Banca Examinadora, designada pelo Colegiado do Programa de Pós-graduação em Engenharia Mecânica, assim composta: Professores Doutores: Luís Gonzaga Trabasso - ISI/Joinville; Reginaldo Teixeira Coelho - USP/São Carlos; Louriel Oliveira Vilarinho - FEMEC/UFU; Wisley Falco Sales - FEMEC/UFU; Ruham Pablo Reis (coorientador) - FEMEC/UFU; Américo Scotti- FEME C/UFU, orientador do candidato.

Iniciando os trabalhos o presidente da mesa, Dr. Américo Scotti apresentou a Comissão Examinadora e o candidato, agradeceu a presença do público, e concedeu ao Discente a palavra para a exposição do seu trabalho. A duração da apresentação do Discente e o tempo de arguição e resposta foram conforme as normas do Programa.

A seguir o senhor(a) presidente concedeu a palavra, pela ordem sucessivamente, aos(às) examinadores(as), que passaram a arguir o(a) candidato(a). Ultimada a arguição, que se desenvolveu dentro dos termos regimentais, a Banca, em sessão secreta, atribuiu o resultado final, considerando o(a) candidato(a):

Aprovado.

Esta defesa faz parte dos requisitos necessários à obtenção do título de Doutor.

O competente diploma será expedido após cumprimento dos demais requisitos, conforme as normas do Programa, a legislação pertinente e a regulamentação interna da UFU.

Nada mais havendo a tratar foram encerrados os trabalhos. Foi lavrada a presente ata que após lida e achada conforme foi assinada pela Banca Examinadora.

Documento assinado eletronicamente por **Américo Scotti**, **Professor(a) do Magistério Superior**, em 25/10/2019, às 17:24, conforme horário oficial de Brasília, com fundamento no art. 6º, § 1º, do Decreto nº 8.539, de 8 de outubro de 2015.

Documento assinado eletronicamente por **Reginaldo teixeira coelho**, **Usuário Externo**, em 25/10/2019, às 17:30, conforme horário oficial de Brasília, com fundamento no art. 6º, § 1º, do Decreto nº 8.539, de 8 de outubro de 2015.

Documento assinado eletronicamente por **Luís Gonzaga Trabasso**, **Usuário Externo**, em 25/10/2019, às 17:31, conforme horário oficial de Brasília, com fundamento no art. 6º, § 1º, do Decreto nº 8.539, de 8 de outubro de 2015.

Documento assinado eletronicamente por **Wisley Falco Sales**, **Professor(a) do Magistério Superior**, em 25/10/2019, às 17:31, conforme horário oficial de Brasília, com fundamento no art. 6º, § 1º, do Decreto nº 8.539, de 8 de outubro de 2015.

Documento assinado eletronicamente por **Louriel Oliveira Vilarinho**, **Professor(a) do Magistério Superior**, em 25/10/2019, às 17:32, conforme horário oficial de Brasília, com fundamento no art. 6º, § 1º, do Decreto nº 8.539, de 8 de outubro de 2015.

Referência: Processo nº 23117.092987/2019-97 SEI nº 1649665

It is said that even before a river falls into the ocean,
it trembles with fear.
It looks back at the whole journey, the peaks of the mountains,
the long winding path through the forests,
through the people, and it sees in front of it such a vast ocean that
entering into it is nothing but disappearing forever.
But there is no other way.
The river cannot go back. No one can go back.
Going back is impossible in existence;
you can only go forward.
The river has to take the risk and go into the ocean.
And only when it enters the ocean will the fear disappear
because only then will the river know that it is not disappearing
into the ocean; rather, it is becoming the ocean.
It is a disappearance from one side
and it is a tremendous resurrection on the other side.
So are we. We can only go forward and take risks.
Be brave!! Go on and become an ocean.

The river and the ocean – Osho

Acknowledgments

As Frank Sinatra would say "*And now the end is near*" and so this is the time to remember those who have helped me throughout this journey and thank. First, I would like to express my sincere gratitude to my supervisors Prof. Américo Scotti and Prof. Ruham Pablo Reis. Scotti, you have been great in setting up the theme and helping with the aims of my thesis, and I have received much inspiration from the heights of your immense experience and knowhow. Ruham, your daily contribution/motivation has been priceless. I would also like to express my appreciation to all colleagues at Federal University of Uberlândia, who have made many valuable suggestions and helped with constructive collaborations. I am also indebted to all staff of the SENAI Innovation Institute for Manufacturing Systems and Laser Processing in Joinville.

I would also like to thank the Brazilian Coordination for the Improvement of Higher Education Personnel (CAPES) for the award of a scholarship through Finance Code 001, and the Brazilian National Council for Scientific and Technological Development (CNPq) for the grants 302863/2016-8 and 315092/2018-1. Also, I would like to thank Fronius for the CMT Advanced equipment (Stephan Egerland, Ph.D.), Airbus for the Scalmalloy® wire (Frank Palm, Ph.D.) and White Martins Praxair for the technical support and for providing the shielding gases used (Marcos Lobato, Eng.).

I would also like to express my appreciations to the referees for their availability and valuable contributions to the improvement of this thesis.

Finally, and in the foremost place, I would like to express my enormous gratitude to my wonderful family. Without your support I would be nowhere near to where I am now, from both the professional and personal points of view.

SILVA, L. J. **Near-immersion active cooling for wire + arc additive manufacturing: from concept to application.** 2019. 116 p. Thesis (Doctorate in Mechanical Engineering), Federal University of Uberlândia, Uberlândia, Brazil.

ABSTRACT

Under the fundamental question on how to mitigate heat accumulation in Wire + Arc Additive manufacturing (WAAM), without compromising the part performance and the production time, it was raised an hypothesis that if the preform is deposited near-immersed in water then heat accumulation would be uniformly mitigated, provided that the water evaporation neither destabilize the process nor increase porosity. Therefore, the core objective of this thesis was to answer the fundamental question by proofing the raised hypothesis. To reach this objective, the strategy was to work based on the Technology Readiness Levels – TRLs (ISO 16290), starting with the establishment of what was called Near-immersion Active Cooling (NIAC) concept (TRL 1-2), followed by the NIAC proof of concept (TRL 2-3), moving on to the development of a functional prototype for the NIAC application and for the elaboration of a parameter selection procedure for WAAM with the NIAC (TRL 3-4), and finally reaching the stage of assessment of the NIAC in a relevant environment through deposition of Scalmalloy® preforms (TRL 4-5). The experimental approach was based on single-pass multi-layer walls deposited with CMT process. The results showed that the NIAC technique allowed significant real-time cooling of the preforms. The interpass temperature is kept low and unchanged independently of the preform height. There was no measurable increase in porosity due to use of water cooling. The parameter selection procedure proposed and validated allowed an adequacy based on surface quality. Suitable Scalmalloy® preforms were produced by WAAM and with better productivity with the NIAC. The flat hardness profiles revealed along the building height indicated that material overaging did not take place on WAAM of such alloy. Moreover, the hardness levels increased significantly on heat-treated samples, indicating that Sc was retained in a supersaturated solid solution during deposition. It was concluded that the NIAC technique is able to mitigate heat accumulation in WAAM of aluminum and, thus, to potentially cope with the related drawbacks.

Keywords: Directed Energy Deposition; WAAM; Cold Metal Transfer; Thermal Management; Aluminum; Heat Accumulation; and Active Cooling.

SILVA, L. J. **Resfriamento ativo por quase-imersão para manufatura aditiva por deposição a arco: do conceito à aplicação.** 2019. 116 f. Tese (Doutorado em Engenharia Mecânica), Universidade Federal de Uberlândia, Uberlândia, Brasil.

RESUMO

Sob a questão fundamental de como mitigar o acúmulo de calor na Manufatura Aditiva por Deposição a Arco (MADA), levantou se a hipótese de que se a pré-forma for depositada quase imersa em água então o acúmulo de calor seria uniformemente mitigado, desde que a evaporação da água não desestabilizasse o processo e tampouco aumentasse o nível de porosidade. Portanto, o objetivo geral desta tese foi responder à questão fundamental por meio da comprovação da hipótese levantada. Para alcançar esse objetivo, a estratégia foi trabalhar com base nos níveis de maturidade tecnológica - TRLs (ISO 16290), começando pelo conceito do que foi chamado de Resfriamento Ativo por Quase-Imersão (RAQUI) (TRL 1-2), seguido pela prova de conceito do RAQUI (TRL 2-3), passando para o desenvolvimento de um protótipo funcional e para a elaboração de um procedimento de seleção de parâmetros de deposição (TRL 3-4), e atingindo o estágio de avaliação do NIAC em um ambiente relevante através da deposição de pré-formas de Scalmalloy® (TRL 4-5). A aplicação do RAQUI resultou em um resfriamento significativo das pré-formas em tempo real. A temperatura de interpasse é mantida baixa e imutável independentemente da altura da pré-forma. Não houve aumento significativo de porosidade devido ao emprego de resfriamento com água. O procedimento de seleção de parâmetros proposto e validado permitiu uma adequação baseada na qualidade da superfície. Pré-formas adequadas de Scalmalloy® foram produzidas por MADA e com melhor produtividade com o RAQUI. Os perfis de durezas planos revelados ao longo da altura de construção indicaram que não ocorreu superenvelhecimento da pré-formas durante a deposição de tal liga. Além disso, os níveis de dureza aumentaram significativamente após tratamento térmico. Concluiu-se que a técnica NIAC é capaz de mitigar o acúmulo de calor em MADA de alumínio e, assim, lidar com os inconvenientes relacionados.

Palavras-Chave: Deposição com Energia Direcionada; Manufatura Aditiva por Deposição a Arco; CMT; Alumínio; Gerenciamento Térmico; Acúmulo de calor; e Resfriamento Ativo.

Nomenclature

AM	Additive Manufacturing
BLT	Backward Layer Temperature
CTWD	Contact Tip to Work Distance
CMT	Cold Metal Transfer
DED	Directed Energy Deposition
EB	Electron Beam
EWW	Effective Wall Width
FLT	Forward Layer Temperature
GMA	Gas Metal Arc
GTA	Gas Tungsten Arc
LEWD	Layer Edge to Water Distance
ISAM	Industrial-Scale Additive Manufacturing
IT	Interpass Temperature
LB	Laser Beam
LH	Layer Height
LMD	Laser Metal Deposition
SLM	Selective Laser Melting
NIAC	Near-immersion Active Cooling
SW	Surface Waviness
PA	Plasma arc
PBF	Powder Bed Fusion
PTA	Plasma Transferred Arc
WAAM	Wire + Arc Additive Manufacturing
TWW	Total Wall Width

TABLE OF CONTENTS

CHAPTER I - INTRODUCTION

1.1 Contextualization

In recent years, the way to manufacture products, including manufactured goods, has changed. To stay competitive, manufacturers have sought to produce with more quality, but always seeking to concomitantly reduce production times and costs. In this line, direct routes of rapid manufacturing, involving subtractive and additive processes, are included. The subtractive ones, more traditional, for example machining, are based on the removal of material to reach the final product. The additives, newer, are based on the addition and encompass a range of manufacturing processes and materials. Analogously, subtractive processes resemble the work of a sculptor, whereas additive processes are like mounting a Lego®, as illustrated in Figure 1.1.
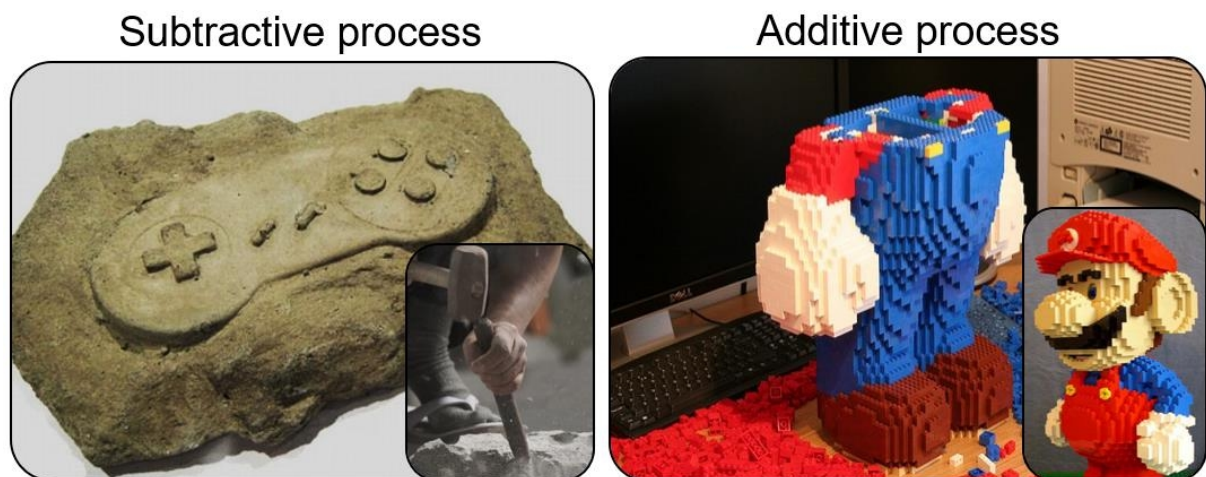
Figure 1.1. Analogy between subtractive and additive manufacturing processes (scheme assembled by the author using images from Google)

ISO/ASTM International (2015) standard guide defines Additive Manufacturing (AM) as a process of joining materials to make parts from 3D model data, usually layer upon layer, as opposed to subtractive manufacturing and formative manufacturing methodologies. Broadly, AM encompasses all AM techniques applied to all materials.

AM technology has been in use since the 1980s. In the early phase, the application of AM technology was basically limited to the production of polymeric prototypes, which were usually not functional, so it is still referred to as rapid prototyping. However, the AM concept has been expanded, allowing the production of functional components (Gibison et al., 2010). By far the greatest opportunity in AM, however, and the reason behind its current hype, is its promise to replace conventional production technologies for serial manufacturing of components or products. The latter application also bears numerous opportunities for business model innovation (Jiang et al., 2017).

The global market for AM machinery and materials have been growing significantly in recent years, as traced by Wohlers (2019) reports. However, SmarTech Publishing (2018), reporting on emerging metal printing opportunities, argues that the largest share of the AM market is focused on rapid prototyping, which is usually called as "3D printing", while the AM of functional parts is limited to very specialized applications. In fact, the lack of distinction between 3D printing and AM of functional parts, as well as the portrayal of some highly publicized applications, may imply that the Industrial-Scale Additive Manufacturing (ISAM) is now firmly established. However, this is not the case, as highlighted by Thomas-Seale et al. (2018) for the United Kingdom industry scenario. According to Additive Manufacturing UK National Strategy 2018-2025 (2018), the reasons for that are the lack the awareness, resources or confidence. Concerning the Brazilian panorama and its peculiarities, it should be no different.

Thomas-Seale et al. (2018) postulated that the most promising technologies for ISAM of metallic components are Powder Bed Fusion (PBF) and Directed Energy Deposition (DED). PBF technologies selectively fuse feedstock (powder) on the build area using thermal energy (laser or electron beam), while DED uses a focused thermal energy source (laser, electron beam or plasma arc) to fuse materials (wire or blown powder) as they are being deposited (ISO/ASTM International, 2015). Detailed reviews addressing the main features of both technologies for different materials can

be found in specialized literature, as per Frazier (2014), Herzog et al. (2016) and Debroy et al. (2018).

The PBF technologies are referred by their high resolution, which makes it suitable to produce high-complexity parts. However, PBF processes are still prohibitively expensive and production time is too long for large components. Therefore, these limitations are boosting the continuous increase in the interest for DED among academics and industrial personnel, particularly arc-based approaches, hereinafter referred to as Wire + Arc Additive Manufacturing (WAAM).

WAAM is a DED approach which adopts electric arc as thermal energy source and metallic wire as feedstock. It is based on processes typically employed for welding yet adapted for AM purposes. According to the ASTM F3187-16 standard guide (ASTM, 2016) the arc-based processes suitable for WAAM are ostensibly based on the gas shielded welding processes, namely Gas Tungsten Arc (GTA), Plasma Arc (PA), Plasma Transferred Arc (PTA) and Gas Metal Arc (GMA), and variants thereof. WAAM is relatively quiet extensively reviewed in the current literature, as per Rodrigues et al. (2019), Cunningham et al. (2018), Pan et al. (2017), Williams et al. (2016), and Ding et al. (2015). Not specifically to any of the cited arc-based processes, these reviews all culminate in the fact that the main advantages of WAAM are the high deposition rate, flexibility of implementation and cost-saving features. There are other advantages not widely mentioned, likely more tangible than the term "cost-saving", which turns to be imprecise if the whole design and production constraints are not correctly outlined. Therefore, WAAM is highlighted as a focus of this thesis.

1.2 Motivation for WAAM of aluminum

As WAAM is based on welding process and its consumables, virtually all commercial welding wires can be applied in such AM approach. However, SmarTech (2018) report entitled "Markets for Aluminum Alloys in Additive Manufacturing: 2018 to 2028" expects the market for aluminum alloys to become a major segment in AM. According to this report, the ISAM adoption is going to shift the market from high-cost/top-performance alloys such as Ti and Ni superalloys towards Al alloys, which are not so expensive but can still offer adequate performance and find large application in the aerospace and automotive markets.

Aluminum alloys widely used in the aerospace and automotive industries include the high strength 2xxx, 5xxx, 6xxx, and 7xxx series. However, these alloys are still struggling to find their way to being declared as successfully processable by PBF (Aboulkhair et al., 2019). For DED, weldability becomes a processing setback. According to the consolidated welding literature (Kou, 2002), Al alloys from 2xxx, 6xxx and 7xxx series (hardened by precipitation) usually are prone to hot cracking and therefore may be challenging for WAAM.

Plotkowski et al. (2017) explain that the majority of research in metal AM has focused on process optimization for alloys that were originally designed for traditional manufacturing routes, e.g. casting and forging. However, alloys selection in this manner will generally compromise material properties in favor of minimizing the development of defects during processing. Hence, it is expected that the most significant potential opportunity for the future of AM of metals resides in Al alloys specifically developed for AM, like the Al-Ce alloy proposed by Plotkowski et al. (2017), the Al-Mn-Sc alloy proposed by Jia et al. (2019), and proprietary ones, such as Addalloy® and Scalmalloy®

The current literature has proven the Scalmalloy® material as being potentiality able to cope with AM challenges like anisotropy and hot cracking in PBF (Spierings et al., 2017). However, there is a gap of information related to DED, which could be related to in-process overaging due to thermal history, as reported by Rometsch et al. (2014) for Laser Metal Deposition (LMD). The Scalmalloy® overaging problem resides in the fact that it cannot be reversed through a post heat treatment, because the solubilization temperature of the scandium aluminides is close to the melting temperature of the Al-Mg matrix (Røyset and Ryum, 2005). This potential setback might be even more harmful in WAAM due to its characteristic high heat input and, without proper thermal management, heat accumulation.

1.3 The troublesomeness related to heat accumulation in WAAM

Heat accumulation occurs due to a positive energy balance. In other words, there is more heat input than output (insufficient heat sink). In practice, heat accumulation is characterized by the consecutive increase of temperature of the component being manufactured over the deposition time. According to Yang et al. (2017), the heat accumulation becomes more significant with the increase in the

number of deposited layers, *i.e.*, with increased heights in the preforms. Wu et al. (2018) explain that, despite an increasing amount of heat is dissipated to the surrounding atmosphere via convection and radiation as the wall is built up, these temperature-reducing mechanisms are less effective than direct conduction to a cool substrate, resulting in less heat dissipation and more heat accumulation.

Heat accumulation is not exclusive to DED, happening also in PBF (Jamshidinia and Kovacevic, 2015). However, it is more noticeable in high-deposition-rate AM processes, like WAAM, because of the larger heat inputs. In extreme cases, heat accumulation might lead to the part collapse (molten material running down), but before that it may lead to coarse microstructure (Wang et al., 2016), excessive oxidation (Wu et al., 2017), geometrical issues (Xu et al., 2018) and residual stress and distortion (Denlinger et al., 2015a). In this sense, thermal management techniques to cope with the heat accumulation and its deleterious consequences are of great interest.

Different approaches for thermal management in WAAM have been proposed in the current literature. The control of interpass dwell times is the simplest and most referenced approach, for instance, by Yang et al. (2017) and Lei et al. (2018). However, despite fulfilling the goal of mitigating heat accumulation, it compromises production, since there is a dead time between each deposition pass. Another possibility is to build up the preform over a cooled platform, as described by Lu et al. (2017), although this approach shows efficiency only for the first layers or small preforms. Wu et al. (2018) used forced interpass cooling with compressed CO_2 while Henckell et al. (2017) used forced cooling with a punctual jet of $N_2+5\%H_2$ behind the arc. One the one hand, Wu et al.'s approach has the advantage of not disturbing the arc. On the other hand, forced cooling during the deposition, as proposed by Henckell et al. (2017), does not delay the production. Wang et al. (2004) and Xiong and Zhang (2014) reported good results by decreasing the heat input (by changing the deposition parameters) as the preforms are built up, although this approach does not eliminate the deleterious effect of thermal degradation. Li et al. (2018) developed a contact cooling system applicable to the lateral surfaces of linear preforms based on the Peltier effect, but this system is strictly restricted to this type of geometry.

All that been said, it can be concluded that the heat accumulation is a limiting characteristic of WAAM. Although there are approaches to minimize it, each one with its advantages and limitations, a more significant challenge would be to mitigate heat

accumulation without compromising production, operational performance of the component and with low environment impact. Therefore, a novel thermal management concept is needed to overcome the challenges related to heat accumulation and thus contribute to make WAAM more widely employed.

1.4 Fundamental questions

- *How to mitigate heat accumulation in WAAM as well as its potential deleterious consequences on the integrity of the preform and/or performance of the component without compromising the production and in a way applicable to most of the geometries as well as being environmentally sound?*

1.5 Hypotheses

For answering the "Fundamental Question", the following hypothesis was raised:

- *If the preform is deposited near-immersed in water, then the heat accumulation would be uniformly mitigated without compromising production and operational performance of the component, provided that the water evaporation does not destabilize the process neither increase porosity.*

If this hypothesis can be proved, a solution based on this assumption would have the advantages of being implemented with low cost for adaptation in AM equipment and of being potentially applicable to most materials and geometries. As a drawback, the AM deposition equipment would be limited to flat-position depositions, although allowing angled walls, within some limits (overhang angles). The use of water offers an environmental appeal to the hypothesis raised as it would not require any special treatment and could be reused for multiple parts/depositions.

1.6 Research questions

The technique proposed in this thesis, based on the hypothesis just raised, is denominated as "Near-Immersion Active Cooling", whose the acronym is "NIAC". In order to demonstrate the feasibility of such technique, consequently the truthfulness of the above hypothesis, the following Research Questions (RQ) are raised:

RQ1 Is the NIAC technique able to effectively mitigate heat accumulation in WAAM?

RQ2 Would the water evaporation destabilize the deposition process or generate porosity in WAAM of aluminum?

RQ3 How to select deposition parameters for WAAM of aluminum with the NIAC, taking into account surface quality?

RQ4 Is it feasible to deposit Scalmalloy® parts by WAAM?

1.7 Objectives

The fundamental and research questions can be translated into the following objectives, which constitute de subject of this thesis:

General objective:
➢ To develop, assess and apply a low-cost and high-efficiency thermal management technique to mitigate heat accumulation in WAAM.

Specific objectives:
- To prove the concept of NIAC to mitigate the heat accumulation in WAAM;
- To demonstrate the potential effect that the water level, the key factor of the NIAC concept, could have on the process performance and stability and porosity formation;
- To develop and assess a parameter selection procedure for WAAM with the NIAC technique for a desirable target geometry; and
- To assess the functionality of the NIAC technique in a relevant environment.

1.8 General methodology and outline

The research conducted during this thesis is illustrated through the flowchart presented in Figure 1.2. Accordingly, the thesis fits to the concept of Technology Readiness Levels (TRL), according to ISO 16290 standard guide definition (ISO, 2013). At Chapter 1, the fundamental question, hypothesis and research questions are addressed, which correspond to a TRL 1 and 2. Chapter 2 brings a background on the thermal management techniques for DED, from both scientific and technological points of view. Henceforward, a brief contextualization and further specific information are given at the beginning of each of the following chapters. Chapter 3 presents the proof of concept of the proposed technology (NIAC), reaching TRL 2 and 3. In Chapter 4, it is described the development and evaluation of a functional prototype for the NIAC technique, reaching TRL 3 and 4. In Chapter 5, a methodology is devised for the development of a parametric map, and a conceptual algorithm for WAAM parameter selection is proposed, also at TRL 3 and 4. Up to this point the experiments are performed using ER 5356 wire. The application of the Scalmalloy® (AlMgScZr) was demonstrated only in Chapter 6 to assess the WAAM with the NIAC technique in a relevant environment, extending the work to a TRL 4 and 5. Finally, the Chapter 7 serves for presenting the general conclusions, contributions and limitations of this thesis as well as for suggesting futures work.
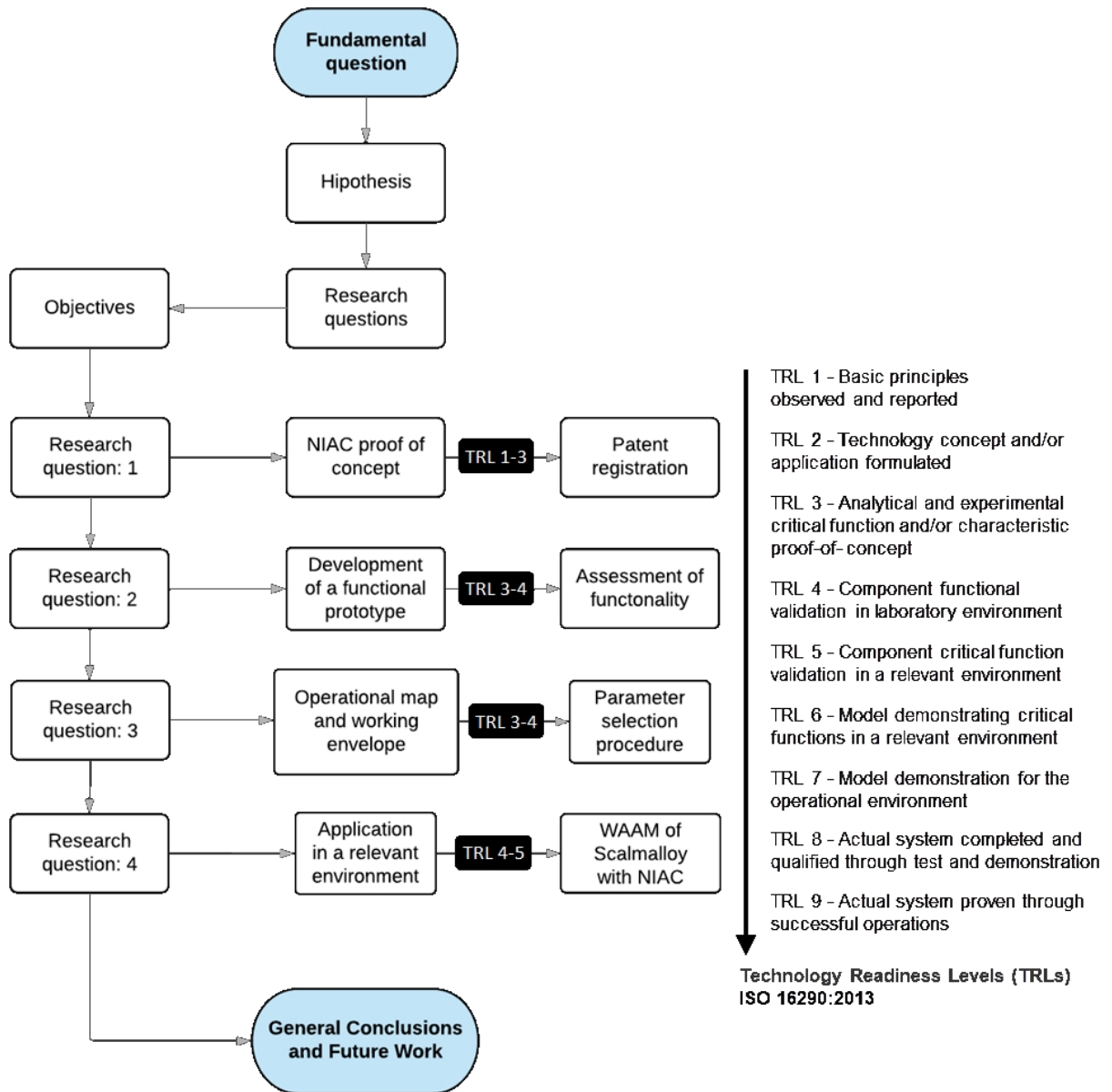
Figure 1.2. Thesis flowchart

CHAPTER II - SCIENTIFIC AND TECHNOLOGICAL BACKGROUND

2.1 Metal additive manufacturing

According to ISO/ASTM International (2015), AM encompasses all AM techniques applied to all materials. For metal AM, the main techniques are PBF and DED (Thomas-Seale et al., 2018). In Figure 2.1 these processes are classified/categorized according to the material feedstock type (powder or wire), way of distribution (powder bed or nozzle deposition) of the addition material and source of fusion used (electron beam, laser, and arc).
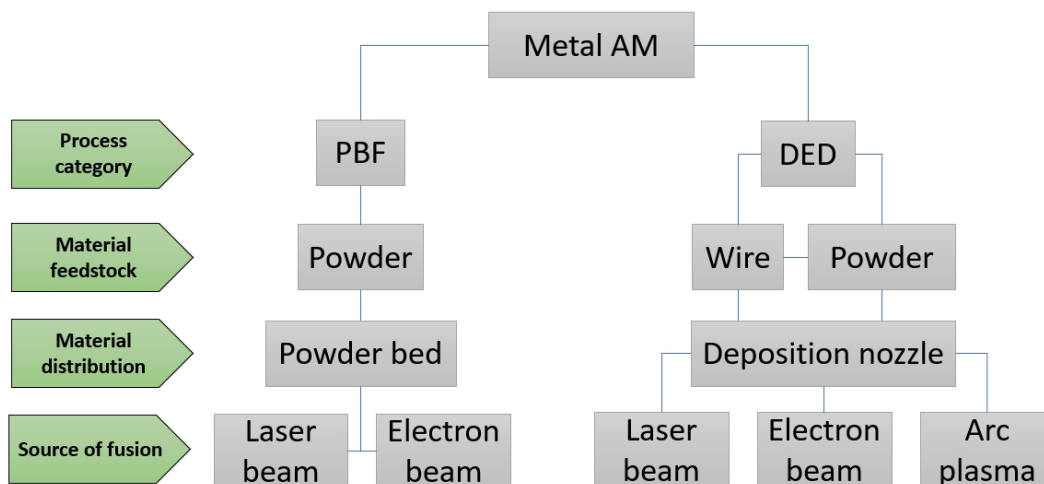
Figure 2.1. Classification of most common metal additive manufacturing processes (based on ISO/ASTM International (2015))

In addition, the metal AM processes can be broken down according to its characteristics, such as cost, part size/deposition rate and resolution/part complexity, as shown in Figure 2.2.
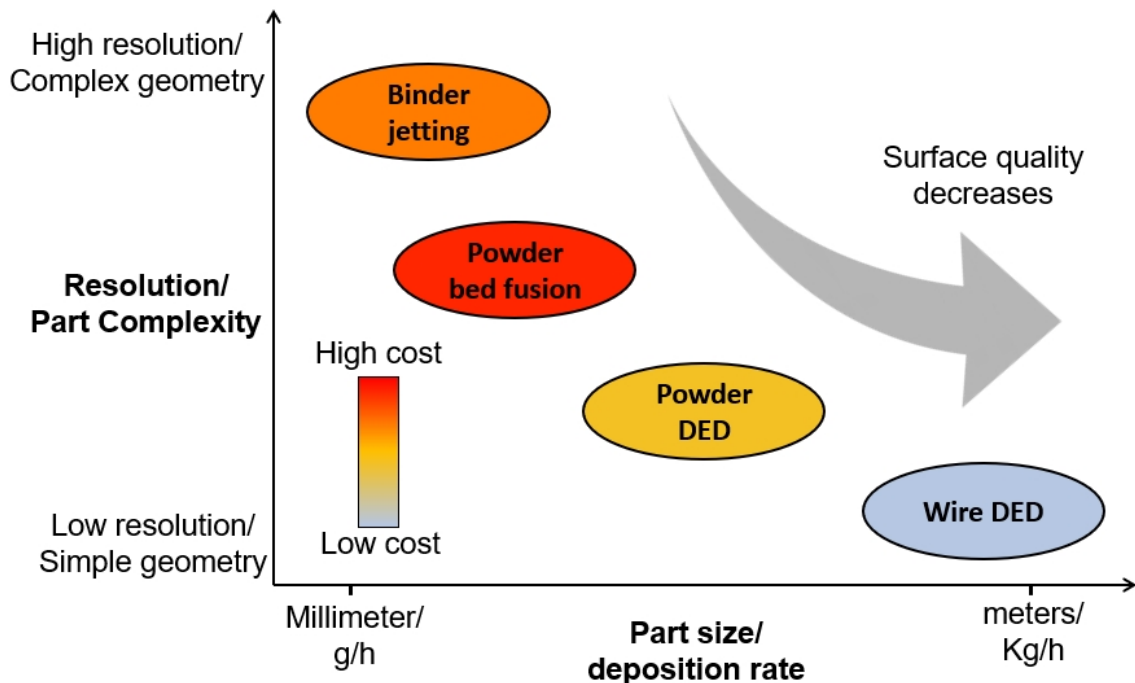
Figure 2.2. Metal AM processes classification according to main features (adapted from Digital Alloys (2019))

Powder Bed Fusion encompasses a variety of AM techniques including direct metal laser melting (DMLM), direct metal laser sintering (DMLS), electron beam melting (EBM), selective laser sintering (SLS) and selective heat sintering (SHS). Electron beams, lasers or thermal print heads are used to melt or partially melt fine layers of metallic powder which are previously spread (deposited) uniformly on a building platform, in a chamber with inert gas or vacuum (TWI, 2019). PBF is the most mature and widely used metal additive manufacturing process and is referenced by Frazier (2014) for its ability to produce high-complex geometries, as the example showed in Figure 2.3. However, PBF technologies demand high-cost energy sources, which makes dedicated equipment very expensive and out of the reach of most companies. In addition, they are generally slow construction technologies and for parts of limited size and whose consumables are expensive. According to Herzog et al. (2016), PBF technologies find application mainly in the medical and aerospace industries.

Figure 2.3. Single-piece rocket propulsion engine designed by CellCore, combining the injector and thrust chamber, which reduces numerous components into one, with multi-functional lightweight construction achievable only with PBF (SLM Solutions, 2019) (reprinted with permission from SLM Solutions)

As an alternative for larger parts with moderate complexity, there is the DED category. According to the ASTM F3187-16 standard guide (ASTM, 2016), DED is an additive manufacturing process in which focused thermal energy is used to fuse materials by melting as they are being deposited. DED systems comprise multiple categories of machines using laser beam (LB), electron beam (EB), or arc plasma energy sources. Feedstock typically comprises either powder or wire, or a combination of both. Deposition typically occurs either under inert gas (arc or laser systems) or in vacuum (EB systems).

Directed energy deposition additive manufacturing can be used with a wide variety of materials including ceramics, metals and polymers (TWI, 2019). DED systems have the following general collection of characteristics: ability to process large build volumes (>1000 mm^3), ability to process at relatively high deposition rates, use of articulated energy sources, efficient energy utilization (electron beam and arc plasma), strong energy coupling to feedstock (electron beam and arc plasma), feedstock delivered directly to the melt pool, ability to

deposit directly onto existing components, and potential to change chemical composition within a build to produce functionally graded materials (ASTM, 2016).

A DED system comprises four fundamental subcomponents: heat source, motion system, feedstock feed mechanism, and a computer control system. They also come in many shapes, sizes, and types, and commonly use laser, electron beam, or arc plasma heat sources. In all DED systems, the feedstock is fed directly to the junction of the heat source and the work piece. From there, the advantages of the different heat sources begin to assert themselves. Laser and electron beam have significant standoff capability and have very high energy densities at the work piece compared to arc plasma sources. In contrast, an arc plasma system can be less costly. Thus, each system, distinguished by its heat source and feedstock, brings certain capabilities to 3D building and repair (ASTM, 2016).

Commercial DED systems are marketed, for example, by Sciaky Inc. (EB) RPM Innovations Inc. (LB) and Gefertec GmbH (arc plasma). ASTM (2016) gives a general guide regarding the relative capabilities of the main DED processes, as shown in Figure 2.4. This guide does not include all criteria for process selection, and it is not intended to be used as a process selection method.

Process	Build Volume	Detail Resolution	Deposition Rate	Coupling Efficiency	Potential for Contamination
Laser Directed Energy Deposition					
Electron Beam Directed Energy Deposition					
Arc Plasma Directed Energy Deposition					
Lower					**Higher**

Figure 2.4. Comparison of various DED processes (ASTM, 2016)

A major advantage of DED over subtractive approaches lies in the saving of raw materials, which becomes even more significant for small batches and expensive and difficult-to-machine materials such as Ti alloys and Ni superalloys. Thus, AM represents an environmentally correct manufacturing solution, since the waste of chip-shaped material can be drastically reduced (Kellens et al., 2017). Moreover, for low/moderate complexity geometries, DED technologies are significant faster than PBF ones. Figure 2.5 shows an example of a Ti component made by Norsk Titanium Rapid Plasma Deposition® process (arc plasma DED), which according to Norsk Titanium (2019) is 50-100 times faster than PBF systems, while using 25-50% less Ti than staring with the traditional forging route.

Within the DED category, arc plasma based processes have been gaining academic and industrial prominence, mainly due to their high deposition rate, low cost and flexibility (Williams et al., 2016). As the present thesis focus on a specific arc plasma DED process, the next section is used to briefly review the key aspects of Wire + Arc Additive Manufacturing (WAAM), highlighting its Cold Metal Transfer (CMT) GMA variant.

Figure 2.5. A titanium component manufactured by a patented DED process from Norsk Titanium called RPD® (reprinted with permission from Norsk Titaniun)

2.1.1 Wire + Arc Additive manufacturing - WAAM

WAAM is a DED approach which adopts electric arc as thermal energy source and metallic wire as feedstock. It is based on processes typically employed for welding yet adapted for AM purposes. Processes for WAAM and its features are relatively consistently reviewed in the current literature, as per Rodrigues et al. (2019), Cunningham et al. (2018), Pan et al. (2017), Williams et al. (2016), and Ding et al. (2015). Regardless of the arc-based processes assessed, all these reviews culminate in the fact that the main advantages of WAAM are the high-deposition-rate, flexibility of implementation and cost-saving features. According to the ASTM F3187-16 standard guide (ASTM, 2016), the arc-based processes suitable for WAAM are ostensibly based on the gas shielded welding processes, namely Gas Tungsten Arc (GTA), Plasma Arc (PA), Plasma Transferred Arc (PTA) and Gas Metal Arc (GMA), and variants thereof. It is worth mentioning that, according to this same standard, the word "welding" in the American Welding Society - AWS definition conveys the joining of two or more pieces of material. As this is not the case for DED, the word "welding" is dropped from the name of each process, and so it is the letter "W" from each corresponding acronym. The remaining terms are enough to characterize the arc physics in each case.

According to Williams et al. (2016), whenever possible, GMA is the process of choice for arc plasma DED: the wire is the consumable electrode, and its coaxiality with the process torch results in easy tool path. As GMA, GTA or PA processes are other options that allow easy control of the heat input (Pan et al., 2017). However, Williams et al. (2016) mention that they are limited by the fact that the wire must be fed always from the same direction, which requires rotation of the torch/part during changes in the deposition path, thus complicating robot programming. The current literature has shown that among the versions of the GMA process, the Fronius Cold Metal Transfer (CMT) seems to provide better results with WAAM. Therefore, a brief overview of CMT process is presented in the following section.

2.1.1.1 Cold Metal Transfer - CMT

CMT stands for "Cold Metal Transfer" and describes a controlled short circuit (dip transfer) GMAW process. According to Norrish and Cuiuri (2014), there are around 10 variants of the controlled dip process. Despite that, they explain that the basic principles remain the same; the current is reduced immediately before the short circuit rupture reducing the pinch effect, avoiding explosive detachment and allowing the droplet to be drawn into the pool by surface tension. In contrast with the current-controlled short circuit transfer (e.*g*. Surface Tension Transfer® from Lincoln Electric), in the CMT process the droplet detachment and arc reignition are achieved in a controlled fashion by a backward movement of the filler wire.

Figure 2.6 shows the CMT process states and the corresponding progression of wire feed speed, welding current and voltage signals. The wire is fed to the workpiece until a short-circuit occurs and the arc is extinguished. The direction of the wire movement is then reversed, *i.e.*, the wire is withdrawn from the workpiece. This breaks the short-circuit and the arc is reignited. The wire movement is then reversed again, and the described process starts again from the beginning. Depending on the characteristic curve for the filler metal, shielding gas and electrode diameter this reversing movement takes place in a frequency ranging from 50 to 130 Hz (Fronius, 2014). Is worth mentioning that there are variants of the CMT process, such as the CMT Pulse (pulsed arc) and the CMT Advanced (variable polarity) and combinations thereof.
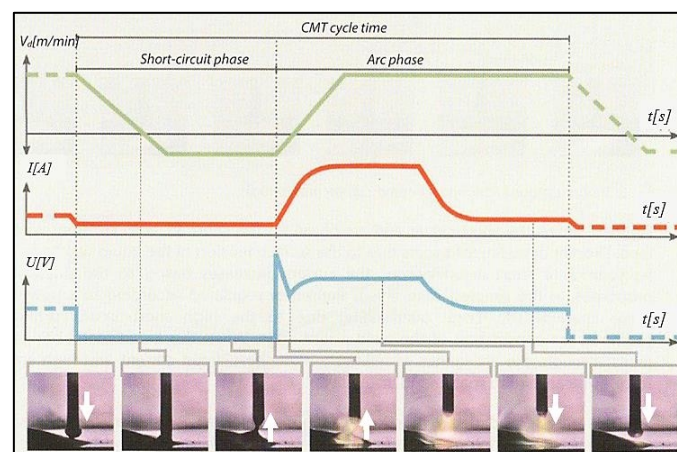

Figure 2.6. CMT process flow with wire feed, current and voltage typical signals (Fronius, 2014)

The CMT delivers beads with excellent quality nearly without spatter and with lower heat input, which qualify it as appropriated for AM (Williams et al., 2016). However, the reasons for the adequacy of CMT for AM extent those just mentioned. Because of the arc length can be maintained very short, the arc pressure on the molten pool is small. In addition, heat is transferred to the material in a very regular basis. These two characteristics imply that the weld pool is very controllable, as demanded to build up layers upon layers, especially on relatively thin walls.

Nonetheless, CMT has a few drawbacks. The first is the need for a characteristic line for each wire (material and diameter) and shielding gas combination. This makes it difficult to use other materials than those provided in the installed synergic line packages. The second is related to the wire feed speed control performed by the power supply to keep the arc length constant and independent of the contact tip to work distance changes. This process control creates a difference between the adjusted and real (measured) wire feed speed. Ali et al. (2019), who performed WAAM of a tool steel with CMT, reported differences between 20 - 32%.

Finally, regardless of the arc process, WAMM is always associated with undesirable high heat input, which, without proper thermal management, might be even more problematic due to heat accumulation. The negative issues related to heat accumulation in preforms made by DED process are compiled and briefly discussed over the following section.

2.1.2 Negative aspects related to heat accumulation

As it happens for other manufacturing process, the final microstructures and mechanical integrity define the resulting performance of the component in AM. But due to the complex history experienced during deposition time, the microstructure from a metallic component produced by AM differs significantly from those produced by conventional process, e.g., forging and casting. This potential setback might be even more harmful in WAAM due to its characteristic high heat input and, without proper thermal management, to heat accumulation.

Heat accumulation occurs due to a positive energy balance. In other words, there are more heat input than output (insufficient heat sink). In practice,

heat accumulation is characterized by the consecutive increase of temperature of the component being manufactured over the deposition time. This phenomenon is not exclusive to DED, happening also on PBF (Jamshidinia and Kovacevic, 2015). However, it is more noticeable in AM processes with high deposition rates, such as WAAM, because of their high heat inputs.

The effect of heat accumulation on the metallurgical aspects of austenitic stainless steel walls made by LMD was investigated by Manvatkar et al. (2014). These authors verified a molten pool enlargement, higher temperature experienced by the previous layer, lower cooling rate, lower G/R solidification parameter and lower hardness as the walls were built up. Subsequent results reported by Wang et al. (2016), with GTA and Inconel® 625 wire, and by Foster et al. (2017), with LMD and Inconel 625® and Ti6Al4V powder, have corroborated and extended these behaviors to other materials and energy sources, including wire and arc.

Besides metallurgical changes, the heat accumulation also impacts on operational aspects of WAAM as well as in geometric and superficial features of the parts produced. Xiong et al. (2017) reported molten pool collapse and geometric deviation of the preforms due to heat accumulation in WAAM of low carbon steel using the GMA process. Wu et al. (2017), in addition to a widening effect on the walls, described excessive oxidation due to the heat accumulation in WAAM of Ti6Al4V using the GTA process. Xu et al. (2018), in a more detailed analysis on this feature, found that excessive oxidation impairs the wettability and, consequently, the geometric regularity of layers produced with maraging steels in WAAM using the GMA process.

Thus, in additive manufacturing of metallic preforms, the lack of proper thermal management makes it difficult to obtain the desired geometry and mechanical properties. Therefore, to turn DED processes with their high deposition rates into a concrete industrial reality it is of paramount importance to promote the thermal management of the preform by means of administrating the application, distribution and removal of heat, before, during and after the manufacturing operation.

2.2 Thermal management techniques for Directed Energy Deposition - DED

In this section is proposed a classification for the thermal generation techniques for DED, as well as is presented a scientific and technological review of these techniques.

2.2.1 Thermal management techniques classification

In order to compile and discuss, in an organized and effective way, the thermal management approaches found in the different sources of literature (mainly scientific papers and patents), an original classification was devised. Based on the studies and developments surveyed, in addition to the Natural (conventional) approach, in general, it is possible to classify the thermal management approaches for additive manufacturing as Intrinsic, Passive or Active.

➢ *Natural approach*

In the Natural approach, considered as the conventional method to deal with the thermal management (limited to cooling), the preforms production and their features might be based on the time the deposited layers are allowed to cool down to a target temperature level (interpass temperature) before the deposition of the next layer is resumed. Besides the dwell times (interpass time) required, the interpass temperature is a consequence of the heat already accumulated within and the heat dissipation capacity of the preform, which turn out to be dependent on its material and geometry.

➢ *Intrinsic approaches*

In the Intrinsic approaches, the thermal management is accomplished by means of the inherent ways the deposition process offers for changing factors such as heat input and material deposition rate, *i.e.*, basically by modifying parameters settings or even by switching, modifying or combining DED processes.

➢ *Passive approaches*

In the Passive approaches for thermal management, the cooling and/or heating agent acts only over the building platform and/or substrate before, during and/or after the construction period, *i.e.*, the temperature administration of the preform is accomplished in an indirect manner through an intermediate element (construction platform and/or substrate), which limits the scope and reach of the effects produced.

➢ *Active approaches*

The Active thermal management approaches, in contrast with the passive ones, all consist of acting in an accentuated manner on the characteristics of the preform or part by means of direct contact, in a total or partial way, with the cooling and/or heating agent, usually a fluid, during and/or after the construction period.

Thus, as outlined in Figure 2.7, each thermal management approach can be classified according to:

- **Type:** the way that the heating and/or cooling is effective to the preform (Natural, Intrinsic, Passive or Active);
- **Subtype:** the way that the heat is applied to and/or extracted from the preform in terms of contact (Indirect or Direct);
- **Action:** the duration that the heating and/or cooling acts on the preform;
- **Means:** the process mode or the state of the heating and/or cooling source matter (Solid, Gas or Liquid);
- **Application:** the way that the heating and/or cooling source matter is applied to the preform (Natural, Process Inherent, or Forced);
- **Effect**: The thermal effect that the heating and/or cooling has on the preform (Heating or Cooling).

Type:	Natural	Intrinsic	Passive	Active
Thermal management approaches for DED				
Subtype:	Direct	Direct	Indirect	Indirect or Direct
Action:	Continuous	Continuous	Continuous	Continuous or Intermittent
Means:	Air	Current and Wire Feed Control	Gas or Liquid	Solid, Gas or Liquid
Application:	Natural	Process Inherent	Forced	Forced
Effect:	Cooling	Cooling and/or Heating	Cooling and/or Heating	Cooling and/or Heating

Figure 2.7. Classification of the thermal management approaches (by the author)

2.2.2 Scientific review based on articles

Data collected from a systematic review of scientific articles are compiled in Table 2.1. According to this survey, one can say that Natural cooling is the most referenced approach, for instance, as by Yang et al. (2017) and Lei et al. (2018). This is probably because it is the simplest approach for thermal management. But despite fulfilling the goal of mitigating the heat accumulation, it compromises productivity, since there is a dead time between each layer, which significantly extend production time. Moreover, preforms made under the Natural thermal management approach are still subjected to thermal degradation of mechanical properties, such as grain growth. Another possibility is to build up the preform over a cooled platform (Passive thermal management), as described Lu et al. (2017), although this approach shows efficiency only at the first layers and/or for small preforms. Wu et al. (2018) used forced interpass cooling with compressed CO_2 (Active-Intermittent thermal management) while Henckell et al. (2017) used forced cooling with a punctual jet of $N_2+5\%H_2$ behind the arc (Active-Continuous thermal management). On the one hand, Wu et al.'s approach has the advantage of not disturbing the arc. On the other hand, forced cooling during the deposition, as proposed by Henckell et al. (2017), does not delay the production. Wang et al. (2004) and Xiong and Zhang (2014) reported good results by decreasing the heat input as preforms are built up by the changing of deposition parameters (Intrinsic thermal management), although this approach does not eliminate deleterious effects of thermal degradation. Li et al. (2018) developed an active, but indirect, cooling system based on the Peltier effect applied to the lateral surfaces of linear preforms, but the system seems strictly restricted to this type of geometry.

Table 2.1. Summary of the state of the art on thermal management in terms of type, approach and respective main contributions

Reference	Thermal management approach	Main highlight	Deposition process and material	Relevant contribution for the present thesis
Yang et al. (2017)	Natural	Use interpass cooling time	GMA and low carbon steel	Interpass temperatures below 200 °C resulted in better wall quality. Very long dwell times, over 5 minutes, did not result in significant improvements.
Lei et al. (2018)			GMA and low carbon steel	No heat accumulation occurred for interpass times above 5 minutes.
Denlinger et al. (2015)			LMD, Inconel 625 and Ti6Al4V	The results obtained showed that adding time to allow additional cooling during the deposition process results in reduced distortion and residual stress in Inconel®625. The opposite was true for Ti-6Al-4V, where decreased dwell time results in significantly lower distortion and residual voltage levels.
Shen et al. (2017)			GTA and Al+Fe alloy (double wire)	Deposition current determines grain size and interpass temperature to prevent cracking induced by residual stresses. The authors suggest that the parameters should be selected to obtain a properly sized molten pool.
Ma et al. (2015)			GTA and Al+Ti alloy (double wire)	The interpass temperature had no significant influence on the microstructure but is important for mitigating cracks induced by residual stresses.
Wang et al. (2016)			GTA and Inconel 625	Coarser microstructure and lower hardness towards the top layer. Significant increase in pool size and reduction in cooling rate as the number of layers are added, *i.e.,* the distance from the substrate, increases.
Foster et al. (2017)			LMD, Inconel 625 and Ti6Al4V	The longer the interpass time (cooler preform) the finer the microstructure, the higher the hardness and the mechanical strength achieved.
Xiong et al. (2015)			GMA and low carbon steel	The current is the main factor on the formation of the layer, because, in addition to heat, it imposes pressure over the liquid pool.
Wu et al. (2018)	Active-Direct	Used forced interpass cooling with a CO_2 jet on the top layer	GTA and Ti6Al4V	Measuring the temperature of the layer provides more accurate and realistic data. The heat accumulates approximately linearly with the number of layers. The first layers are less oxidized and narrower than the last ones due to heat accumulation.
Henckell et al. (2017)	Active-Direct	Used N_2 + 5% H_2 jet behind the torch (165 mm)	GMA and low carbon steel	Thermal management reduced heat accumulation as well as all deleterious effects caused by it (molten pool collapse, increased layer width, grain growth, varying hardness). Heat accumulation can be reduced and eventually controlled by the type of gas employed.

*to be continued

Table 2.1. Summary of the state of the art on thermal management in terms of type, approach and respective main contributions

Reference	Thermal management approach	Main highlight	Deposition process and material	Relevant contribution for the present thesis
Fayolle (2016)	Active-Direct	Used liquid argon jet (cryogenic)	GTA and Ti6Al4V	Thermal management reduced oxidation and significantly increased productivity
Li (2018)	Active-Direct	Used thermoelectric effect (Peltier)	CMT-tandem and Al-Si-Mg alloy	It accomplished improved geometric quality and increased productivity and promoted grain refining.
Yanagida and Koide (2008)	Active-Direct	Used water-shower cooling behind the arc	GMAW* and AISI 304	The application of this technique improved geometric quality, increased productivity and promoted grain refinement.
Geng et al. (2017)	Intrinsic	Decreased the arc energy, supposedly by increasing the travel speed	GTA and Al-Mg alloy	A theoretical model was developed to determine a suitable interpass temperature for each deposition.
Farshidianfar et al. (2016)			LMD and AISI 304L	A system controls the cooling rate / microstructure in real time by varying the deposition speed. One of the most important capabilities of a real-time microstructure controller is the ability to produce desired local mechanical properties.
Wang et al. (2004)		Reduced the deposition current	GTA and Al 4043	The modulation of the heat input is accomplished by reducing the welding current from 140 to 100 A in the first 40 layers, being minus 1 A per layer addition and keeping it constant at 100 A for the rest of the layers. In this case there is no production losses because the heat source is independent of the deposition rate.
Xiong et al. (2013)		Increased the travel speed	GMA and low carbon steel	The layer width was kept constant along the cross section by increasing the welding speed as the layers were deposited.
Cao et al. (2017)	Passive	Cooled the platform/substrate	GMAW* and Al alloy	Weldments were performed under a water-cooled platform. Under this condition, the width of the softened zone was reduced, and the microhardness, the tensile strength and nominal yield strength of the welded joints were all improved
Lu et al. (2017)			GMA and low carbon steel	The thin wall parts are more difficult to be deposited continuously without a compulsory cooling solution, i.e. Natural condition.
Ali et al. (2019)			GMA and tool steel	To obtain a better heat dissipation and reduce the waiting (dwell) time between the layers, a cooling plate was placed under the base plate to maintain a constant temperature of 17 °C.

* Results related to welding experiments

2.2.3 Technological review based on patents

Due to the innovative potential of the thermal management technique developed in this thesis, in addition to scientific, a technological review was raised in terms of patents aiming at filing a possible patent application. This patent search was performed on Google by using combinations of the following keywords:

- Additive manufacturing
- Welding
- 3D Printing
- Heat control

- Cooling control
- Temperature control
- Heat sink
- Shape control

The invention of Adams (2005) (US7326377B2), in a Passive-Indirect heat management approach for moderating heat in the preform and its consequences, deals with a system for additive manufacturing with electric arc using a heat extraction or imposition block with circulation fluid around fins, coupled to the construction platform. In the case of heat extraction, the cooling fluid used is preferably a substantially cooler liquid than the block itself, which may be basically water but possibly glycol, mixtures of glycol and water and even gases which assume liquid state at temperatures well below that of the environment, such as liquid nitrogen or helium. In the case of heat imposition, heating devices may be incorporated in the block or used to heat the circulating fluid. A fluid circulation control system provides a mechanism for inducing high rates of cooling or heating as molten raw material is deposited on the substrate. As advantages offered are the control of oxidation and grain size of the preform, which allows to optimize the mechanical strength and ductility of the part. However, since the thermal management used is Passive-indirect, there is a limitation of the extent of the effects, which are restricted to reduced-height preforms or to layers of levels closer to the temperature control block, therefore to the substrate.

In that same Passive_indirect line of action, the invention of Peretti and Trapp (2010) (US2010242843A1) relates to a mandrel (support for preforms of revolution) used as a construction platform for additive manufacturing with electric arc, laser or electron beam. To cool the preform under construction, this mandrel has higher thermal conductivity than that of the deposition material and has internal channels for passing

cooling fluid. Advantages achieved include the increase in the speed of manufacturing of the preform and the attainment of improved mechanical properties, even if restricted to preforms of limited height or to layers closer to the mandrel.

Further, the invention of Guo (2017) (CN107498043A) relates to the cooling of the building platform in additive manufacturing, but with melting-deposition of metallic wire by electron beam. The control of the indirect and continuous cooling of the preform, by means of internal circulation of fluid in the construction platform, occurs in closed circuit based on the monitoring of its temperature. Thus, negative effects due to the low pressure over the molten pool and solidification of the material (molten pool spreading, low heat dissipation, etc.) inherent to compulsory high vacuum in the electron beam building chamber are minimized.

Similarly, the invention of Karlen (2016) (US20170355019A1) relates to the use of a heating element of at least part of the preform during additive manufacturing with melting-deposition of material. The heating element, electric coil or other suitable device, is controlled as a function of thermal imaging of the preform to prevent non-uniform heating, thereby reducing defects correlated to heating and/or non-uniform cooling during construction. With this approach, the reduction of thermal gradients in the preform is obtained, improving the control of distortions and minimizing the risk of solidification cracking.

In a similar line, the invention of Dutta (2016) (US2016271732A1) describes a substrate and/or layers preheating device for use in additive manufacturing of metal preforms with melting-deposition of powdered material. The preheater, capable of generating heat by the passage of electric current and induction, is mounted to accompany the energy source in the deposition path always close by and heating the substrate and/or the anterior layer immediately ahead of the current deposition region. In this case, it is possible to form the molten pool more easily and thus to traverse the deposition path more quickly and at the same time to obtain a more adequate configuration of the first layer (better spreading) for the deposition of the subsequent one and so on, since the preheating increases the wettability of the molten material on the substrate, previously at the ambient temperature, and/or on the other layers.

There are other developments that use both heating and cooling to address the thermal management of preforms and parts. In that sense, the invention of Naware (2014) (US2016096326A1) encompass a plate-shaped construction base with multiple

cooling and/or heating elements, which may be of diverse types. This plate is used to selectively cool and/or heat the part being built just above, to constantly control the thermal gradient and temperature distribution generated and thus allow mechanical stresses of thermal origin to be reduced. Again, this is a Passive-indirect thermal management approach, since the cooling medium only contacts the base of the part, which restricts the effects to limited heights of it.

While addressing Passive-indirect thermal management, the invention of Albrecht and Hsu (2014) (US20150021815A1) relates to temperature control devices which can be used during at least a portion of the additive manufacturing process. In this case, a device coupled to the construction platform can indirectly control the cooling rate of the preform to result in the desired microstructure. This device may include a cooling element, such as air, water or oil coils, and/or fans. With this approach it is possible to increase the deposition rate of material. In addition, other temperature control devices may act on the substrate prior to (preheating) the preform construction, to prevent distortion, and/or after (post heating), to provide it with annealing.

The invention of Fischer et al. (2015) (EP3069804A2) relates to a method with Active-Direct and continuous cooling of preforms, preferably metallic, for additive manufacturing by selective powder bed fusion with laser or for melt-deposition processes of material. In this case, the preform is constructed with integrated cooling or heating channels, which may also be on the construction platform, in this case with individually sealable outlets, through which a fluid passes by. The temperature and/or the flow of the fluid, controlled based on the temperature measurement (thermography) of the preform and by means of an external cooling and/or heating system, are used to perform the thermal management. The fluid employed is a non-corrosive and non-flammable liquid preferably with high thermal conductivity that can be used multiple times by using filtration. This fluid may partially or entirely fill the channels integrated in the walls of the preform, may overflow between deposition passes to provide corrosion protection, oxidation and adhesion of melt deposition spatter, and even for cooling-lubrication in case of interpass machining. It can also flow with different temperatures through different channels, with temperature changes of the preform in time and space, generating a varying thermal gradient. Thus, the method allows to instantaneously manage the heat coming from the source of melting and emanating from the preform, thus controlling the formed microstructure (and resulting mechanical

properties) and the residual stresses. In addition, it allows to avoid accumulation of heat and, thus, makes it possible to use higher material deposition rates without deteriorating the resulting mechanical properties. However, in order to operate, the method requires that a substrate with holes aligned with those of the construction platform, for passage of the fluid. It also demands that the part must be at least partially modified in its three-dimensional CAD design prior to construction to include internal channels integrated into the walls of the preform, which requires more machining of the part to remove the volume of material with channels to reach the final geometry of the piece.

There are also developments that employ Active-Direct and continuous cooling for thermal management by the application of localized gas over the preform. In this line, the invention of Xiong et al. (2015) (CN104959606A) deals with a localized temperature control system for additive manufacturing of metal parts by melting-depositing material in the form of wire or powder. In this case, the temperature control is carried out during construction by means of a preferably inert gas flow directed by a cooling nozzle towards the already solidified region of the preform near the material deposition head. After draining heat from the preform, the gas flow is sucked into the back of the nozzle and directed to a cooling unit to then re-act in a localized manner. The gas flow rate and temperature are controlled to define the formed microstructure, including dynamically according to the position in the preform.

2.3 Summary

Based on the scientific and technological review presented, the following points can be drawn:

- Heat accumulation is a limiting characteristic of WAAM, which could impair on metallurgical and geometrical features;
- Although there are approaches to minimize heat accumulation, each one with its advantages and limitations, a more significant challenge would be to mitigate heat accumulation, without compromising production, operational performance of the component and with low environment impact;

- On the one hand, in the outlined survey, most of the scientific papers are focused on the Natural thermal management approach. On the other hand, most patents seem to be focused on the Passive and Active approaches; and
- In the patent search, no thermal management technique like the one proposed and developed in this thesis was found.

CHAPTER III - THE NIAC PROOF OF CONCEPT

3.1 The NIAC concept

The concept of NIAC has its foundations based on an active cooling of the preform by means of its relative continuous and controlled near-immersion in a cooling liquid within a work tank throughout the building time. Figure 3.1 schematically illustrates the application of the concept, in contrast to more common thermal management approaches, such as without any forced cooling means (Natural approach) or conducted by means of substrate and/or building platform cooling (Passive approach). Thus, the cooling rate of the non-immersed part of the preform and the interpass temperature would be controlled by the level of the cooling liquid and by the heat exchange with its part just immersed (dependent on initial temperature and thermal capacity and conductivity of the cooling liquid for a given material under deposition), in direct contact and already at temperature equilibrium with the liquid.

By the NIAC approach, direct contact of the cooling liquid with all the layers of the preform inside the work tank is assured, except for a few ones just below the ongoing level of material deposition. The cooling liquid could, thus, act constantly to withdraw heat directly from the preform, significantly lowering the interpass temperature, *i.e.*, the minimum temperature of the previous layer before the new deposition of material, thus potentially reducing in an expressive manner the heat accumulation in the preform as its building goes on.

It can then be considered, in contrast to the Natural and Passive approaches, that with the NIAC concept implementation the heat flow just below the deposition region would always assume a three-dimensional and balanced regime. This would induce near-isotropic cooling (more equalized in all directions), which could promote better balance of properties in the directions of the preform growth (typically vertical and horizontal), regardless of its final height.
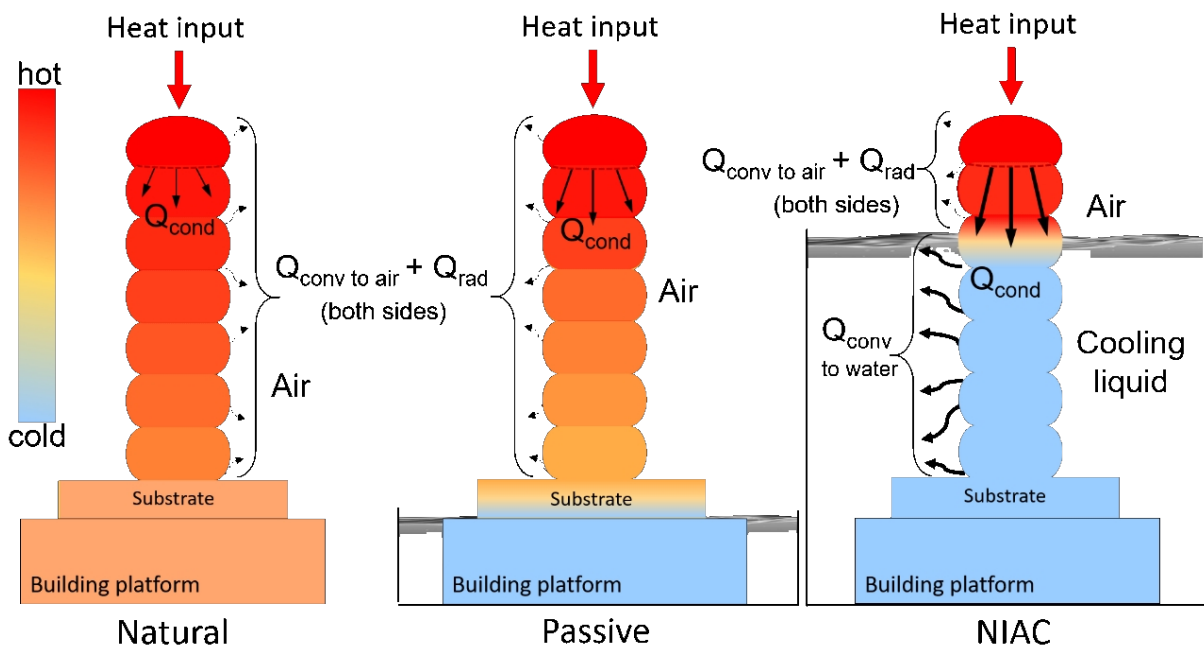
Figure 3.1. Schematic illustration of the NIAC concept versus the Natural and Passive thermal management approaches (the arrows are proportional to the heat sink intensity), where: Q_{cond} = conduction heat sink; Q_{conv} = convection heat sink; Q_{rad} = radiation heat sink (by the author)

Thus, the NIAC technique is expected to allow the mitigation of several problems linked to the heat accumulation in WAAM. Regardless of the geometry to be built, one could favorably regulate the preform features in terms of mechanical quality (microstructure and grain size/type formed, resulting properties, residual stress levels, etc.) and geometric quality (form regularity of the layers, degree of distortion, etc.). In addition, potentials for reducing the oxidation levels of the layers and even the toxic emissions (metallic fumes), typical of fusion-deposition with electric arc, are foreseen.

In addition of being able to favorably regulate characteristics more related to the preforms, the NIAC implementation would allow to preserve or even increase the productivity by increasing the building rate. This could even occur without any or with shorter and/or less frequent use of dwell times, due to the NIAC intense and continuous cooling, and/or by performing the building up operation at higher melting-deposition rates, since the corresponding increase in energy (heat) input would be counterbalanced by a larger heat dissipation capacity provided by its efficient cooling strategy.

Thus, by promoting a better thermal management of the preforms through the NIAC technique, it would be possible to couple a higher manufacturing productivity with an improved mechanical and geometric quality state. In achieving success, the NIAC concept could be extended to other DED AM processes, such as to LMD. Finally, as devised, the NIAC concept relies preferably on the use of water as the cooling liquid, which adds to the green-manufacturing appeal of AM.

In view of the diversity of the foreseen potentials, some aspects of the NIAC concept are evaluated as following to validate it as a proof of concept as introduced for thermal management in WAAM.

3.2 Experimental validation of the NIAC

The experimental validation of the new concept for thermal management was based on the comparison of three cooling approaches to the preforms; Natural, Passive and NIAC. Figure 3.2 shows the experimental rig employed for the NIAC concept. The same arrangement was used for the Passive and Natural approaches by fixing the cooling liquid level at the substrate-building platform and by draining it from the work tank, respectively, as illustrated in Figure 3.3.
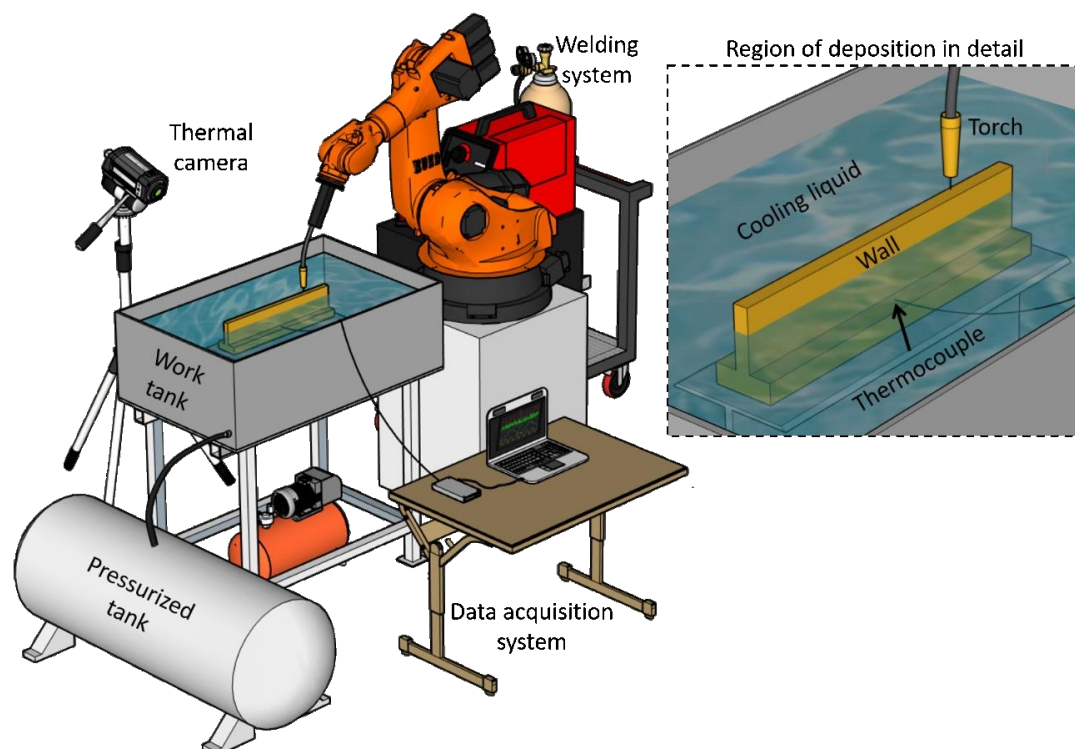
Figure 3.2. Experimental rig representation for the NIAC concept (by the author)

Single-pass multi-layer linear preforms (single walls) were deposited under the three different cooling approaches. Considering that one potential hindrance of the NIAC concept would be hydrogen contamination of the deposition pool from vaporized water, an aluminum alloy was chosen as the preform material. As well known, aluminum alloys are characterized by a high level of hydrogen solubility in the liquid state, main cause of porosity during its processing. The deposition settings are summarized in Table 3.1 and were kept constant throughout the experiments. Three walls were produced for each cooling approach. For the NIAC one, the distance separating the deposition level (arc root) from the cooling liquid was kept constant throughout the deposition height by means of a pressurized water tank. It is also important to mention that the NIAC concept was applied just after the 9th layer (approximately from 15 mm of wall height) to prevent water turbulence and evaporation and any consequent process instability and/or preform contamination.
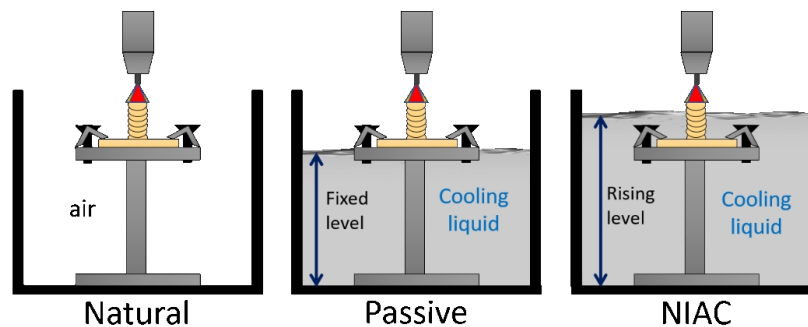

Figure 3.3. Schematic representation of the cooling approaches compared for the experimental validation of the NIAC concept (by the author)

Table 3.1. Deposition settings for the experimental validation of the NIAC concept

Arc deposition equipment	Fronius CMT - TransPuls Synergic 500
Wire (deposition material)	AWS ER 5356 - Ø 1.0 mm
Substrate	Al5052 (300 x 40 x 3 mm)
Wire feed speed	8.2 m/min
Deposition speed	7.5 mm/s
CTWD*	12 mm
LEWD**	15-20 mm (roughly kept by hand)
Shielding gas	Commercial argon - 15 L/min
Cooling liquid	Tap water at around 25 ºC
Preform geometry	Single wall with 28 layers and length of 380 mm
Building strategy	Single-pass multi-layers bidirectional depositions
Dwell time	0 s (continuous deposition)

The measured resultant average deposition current and arc voltage levels were 90 A and 8.5 V, respectively. *CTWD = contact tip to work distance; **LEWD = layer edge to water distance.

The first comparison regarding the different cooling approaches was made through thermal analyses based on thermocouple and thermography data to verify the cooling effectiveness in each case. The possibility of any contamination of the deposition pool with hydrogen was assessed by a porosity measure. Performance features of the preforms produced with each cooling approach were evaluated via mechanical (aiming anisotropy characteristics) as well as geometric quality (aiming form deviations) assessments.

During depositions, a commercial infrared camera was used to register lateral infrared portraits (thermograms) from the whole walls. From the thermograms generated, the thermal cycles of the 23rd layers at a fixed position (mid length) were monitored during the next 5 subsequent layers. In addition, at the same time, a thermal history of the substrate was measured by a 0.6-mm-diameter (each wire) K-type thermocouple fixed at the substrate mid length and positioned at approximately 5 mm from the deposition path centerline. Data from the thermocouple was used to adjust the infrared emissivity.

Considering the proof-of-concept purpose, the Archimedes method was chosen to assess porosity level in the walls. According to Spierings and Schneider (2011), the Archimedes method delivers more reliable results as the whole sample volume is taken into account instead of just single cross sections, which might not represent a typical porosity of the sample. However, the details of the shape, size and distribution of pores cannot be determined using this method. Neither other internal voids, such as solidification shrinkages, lack of fusion and cracks, can be distinguished from pores. Then, the results are presented in terms of relative density. The wire density was taken as a reference and assumed to be free of voids. Two samples weighing around 100 g each were cut from one of the preforms produced for each cooling approach. A digital balance with resolution of 0.01 g and distilled water were utilized. Three measurements were performed over each sample. First, all samples were weighted in the air to prevent the water from infiltrating in any superficial defect. Care was taken to ensure that air bubbles were not present on the samples under test.

The remaining walls were mechanically sectioned in their central regions and standardly prepared by grinding and polishing. The geometric quality (form regularity) of the preforms was evaluated by cross-sectional-view macroscopic examination, while the pore morphology was analyzed by longitudinal-sectional-view microscopy.

The effect of the NIAC technique on the anisotropy of mechanical properties was evaluated by means of tensile testing in the longitudinal (x) and vertical (z) deposition directions. In this case, specimens were machined also from the central region of the preforms, as located in Figure 3.4. Room temperature tests were conducted by using a universal testing system at a strain rate of 1 mm.min^{-1}. For statistical treatment of the results, six tensile tests were carried out for each direction of loading (directions of preform growth). For comparison purposes, the tensile tests were also likewise performed in samples produced with the Natural and Passive conditions.
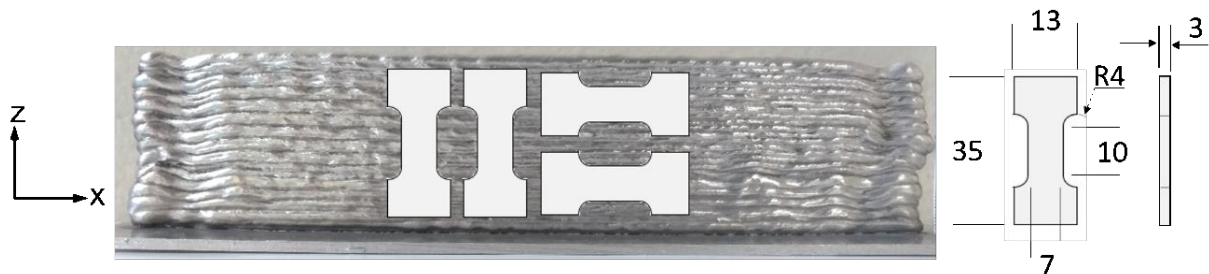

Figure 3.4. Location of the tensile specimens sampling (two from each cooling approach from three walls) and their dimensions in mm (by the author)

3.3 Results and discussion

3.3.1 Thermal analyses

Thermograms of the lateral surface of the walls deposited under the three different thermal management approaches, taken immediately after the arc was switched off, are shown in Figure 3.5. In qualitative terms, the thermal field of the preform deposited with the NIAC technique is remarkably different and evidences how it was actively cooled. For the Natural and Passive cooling approaches, the respective entire preforms exhibit high temperatures after deposition, as the heat from the deposition source (electrical arc) had accumulated, which it is in accordance with Yang et al. (2017). With the NIAC technique, in contrast, only a small area of the preform, that was surrounding the arc last position, appears expressively heated since the water level following immediately below quickly cooled down the rest of the preform.
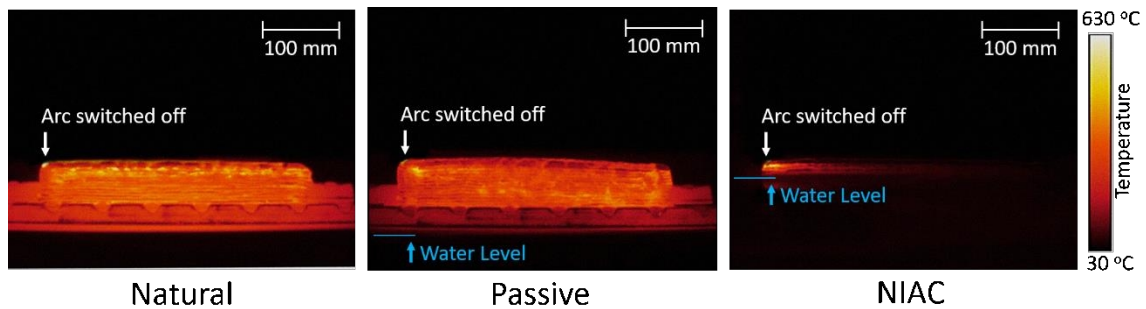
Figure 3.5. Thermograms taken of the lateral surface of the walls deposited under the different thermal management approaches right at the end of the 28th deposited layer

Complementing, now in quantitative aspects, Figure 3.6 shows the thermal cycles measured at fixed spots (at the mid length) on the substrates (left-hand side), along the whole deposition, and on the 23rd layers (right-hand side), during the execution of the last 5 layers. The peaks of temperature are consequence of the moments that the arc passes by above and vertically aligned with the points of measurement and the valleys correspond to the periods in between (representative of the interpass temperatures).
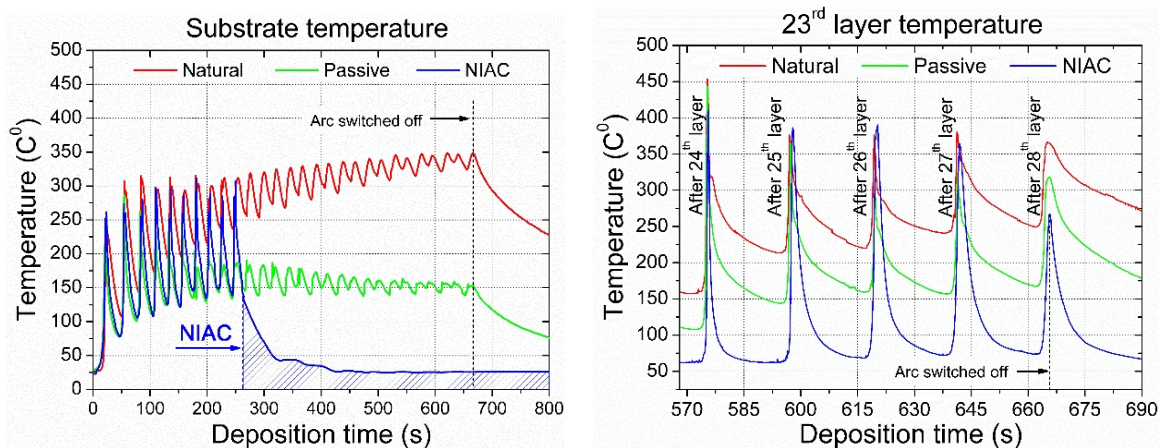

Figure 3.6. Thermal cycles simultaneously measured at fixed spots under the different thermal management approaches: values registered with a thermocouple fixed to the substrates at their mid lengths 5 mm from the deposition path centerline along the whole depositions (left-hand side); values extracted from thermograms taken of the 23rd layers at their mid length during the execution of the last 5 layers (right-hand side)

Under the Natural cooling approach, the substrate and the 23rd layer temperatures are seen to continuously rise as the layers are deposited and reach the highest levels observed, which is an evidence of the largest heat accumulation.

Specifically for the case of the temperatures measured at the substrate, each time the deposition source (electrical arc) gets far away in terms of height, the values tend to reach a maximum, almost averagely steady, level and then gradually reduce towards the room temperature, as reported by Denlinger et al. (2015). In this case, the heat input is balanced by the heat sink via conduction through the preform and to the substrate and to the building platform, convection to the air and radiation to the surroundings. However, as seen, after the end of the deposition, the temperature starts to fall as air cooling continuous.

For the Passive cooling approach, the same general trend is noticed. However, the substrate temperature seems to reach the almost averagely steady level much sooner (around 400 s) and it is significantly lower in value (around 150 ºC), indicating lesser heat accumulation. In this case, the conduction through the preform and to the substrate and to the building platform is boosted by the water convection around it, and so it is the heat sink. The 23rd layer temperature, in turn, continues to ascend until the end of the deposition time, yet with the valleys at lower levels than those reached with the Natural approach, but with a similar ascending rate. This fact suggests that the Passive cooling approach at this layer level is no longer effective to promote as much heat sink as it did for the first layers. This behavior corroborates observations made by Wu et al. (2017), who argue that there is a large discrepancy between the temperature measured at the substrate and the actual layer temperature, particularly if the dwell time in between layers is short or nil, as it is the case of the present evaluation.

Under the depositions with the NIAC technique, the first 9 layers were in fact deposited with the Passive approach and, as noticed, in the matched elapsed time the respective thermal cycles were very similar to each other. But as soon as the substrate was immersed by the rising water level (around 260 s), its temperature sharply dropped to the that of the water. The elapsed time till the water temperature is simply explained by the water convection sinking the substrate heat. The thermal cycles of the layers above the water level and then, as the preform is built up, also of the layers that are being immersed, cannot be detected by the thermocouple, since the heat flow by conduction through the preform is dissipated by the water convection before it reaches the substrate. It is also worth mentioning that there is a small water evaporation at the immersion level (water-preform contact). As the cooling power due to water phase transformation (specific heat) is much higher than that equivalent to water heating

(latent heat), it is believed that evaporation also significantly contributes to the heat sinking of the preforms.

Still regarding the NIAC technique, the 23rd layer valley temperatures (representative of the interpass temperatures) were the lowest, compared with the Natural and Passive approaches, and remained almost unchanged during all the deposition time, clearly showing no signs of heat accumulation. This behavior took place as expected, since the water level rises as the layers are deposited, keeping similar deposition conditions independently of the preform height.

3.3.2 Geometric quality

As typically shown in Figure 3.7, the NIAC technique promotes the tallest walls and a more regular and lower surface waviness. It also leads to lower variability of the wall height along its length, even near the ends. Such regions are critical for single-pass multi-layer bidirectional continuous (no dwell times) deposition of thin walls. They tend to become lower and wider than the rest of the wall extent due to local heat accumulation. It is important to clarify that the geometric quality at the ends of the preforms could be improved with the NIAC technique by switching the arc off and adding a short dwell time before starting the next layer. In addition, the wall deposited with the NIAC showed lower levels of surface oxidation, since it remained at lower temperatures during all the deposition time.

From the typical cross-sectional views displayed in Figure 3.8, it is visually confirmed that the tallest and slenderest walls are resulted from the NIAC application. Moreover, with this cooling technique the width of the preform remains virtually constant along its height, in contrast to what is verified for the Passive and, yet more intensely, for the Natural approach, which width significantly increases as the layers are deposited. This behavior can be explained by a molten pool enlargement due to heat accumulation. Despite the methodological nuances, Wu et al. (2018) reported a similar trend when using high interpass temperatures in WAAM of Ti6Al4V. The prominent width increase towards the top of the wall with the Natural cooling approach is a clear evidence of the largest heat accumulation in such a case.
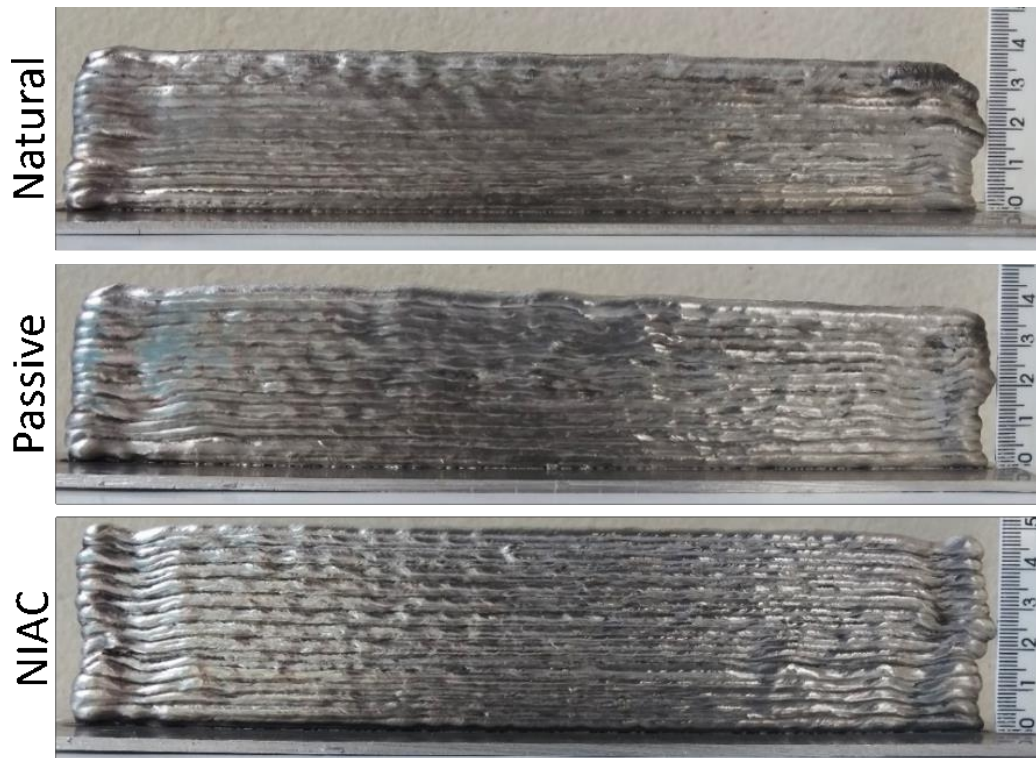
Figure 3.7. Typical aspects of the walls (after cleaning with a manual brush) deposited under the different thermal management approaches and with the same deposition settings and number of layers
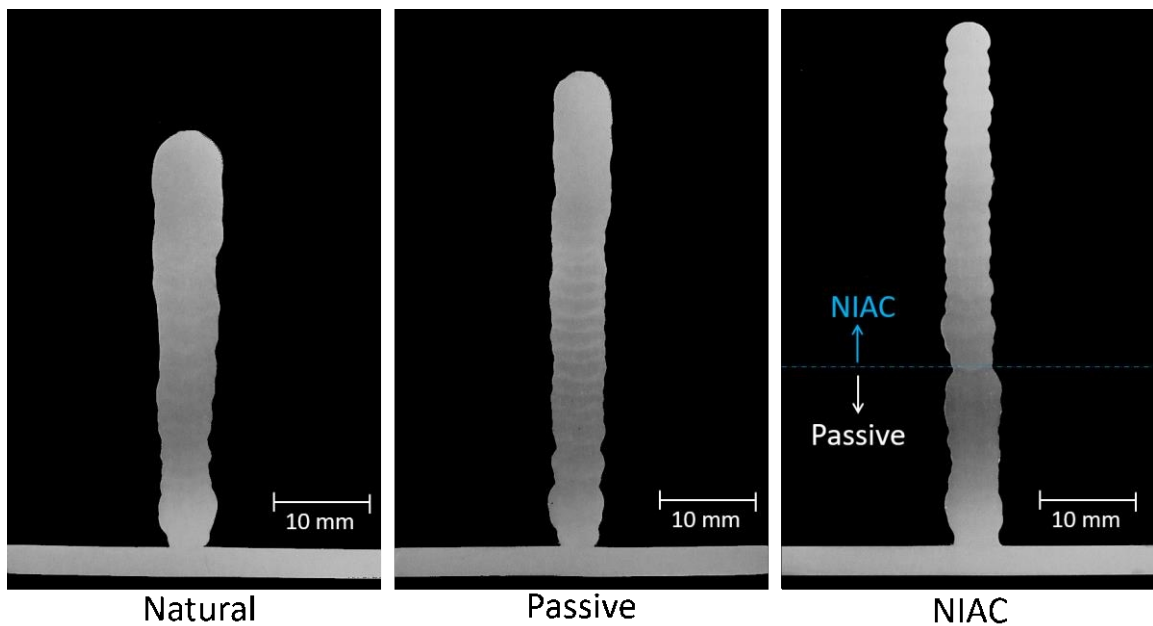

Figure 3.8. Typical cross-sectional views of the walls deposited under the different thermal management approaches and with the same deposition settings and number of layers

3.3.3 Porosity assessment

It is widely recognized that hydrogen is the dominant cause of porosity in aluminum alloy weld beads. Due to closeness of arc welding and additive manufacturing operations and in face of the possibility that water vapor might hydrate the Al-oxide films and/or even contaminates the deposition pool and/or the electric arc, one can say that porosity is the major concern related to the application of NIAC in WAAM of aluminum. However, as shown in Figure 3.9, for all thermal management approaches the walls showed low porosity levels and within a range to what has been reported in the current literature (Haselhuhn et al., 2016; Ryan et al., 2018).
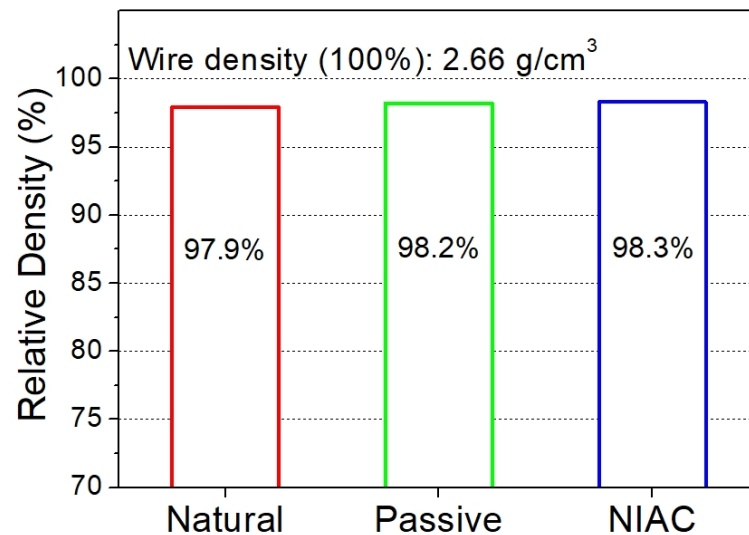

Figure 3.9. Effect of the different thermal management approaches on the relative density (Archimedes method)

Although there is a large amount of information about porosity on WAAM of aluminum alloys, only few works have evaluated the pore evolution. Gu et al. (2016) investigated the effect of post-deposition heat treatments on the porosity of 2319 and 5087 aluminum parts built with WAAM and reported porosity increase due to exposition at 535 ^{o}C for 90 minutes for both alloys, but pore growth was more intense in the 5087 alloy. These authors advise that a high-temperature heat treatment may cause serious secondary porosity problems, which makes the mechanical properties worse. Derekar et al. (2018), who evaluated the effect of the interpass temperature on the porosity of 5356 aluminum parts built with WAAM, reported larger pores at the fusion line for a

lower interpass temperature due to a longer cooling time, that, in their opinion, could have allowed hydrogen diffusion and pore coarsening to happen. From these results, one can expect an in-situ pore evolution due to heat accumulation in WAAM.

With that issue in mind, micrographs were performed at longitudinal sections taken from the central region of the preforms here evaluated. As typically shown in Figure 3.10, voids newly formed inside the last layers have a sound spherical shape and a similar size range for all the thermal management approaches assessed. With the NIAC technique, the voids inside the first layers remained virtually unchanged, which is in accordance with the lower temperatures assured by the water level constant rise. In contrast, for the Natural and Passive approaches, the irregular morphology of the voids suggests the possibility of intra-pore coalescence and/or trapped hydrogen expansion, both due to a higher temperature exposure (heat accumulation), resembling what has been observed by Toda et al. (2009). Gu et al. (2016) warn that high-temperature heat treatments of aluminum parts built via WAAM may cause serious secondary porosity problems, which worsen mechanical properties. Larrosa et al. (2018) reported similar issues in AlSi10Mg parts built with PBF.
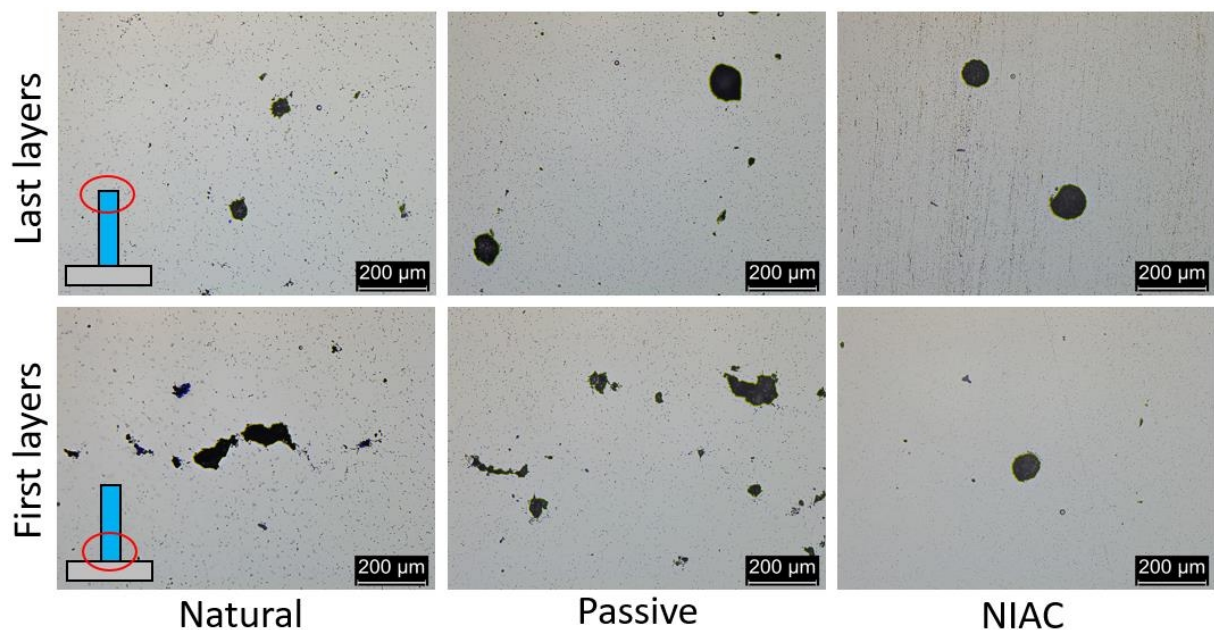

Figure 3.10. Effect of the different thermal management approaches on the morphology of voids according to the location in the preforms (longitudinal sections sampled from regions with more incidence of voids)

In summary, the use of water in the thermal management technique conceived near the deposition pool and electric arc, at least for the deposition settings adopted, is not a risk factor concerning hydrogen-induced porosity. This NIAC feature might be related to the positive pressure undergone by the deposition poll and its surroundings due to the shielding gas flow, which pushes water vapor, that is formed nearby even with large volumes of water in the work tank, away from the deposition location.

3.3.4 Microstructural texture assessment by XRD

As the 5356 aluminum is a non-heat treatable alloy, no significant changes are distinguished by examining the XRD patterns showed in Figure 3.11. Nonetheless, a qualitative analysis of the ratio between the intensities of the main peaks suggests a microstructural texture imposed by the thermal management techniques applied. As seen, the NIAC technique, different from the Natural and Passive approaches, fits well with the standard diffraction pattern for the α aluminum phase (PDF # 040787). Similar strategy was used by Zou et al. (2018) to assess the microstructure texture of Ni-Fe parts built via PBF.
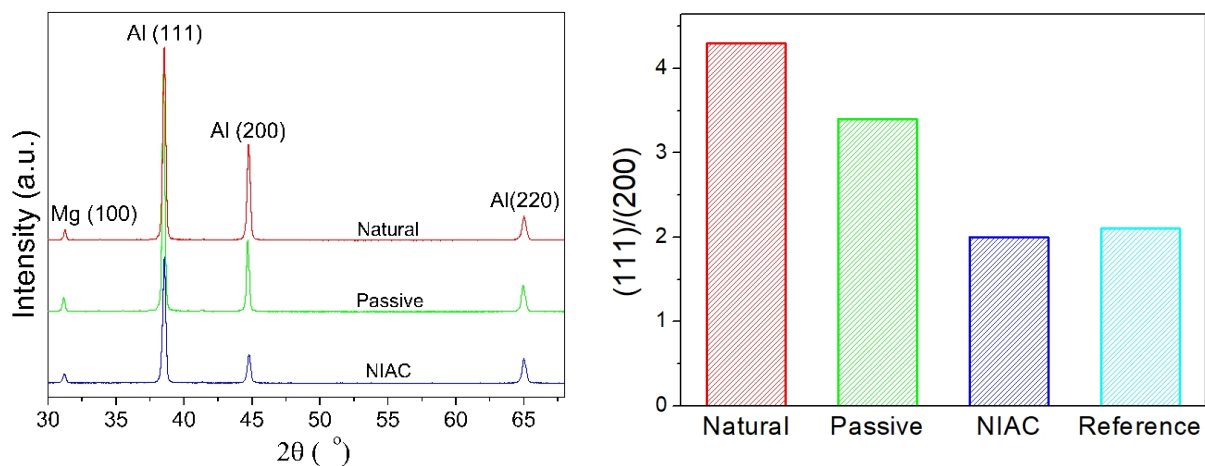

Figure 3.11. XRD patterns and the ratio between intensities of the two main peaks from parts built with the different thermal management approaches

3.3.5 Mechanical properties

Figure 3.12 illustrates the typical stress-displacement curves according to the thermal management approaches, being the resultant mechanical behavior under tensile loading noticeably different for each case. As compiled in Figure 3.13 (left-hand side), all cooling conditions statistically exhibited equal mean ultimate tensile strength (UTS) values, regardless the direction (vertical and longitudinal) of the preform growth. In addition, the mean UTS numbers fell inside the typical range reported in the current literature (from 250 to 320 MPa) for WAAM of similar alloys (Horgar et al., 2018; C. Zhang et al., 2018). In contrast and as gathered in Figure 3.13 (right-hand side), the final displacement (FD) values, employed as a ductility scale, exhibit significant differences between the vertical and longitudinal directions for the Natural and Passive cooling approaches, indicating anisotropy to some extent, which is certainly linked to the respective heat accumulation that took place in each case. In contrast, the NIAC technique clearly equalizes the ductility measure concerning the direction of the preform growth, suggesting the existence of an anisotropy-mitigation effect. This behavior could be explained considering the formation of spherical voids with the NIAC technique, as presented in Figure 3.10, which could lead to superior mechanical properties. In addition, it is reasonable to consider that pore morphology has a greater effect on the mechanical properties than microstructural texture as observed in the XRD patterns.
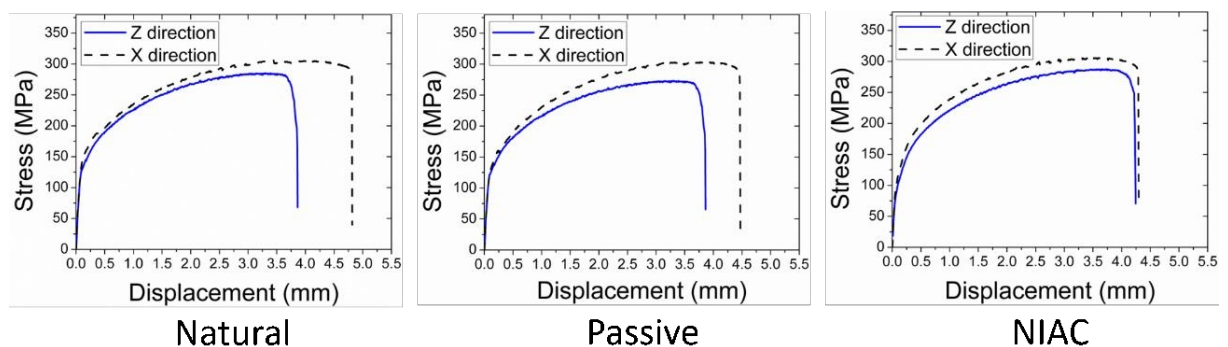

Figure 3.12. Typical stress-displacement curves according to the direction of the preform growth under the different thermal management approaches
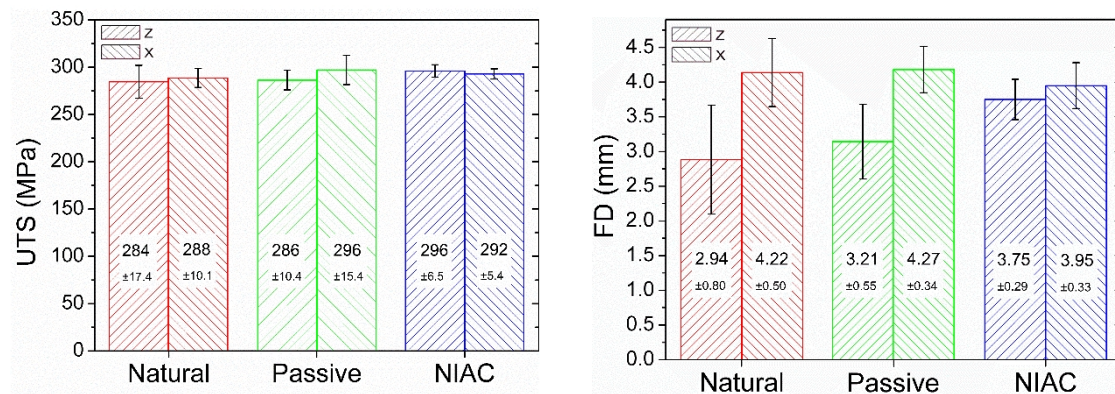
Figure 3.13. Effect of the different thermal management approaches on ultimate tensile strength (UTS) and final displacement (FD) according to the direction of preform growth

3.4 Partial remarks about the NIAC

- The high heat sink power of this technique can keep the preforms at lower temperatures during all the deposition time, independently of their heights;

- Under this cooling technique, wall-shaped preforms become slender and taller and exhibit virtually constant widths;

- This technique is also a boosting factor towards preforms with isotropic mechanical properties;

- The use of water in this technique does not lead to any measurable increase in porosity; and

- Thus, in view of the novelty of this thermal management technique as devised and as compared with the state of the art verified from the scientific (papers) and technological (patents) background, considering the related inventive activity as just described along the initial stages of its proof of concept, and given its resultant potential for industrial application, the NIAC was filed in the National Institute of Industrial Property (INPI) as an invention (utility patent), as detailed in Reis et al. (2018).

3.5 Difficulties observed

- Keeping a constant LEWD by hand during all the deposition time;
- Guaranteeing the arc ignition and turn-off at the same position; and
- The lack of a dwell time in between the layers.

CHAPTER IV - DEVELOPMENT OF A FUNCTIONAL PROTOTYPE OF THE NIAC

4.1 Functional prototype description

From the knowhow gained with the proof-of-concept experiments, a NIAC functional prototype was developed, as showed in Figure 4.1.
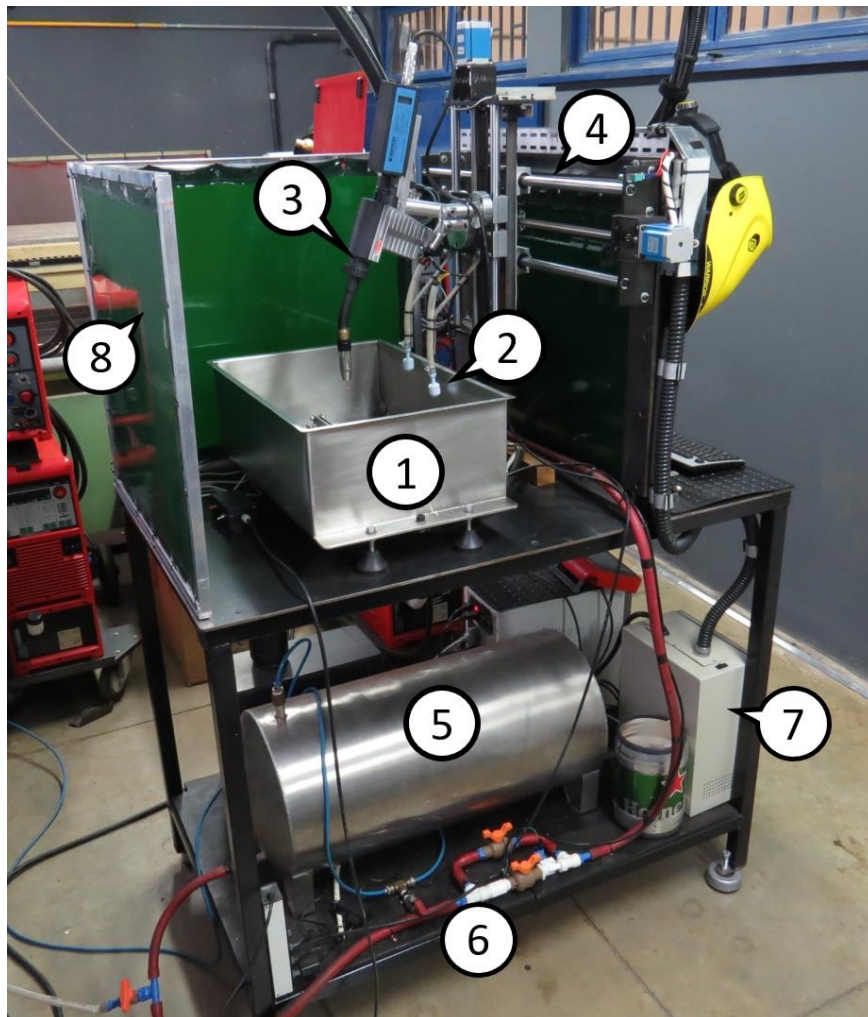

Figure 4.1. NIAC functional prototype overview: (1) work tank; (2) float switch (3) CMT torch; (4) motion system; (5) pressurized water tank; (6) hydraulic and pneumatic system; (7) CNC controller; and (8) protection curtain

Basically, the NIAC functional prototype is a structure of 70 x 130 x 200 cm (width x length x height) made with low carbon steel square tube of 50 x 50 mm with 2 mm of thickness. Also, there is a low carbon steel 10 mm thick top plate for general support of equipment. The motion system is placed on a gantry, while the work tank is kept static on the top plate. The motion system contains sliding bearings under linear guides (Ø 20 mm), ball screws (Ø 16 mm with a pitch of 5 mm) and stepper motors (NEMA 23). The work tank is a stainless-steel vat of 48 x 36 x 30 cm (50 L) under rubber feet to insulate it from the top plate. The ground cable is connected at both ends of the working tank to avoid arc magnetic blow. The water level is controlled by a magnetic float switch, which switches a solenoid valve to raise the water level as the layers of metal are deposited (z-axis increment). The water goes up to fill the work tank by pressure difference from an internal tank and returns to it by gravity after deposition is finished so it can be reused. On a bottom plate there is a pressurized water tank of 100 L, a hydraulic and pneumatic system (solenoid valve, ball valves, hoses, etc.), and the CNC controller (switching for the power supply, driving for the stepper motors, CNC interface board and computer). Protective curtains are used to mitigate the arc radiation in the environment during deposition but does not eliminate the need for personal protection equipment. In addition, an exhaust system nearby is used to reduce the generated fumes in the surroundings.

The CNC system is controlled by a Mach3® software, which is normally used in plasma cutting machines and CNC routers. The programming language is based on the G-code. The programs for the deposition path can be done by hand or by CAM software with adequate post processing. In fact, for ordinary geometry, manual programming is easier and more flexible.

Williams et al. (2016) claimed that whenever possible, GMA[1] is preferable for WAAM because the wire is coaxially fed, which results in easy tool path execution. The NIAC functional prototype uses a Fronius Cold Metal Transfer (CMT) welding system. The deposits with excellent quality, lower thermal heat input and nearly without spatter qualify the CMT as suitable for WAAM. Since the arc length can be maintained very short, the arc pressure on the molten pool is small. In addition, heat is transferred to

---

[1] According to ASTM (2015), the word "welding" in the AWS definition conveys the joining of two or more pieces of material. As this is not the case for DED, the word "welding" is dropped. The remaining term characterizes the arc physics.

the material in a very regular basis. These two characteristics imply that the molten pool is very controllable, as demanded to build up thin walls.

4.2 Instrumentation and calibration

4.2.1 Geometric accuracy of the machine

The straightness and perpendicularity of the axes in relation to the top plate were adjusted with a dial indicator and a square tool. The positional deviation, according to the definition found in the ISO 230-2 standard guide for machine tools, did not exceed 0.020 mm along the working range. Although there is no specific standard guide for the accuracy of AM machines, this value looks sound considering the typical geometrical features of preforms built with WAAM, as summarized in Table 4.1.

Table 4.1. Geometrical features of preforms built with WAAM

Parameter	Value	Reference
Dimensional accuracy*	0.2 mm	Ding et al. (2015)
Layer thickness	1.0 - 2.0 mm	Williams et al. (2016)
Surface waviness	0.5 mm	
Minimum feature size	2.0 mm	

* Distortions induced from residual stresses could affect accuracy (Ding et al., 2015).

4.2.2 Motion system

The calibration of the motion system is important to ensure that the programmed dimensions and speeds are correct. This was done by a dedicated routine in the Mach3® software, which sets the ratio step/mm through an interactive process. The idea is to execute a movement with a programmed length, measure it and inform the actual length in the software, that then resets the parameter step/mm. The calibration procedure was repeated until the programmed value equaled the measured value.

4.3.3 Water level system

The top plate level was checked with a spirit level to ensure a constant LEWD all over the working area. The control of the water level was accomplished by means

of a magnetic float switch as shown in Figure 4.2. This element switches a solenoid valve and it then raises the water level as the layers of metal are deposited (z-axis increment). Preliminary tests were carried out to determine the work pressure of the pressurized water tank. If the pressure is too low the level will take time to rise, but if it is too high it will cause excessive water turbulence. In addition, tests were performed to set the float switch resolution, *i.e.*, the minor vertical movement to activate it. Finally, tests were carried out to determine the time needed to raise the water level to common layer heights and to stabilize it. This information is important to set up a minimum interpass dwell time. Table 4.2 summarizes the water level control characteristics.
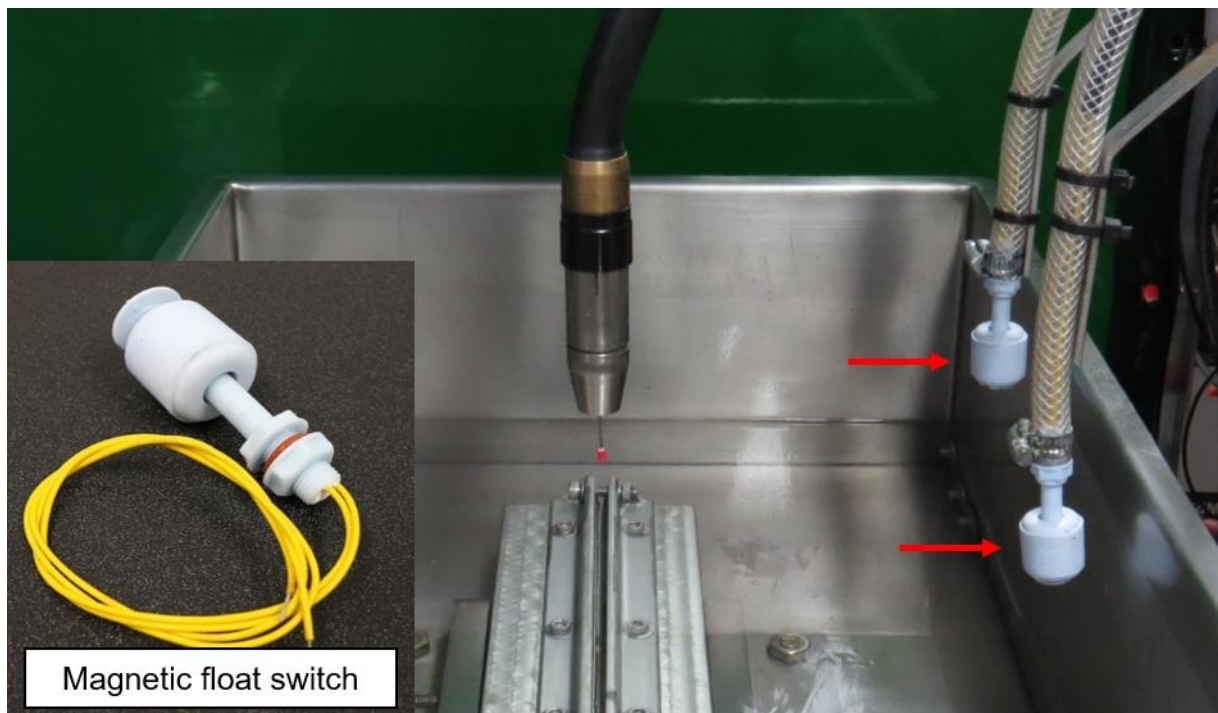

Figure 4.2. Magnetic float switch used to control the water level

Table 4.2. Water level control characteristics

Work pression of the pressurized water tank	1 bar
Resolution of the magnetic float switch	1 mm
Response time to raise the water level	2.1 s/mm

Note: these characteristics are valid for the tested conditions

4.3.4 Deposition parameters

A data acquisition system (DAQ) developed by Machado (2011) was used to measure the deposition parameters: voltage, current and wire feed speed. In this DAQ,

the correspondent transducers signals are conditioned in a dedicated electronic interface and acquired by an A/D commercial board at a rate of 5 kHz and 14 bits.

The voltage and current signals were calibrated using a load bank developed at Laprosolda-UFU (Figure 4.3). The load bank is composed of a stainless-steel pipe and its electrical resistance can be varied by changing the position of the clamp highlighted in Figure 4.3. The load bank is cooled by water circulation to keep the electrical resistance almost constant during the calibrations process.
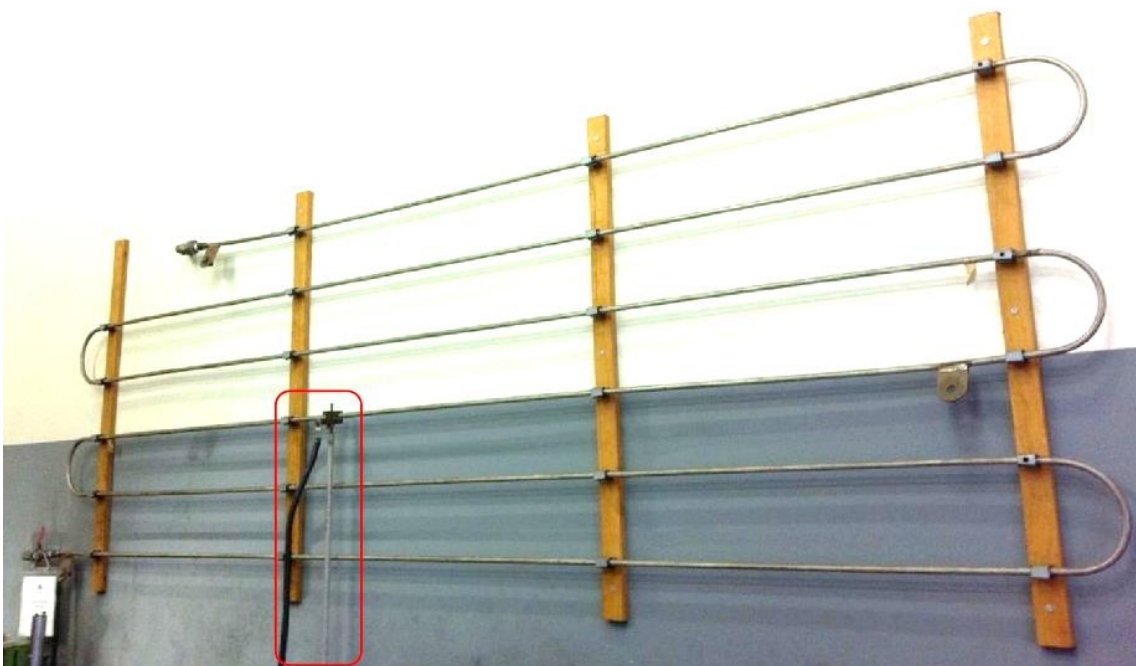

Figure 4.3. Load bank used to calibrate the output signal from the interface conditioner (current and voltage)

The current and ground cables of a welding/AM power source are attached to the load bank terminal and to the clamp (Figure 4.3). A current transducer (hall effect sensor) and a calibrated current clamp were attached to the current cable, while probes for measuring voltage and a calibrated voltmeter were attached to the welding/AM power source terminals. The current imposed by the welding/AM power source was varied in a range from - 450 to 450 A at steps of 50 A. Table 4.3 summarizes the calibration values, while Figure 4.4 presents the current and voltage calibration curves.

Table 4.3. Calibration of the current and voltage signals

| Welding/AM power source	DAQ output		Voltmeter	Current clamp
Regulated current (A_m)	Voltage signal	Current signal	Voltage [V_{RMS}]	Current [V_{RMS}]
-450	-8.16	-4.50	-54.00	-437.30
-400	-7.24	-3.99	-48.00	-388.60
-350	-6.35	-3.49	-42.00	-340.50
-300	-5.43	-3.00	-36.00	-292.10
-250	-4.54	-2.50	-30.00	-243.90
-200	-3.62	-2.00	-24.00	-195.40
-150	-2.72	-1.50	-18.00	-146.90
-100	-1.82	-1.00	-12.00	-98.50
-50	-0.91	-0.50	-6.00	-50.10
50	0.89	0.53	6.00	49.10
100	1.79	1.02	12.00	97.20
150	2.70	1.52	18.00	145.30
200	3.61	2.02	24.00	193.50
250	4.51	2.52	30.00	241.80
300	5.40	3.02	36.00	290.00
350	6.32	3.52	42.00	337.90
400	7.20	4.02	48.00	386.00
450	8.11	4.52	54.00	434.20
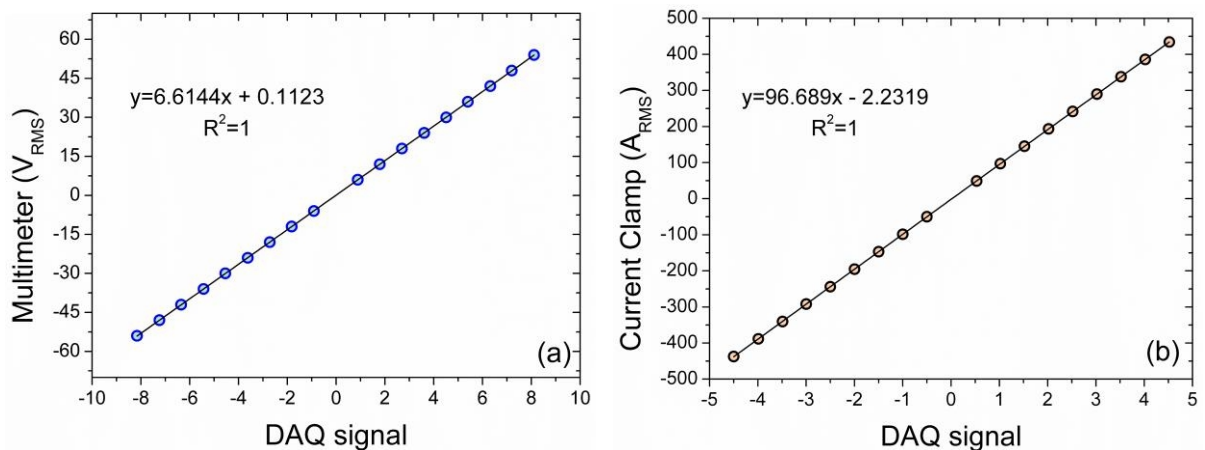
Figure 4.4. Calibration curves for the (a) voltage and (b) current signals

The wire feed speed (WFS) measurements were performed by an optical encoder-based system clamped to the wire, as shown in Figure 4.5. This optical encoder has a disk with 50 slots and the output signal from this transducer is a squared wave with amplitude of 5 V. As the frequency of this signal is proportional to the WFS, the DAQ signal calibration was performed using a function generator. The frequency range used (5-190 Hz) for the calibration was estimated based on the WFS capabilities

of CMT welding/AM power source (22 m/min in the pulsed mode). The disadvantage of using a function generator to calibrate the WFS signal is that it does not account for the response time of the transducer. For validating simulations carried out with the function generator and the WFS predicted by Eq. 4.1, actual WFS tests were performed using a stopwatch and a reference guide 2 meters long. Table 4.4 summarizes the calibration by the two methods used and Figure 4.6 presents the resultant calibration curves. As one can see, both the calibration curves are quite similar, which means that the predicted WFS can be taken as valid.
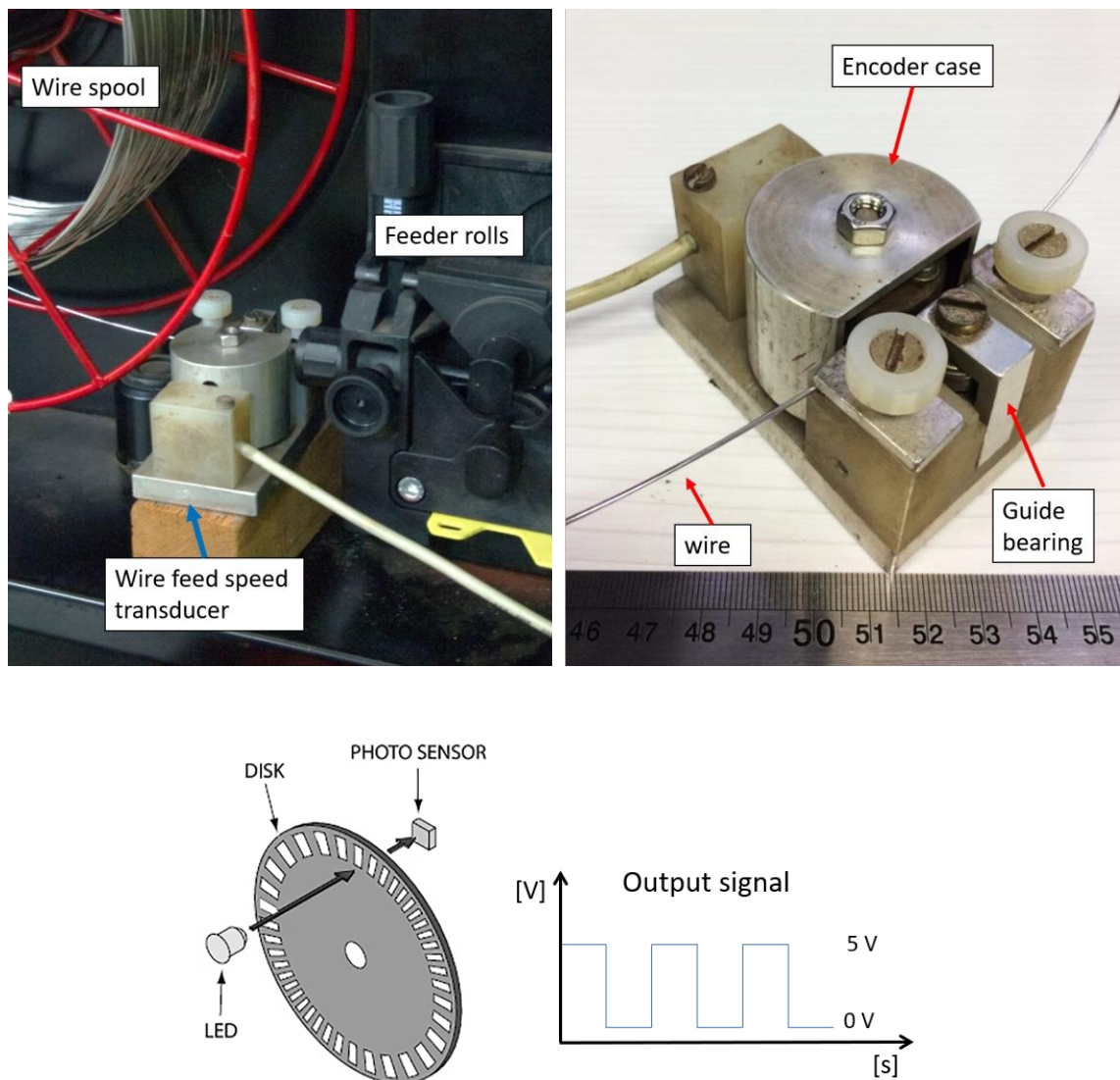

Figure 4.5. Wire feed speed measurement system and respective transducer details

$$WF\ S_{predicted} = \frac{(\pi * \emptyset_{roll} * f) * 60}{N_{slots} * 1000}$$
Eq. (4.1)

where:

- WFS$_{predicted}$: wire feed speed predicted [m/min];

- Ø$_{roll}$: roll diameter [mm];

- f: squared wave frequency [Hz]; and

- N$_{slots}$: number of slots of the encoder disk.

Table 4.4. Calibration results for the WFS using a function generator and by actual measurements

| Function generator		Measurements	
WFS$_{predicted}$ [m/min]	DAQ signal	WFS$_{actual}$ [m/min]	DAQ signal
0.603	0.107	0.605	0.097
1.209	0.205	1.265	0.213
2.419	0.408	1.949	0.328
3.626	0.621	2.600	0.436
4.837	0.816	3.226	0.542
6.047	1.006	3.788	0.640
7.255	1.214	4.238	0.732
8.463	1.428	4.877	0.825
9.675	1.621	5.428	0.917
10.886	1.835	6.473	1.095
12.094	2.025	7.560	1.278
13.303	2.224	8.642	1.458
14.519	2.434	9.688	1.637
15.716	2.633	10.736	1.814
16.931	2.832	11.807	1.989
18.153	3.029	12.842	2.165
19.350	3.237	13.972	2.341
20.547	3.433	15.026	2.515
21.781	3.639	16.086	2.690
22.990	3.839	17.087	2.870
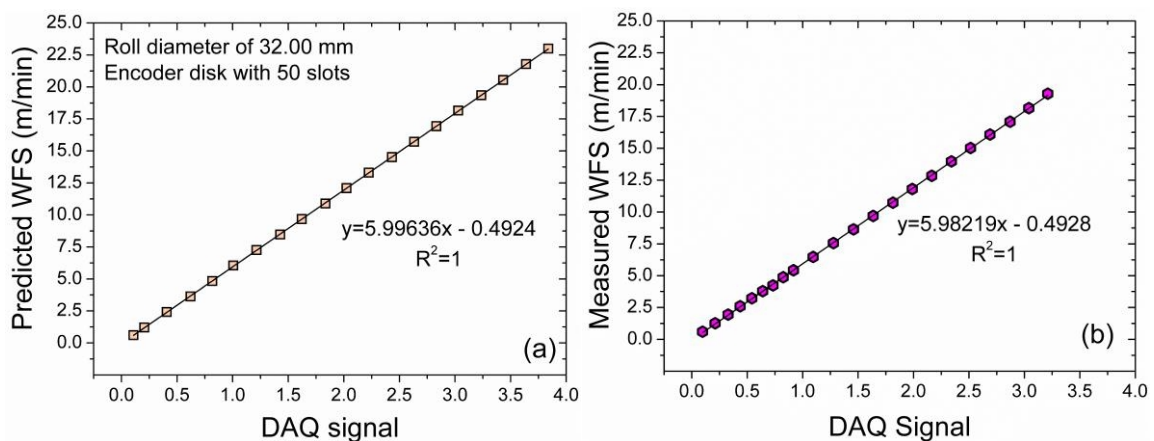
Figure 4.6. Calibration curves for the WFS according to the (a) prediction and (b) measurement methods

4.3.5   Interpass temperature and thermal history system

According to the ASTM F3187 – 16 standard guide (ASTM, 2016), the interpass temperature may be a key variable for certain DED processes and materials. However, Wu et al. (2017) advised that if the temperature measured at the substrate is taken to be the interpass temperature, it will cause large errors. They argue that there is a large discrepancy between the temperature measured at the substrate and the actual interpass temperature, particularly if the dwell time in between layers is short. They further claim that in-situ measurement of the layer surface temperature using non-contact techniques provides far more accurate and reliable data. In addition, Hagqvist et al. (2013) mention that contact measurement methods are impracticable because of the layer-by-layer approach of AM.

According to Hagqvist et al. (2013), due to the availability of pyrometers with focusable optics, measurements with a small spot for high spatial resolution are an option besides thermal cameras. The thermal cameras make data analysis harder, since surface characteristics vary over the examined area. Also, there is a higher risk of the camera optics focusing at plasma reflections. This risk is mitigated when using an infrared (IR) pyrometer together with a focusing optical head that difficult stray reflections to hit the detector.

Figure 4.7 shows the experimental arrangement used for measuring the preform temperature in the NIAC functional prototype. In this arrangement, there are two IR pyrometers of the same kind. The first one was attached to the motion system and was used to measure the interpass temperature. The second one was fixed at the top plate by using a magnetic base and was used to measure the thermal history of a point of interest (fixed target) during the deposition until the water level reaches it. Table 4.5 summarizes the specification of the IR pyrometers used. The water temperature inside the work tank was checked regularly via a simple thermocouple.

The hindrance in using IR pyrometers is that an accurate temperature measurement requires knowledge of the object's emissivity. Hagqvist et al. (2013) argue that generally there are no data about temperature and wavelength dependency on emissivity for commercial alloys. Neither does the available data consider the surface oxidation, which is an inevitable consequence when heating reactive metals, such as aluminum, in the presence of oxygen. Therefore, one of the most prominent

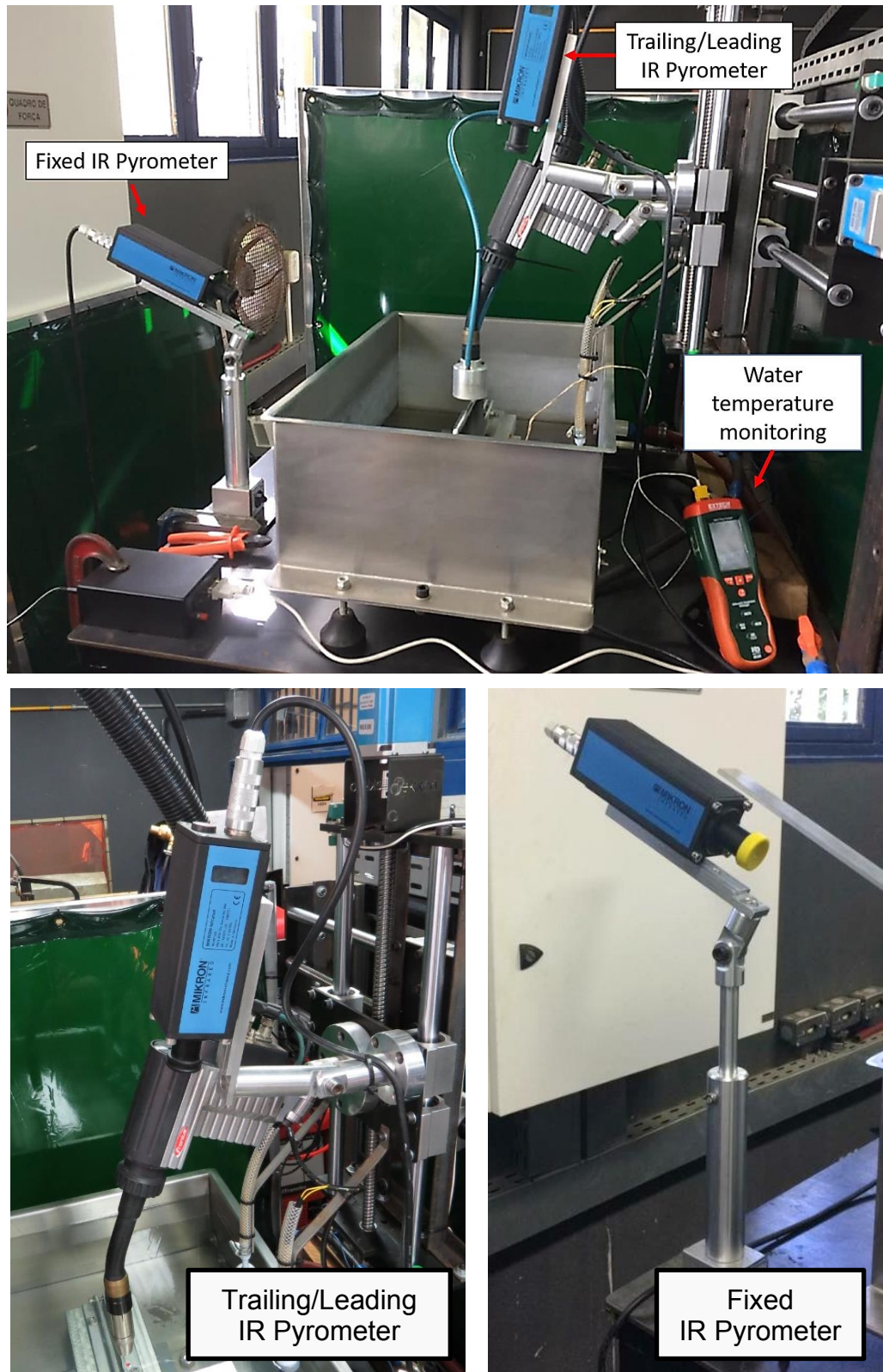sources of uncertainty in IR pyrometry is the estimation of de measurand surface emissivity.

Figure 4.7. Experimental setup for measuring the temperature of the preforms and of the water during deposition

Table 4.5. Specification of the IR pyrometers used (LumaSense, 2019)

IR pyrometers	Mikron MI-PE140 with focusable optics
Spectral range	3-5 μm
Temperature range	30-1000 °C
Spot size	Ø 2.9 mm at a distance of 380 mm
Resolution	0.1 °C

Although there are several methods to find out the emissivity of a material, many of these methods are restricted to a laboratory scenario. Experiments performed by Brandt et al. (2008) showed that surface emissivity can be estimated by means of a reference paint applied to the surface to be measured and comparing the radiation from the uncoated surface with the radiation from the reference paint. Also, the emissivity of a surface can be estimated by comparing its temperature to the temperature inside an electrically heated cavity (Figure 4.8). Due to multiple reflections, the emissivity is nearly 100% inside the cavity.
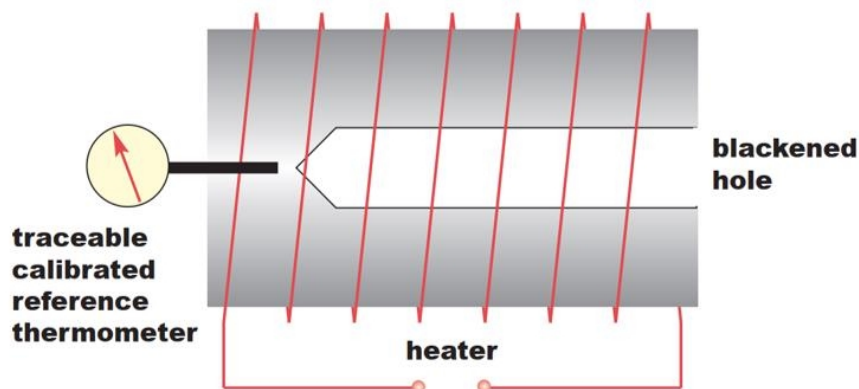

Figure 4.8. Calibration radiator used to determine the emissivity of a surface (LumaSense, 2019)

One of the most common approaches for adjusting the emissivity is by comparing the IR pyrometer temperature with a thermocouple data. In the present work, the data from a 0.6 mm diameter (each wire) K-type thermocouple was used to adjust the emissivities of the IR pyrometers. For that, a few layers were deposited, then the thermocouple was attached to the side of the last layer and the pyrometers were focused to points very close to it. As a first approximation, emissivities of 15% were used as suggested by the manufacturer of the pyrometers (LumaSense, 2019). Then the emissivity of the trailing/leading IR pyrometer was corrected for 20%, while the one

for the fixed IR pyrometer was corrected for 22%, both to match the thermocouple data. This difference in the emissivities could be related to smut formation at the lateral surfaces of the preforms, as shown in Figure 4.9. The smut formation is related to the evaporation of elements with low boiling point like Al and Mg. In fact, the welding literature reports the Mg loss due to evaporation. These metallic vapors might oxidize and condense on the relatively cool weld bead or layer and parent material nearby.
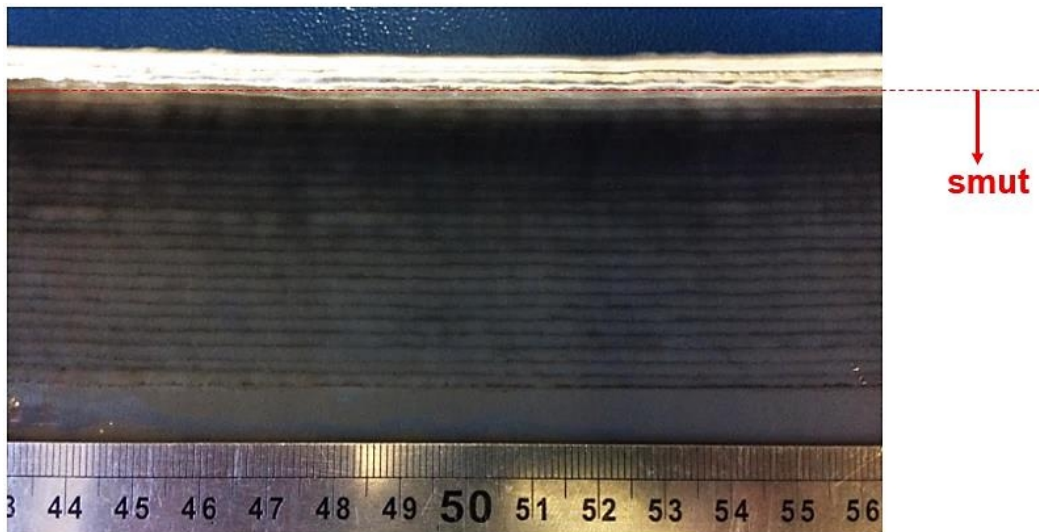

Figure 4.9. The smut formed at the lateral surface of a wall-like preform (by the author)

4.4 Functionality assessment

4.4.1 Experimental approach

Wall-like preforms were deposited with different LEWD values to evaluate the functionality of the water level control system, as well as the effect of the LEWD on the geometric features, porosity and interpass temperature of the preforms. Moreover, walls of different lengths were deposited to test the concept of the NIAC in terms of a condition with deposition concentration, *i.e.*, small details in large components (localized heat accumulation). The deposition settings used for the validation tests are summarized in Table 4.6.

Table 4.6. Deposition settings used for the functionality assessment of the NIAC prototype

Arc deposition equipment	Fronius CMT – TransPuls Synergic 500
Wire (deposition material)	AWS ER 5356 – Ø 1.0 mm
Substrate	Al5052 (330 x 38.1 x 6.35 mm)
Wire feed speed	7.6 m/min
Deposition speed	60 cm/min
CTWD*	12 mm
LEWD**	5 -10 -15 - 30 mm
Shielding gas	Commercial argon at 13 - 15 L/min
Cooling liquid	Tap water
Work tank volume	50 L
Preform geometry	Single wall with 20 layers
Building strategy	Single-pass multi-layers bidirectional depositions
Dwell time	5 s/layer

The measured resultant average deposition current and arc voltage levels were 96 A and 8.5 V. respectively. *CTWD = contact tip to work distance; **LEWD = layer edge to water distance

The porosity level was estimated by the Archimedes method. According to Spierings and Schneider (2011), the Archimedes method delivers more reliable results as the whole sample volume is considered instead of only single cross sections, which might not represent a typical porosity of the whole sample. In addition, the Archimedes method is the most economic and fast procedure for that purpose compared to other common methods (microscopy and computerized tomography). For these measurements, a digital balance with a resolution of 0.01 g and distilled water were used. The preforms were cut from the substrate in samples with around 100 g. The porosity was estimated from the density of a reasonable sample of the Al wire used (100 g) that was calculated by using this method. Three measurement trials were performed for each sample both in the air and in the water. First, all samples were weighted in the air to prevent the water from infiltrating in the superficial defects. Care was taken to ensure that air bubbles were not present on the samples under testing. The results are presented in terms of volume of voids, since the eventual presence of internal cracks and/or lack of fusion defects may affect the porosity results.

Figure 4.10 shows the infrared pyrometer (IR) arrangement employed for measuring the interpass temperature. Data from a 0.6 mm diameter (each wire) K-type thermocouple was used to adjust the pyrometer emissivity to 22%. The pyrometer measuring spot target was kept close but at 30 mm from the arc center, as the signal got very noisy for shorter distances.
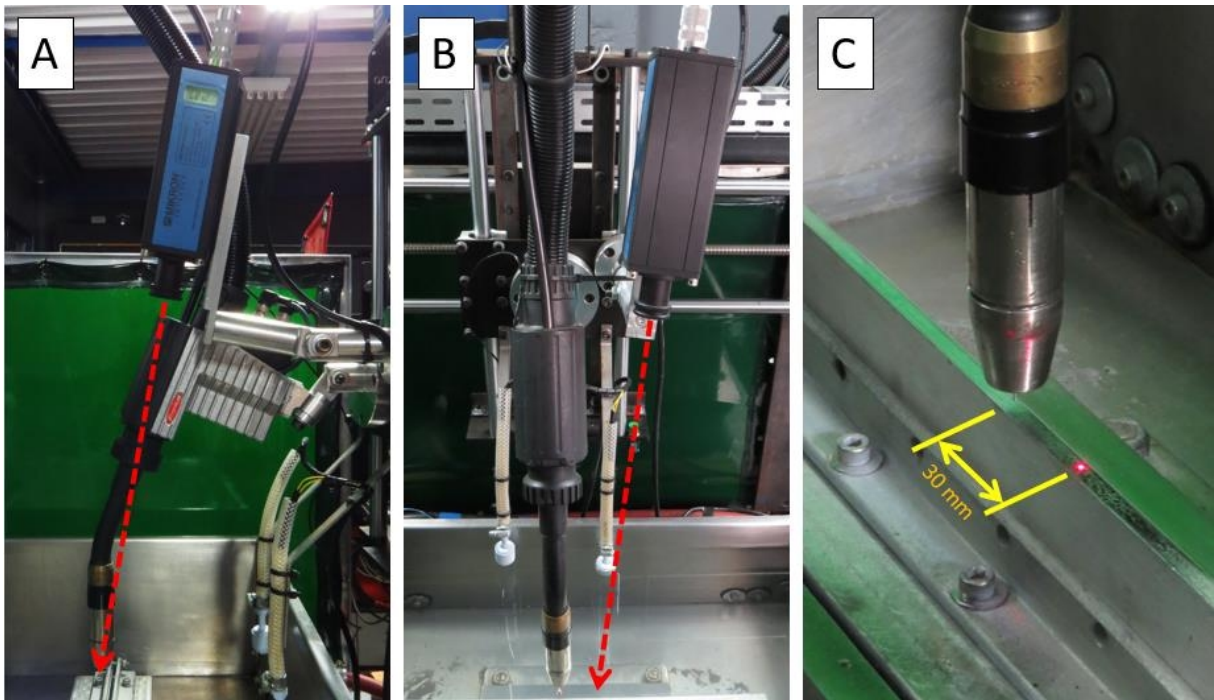
Figure 4.10. IR pyrometer arrangement for the functionality assessment of the NIAC prototype: (A) front view; (B) lateral view; (C) measuring spot target

4.4.2 Functionality results

The water level control through the magnetic float switch was able to keep the LEWD constant during all the deposition time. The deposition process remained stable even when operating very near the water (LEWD of 5 mm), but in this case there was turbulent water evaporation at the ends of the preform due to local heat accumulation (torch reversal). To mitigate this issue, only for the LEWD of 5 mm, the wall length was decreased by 5 mm after each layer, as illustrated in Figure 4.11.

Figure 4.11. For the LEWD of 5 mm, the length of the wall was decreased by 5 mm after each layer to mitigate turbulent water evaporation at the ends of the preform

As expected, the LEWD influences the visual and geometric aspect of the walls. As shown in Figure 4.12, for lower LEWD values (water closer to the deposition level) the lateral surface waviness tends to be higher and the top surface more undulated. For the Natural condition, the surface of the walls got rougher and assumed a matte aspect, which may be related to the heat accumulation and/or to an insufficient protection with the shielding gas. Unlike welding, where shielding gas hits the plate

and spreads around, in WAAM the shielding gas tends to flow along the sides of the thin wall without spreading.
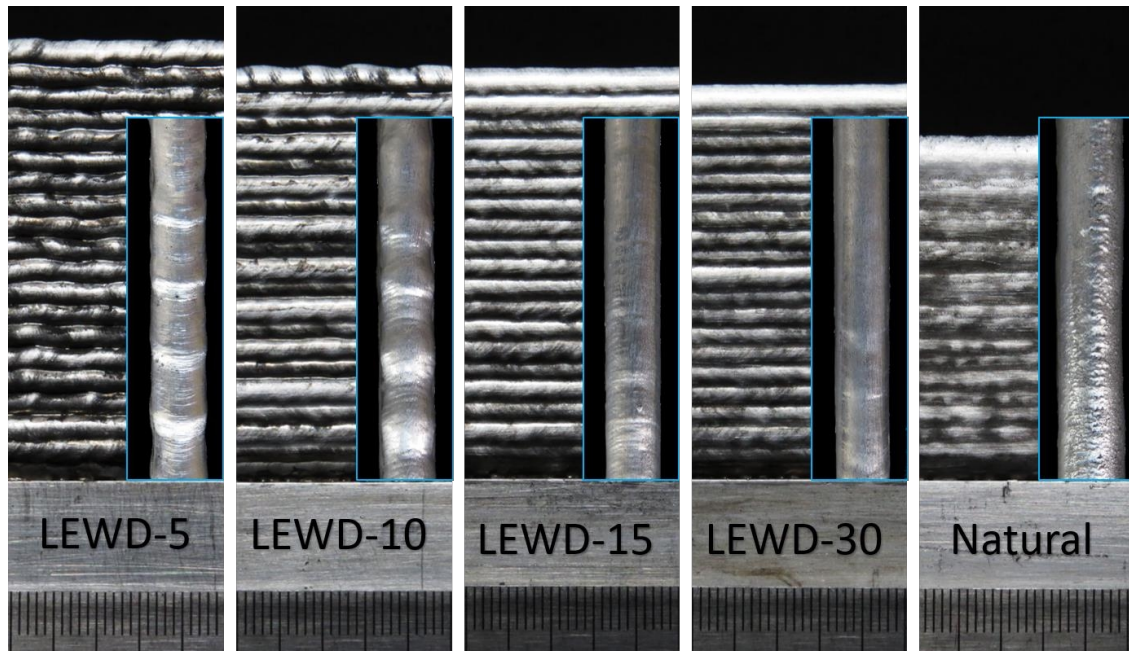

Figure 4.12. Effect of the LEWD on the aspect of the lateral and top surfaces of the preforms

From the cross-sectional views showed in Figure 4.13, it is clear that the walls deposited under the NIAC technique are taller and slender than those ones produced under the Natural approach. Also, it can be observed that under the Natural cooling approach the walls are more irregular and tend to become wider along the height. This behavior is related to molten pool enlargement due to both the heat accumulation and the excessive oxidation. Regardless of the surface waviness, the width of the walls deposited with the NIAC technique is almost constant along the height (parallel sides).

As shown in Figure 4.14, the variation of the LEWD had no significant effect on the total width (external width), while the effective width increased with increasing LEWD values. This result suggests that the higher the LEWD (weaker heat sink effect), the greater the volume of the anterior layer that is remelted. This agrees with the analytical model proposed by Ríos et al. (2018), which predicts that the surface waviness depends on the remelted volume. The relationship between the surface waviness and the LEWD value has a minimum for a LEWD between 15 and 30 mm. This minimum value of surface waviness is in concordance to what was postulated by Williams et al. (2016).
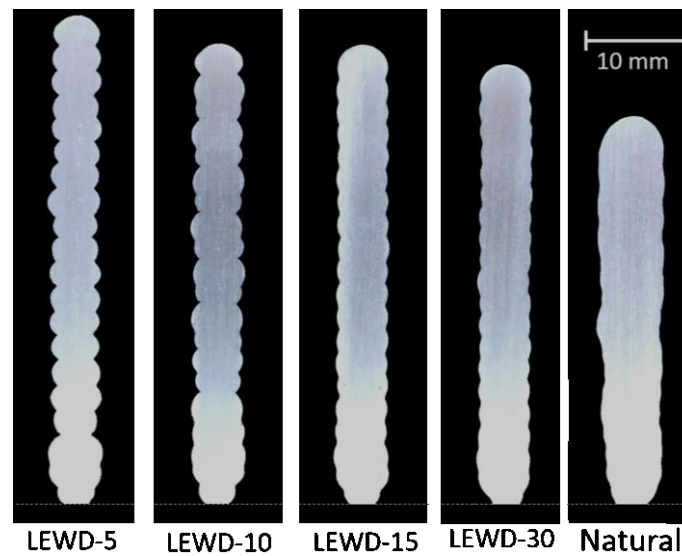
Figure 4.13. Effect of the LEWD on the geometrical quality of the walls
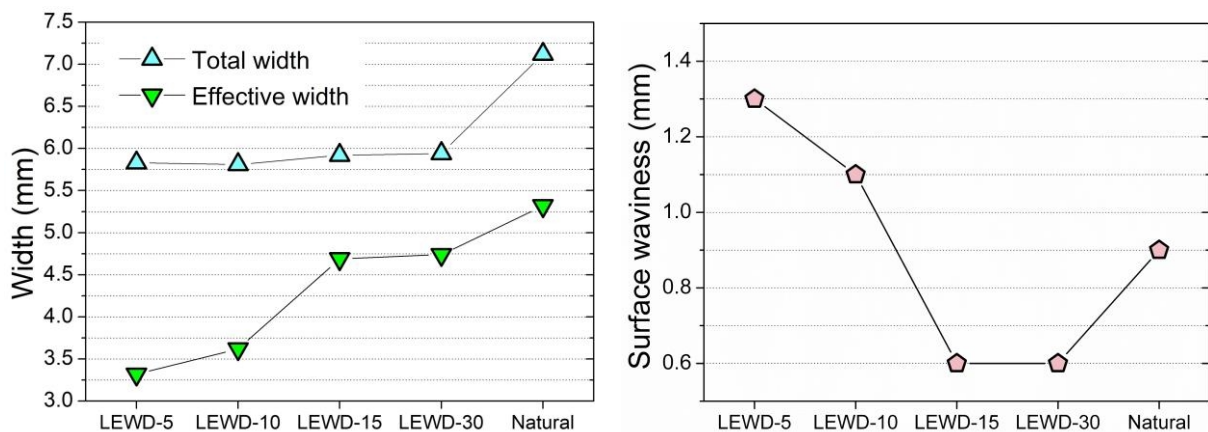

Figure 4.14. Effect of the LEWD on the width and surface waviness of the walls

In general, the porosity level was in concordance with that figures reported in the current literature (Ryan et al., 2018). As shown in Figure 4.15, the significant higher porosity level for the lowest LEWD can be attributed to a larger water evaporation, which could hydrate the fresh oxides and/or contaminate the molten pool. The replication in a certain range (Figure 4.15 right-hand side) confirms that the porosity tends to increase for lower LEWD values. There is also a tendency to increase the porosity in walls deposited under the Natural cooling approach. This behavior might be related to larger molten pool volumes this case, which could absorb higher amounts of hydrogen (Da Silva and Scotti, 2006) and/or due to heat cumulation, which may promote an intra-pore coalescence phenomenon and an expansion of trapped gas inside the pores (Gu et al., 2016; Toda et al., 2009).
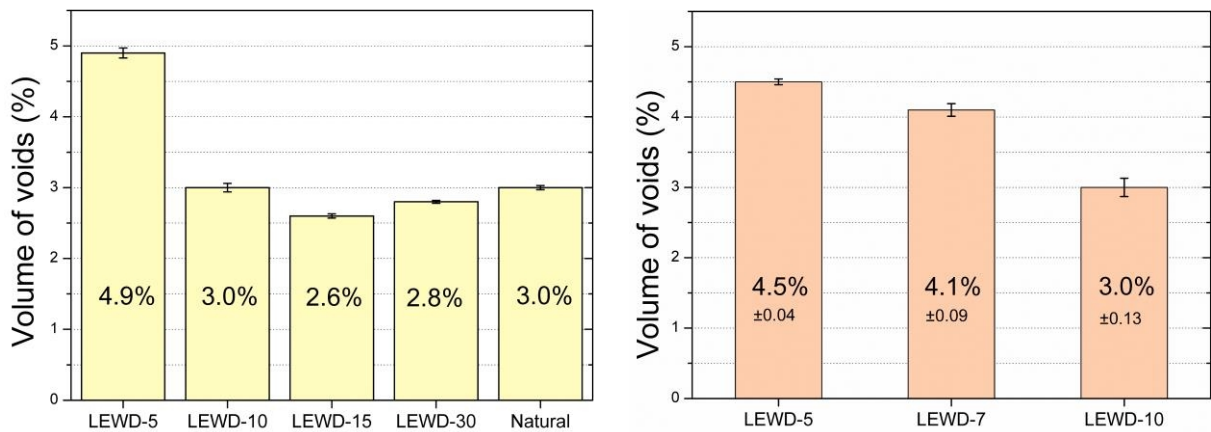
Figure 4.15. Effect of the LEWD on the volume of voids

Figure 4.16 shows the temperature measured by the trailing/leading IR pyrometer during the deposition of two layers. Because of the bidirectional deposition strategy, two levels of temperature can be distinguished. The highest level is the temperature of the newly deposited layer measured at 30 mm behind the arc center. The lowest level represents the temperature measured at 30 mm ahead of the arc. For the Natural cooling approach, both levels are higher. For the NIAC technique, the lower the LEWD the lower both the levels of temperatures due to the higher heat sinking effect. Also, it is possible to notice that there is a time for the temperature to stabilize, which depends on the thermal management technique applied. Under the NIAC technique, the lower the LEWD the faster the temperature stabilization due to the higher heat sinking effect.

As shown in Figure 4.17 (left-hand side), the temperature data acquired from the trailing/leading IR pyrometer during all the deposition time (20 layers) tends to fit a bimodal distribution. The average temperature measured ahead of the arc (forward temperature - FT) corresponds to the first quartile Q1 (25%) and seems to be representative of the average interpass temperature. The temperature measured behind the arc (backward temperature BT) corresponds to the third quartile Q3 (75%) and represents the average temperature of the ongoing layer at 30 mm behind the arc center. Hereafter, to facilitate the comparison between different groups of data in terms of their quartiles, the temperature data from the trailing/leading IR pyrometer is represented through the boxplot method, as shown in Figure 4.17 (right-hand side).
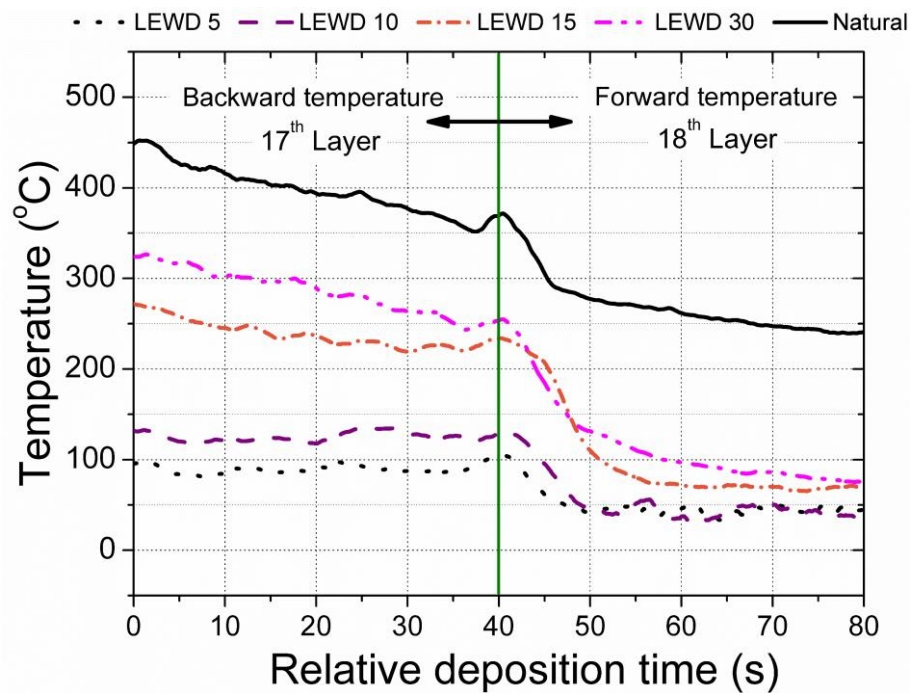
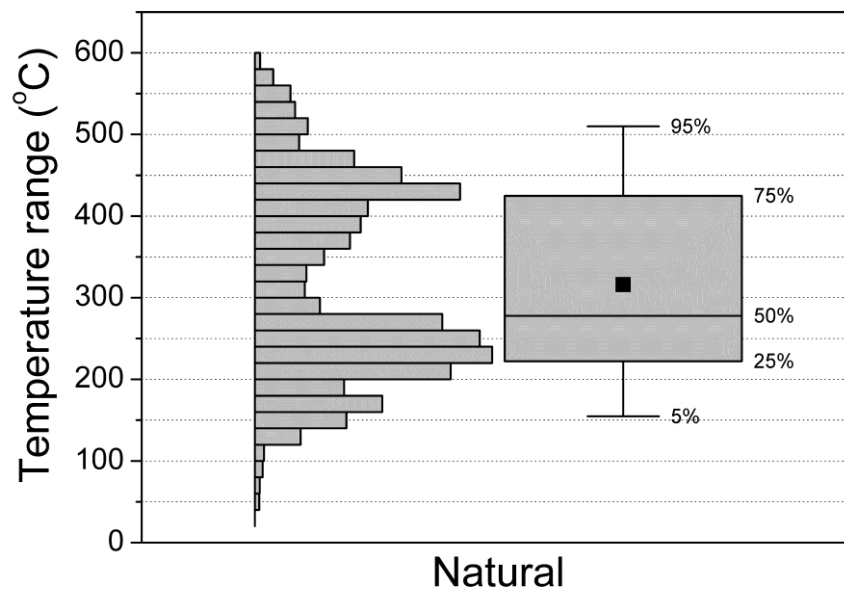Figure 4.16. Temperature data from the trailing/leading IR pyrometer (after the deposition of 2 layers)

Figure 4.17. Temperature distribution based on the data acquired from the trailing/leading IR pyrometer during all the deposition time

Figure 4.18 shows the effect of the LEWD on the temperature data distribution, while Table 4.7 lists the values of BT and FT. The FT (25%) as well as the BT (75%) temperatures tend to become lower as the LEWD is reduced. However, the BT (the

top line of the box) is more sensible to the LEWD variation than the FT (the bottom line of the box). The FT appears to be more dependent on the water temperature than on the LEWD used. Moreover, the interquartile range (Q3-Q1: the box height) is remarkably narrower with low LEWD values due to the correspondent high heat sinking powers. Therefore, for a low Q1 (interpass temperature), it sounds quite reasonable to link a low interquartile range to a high cooling rate.
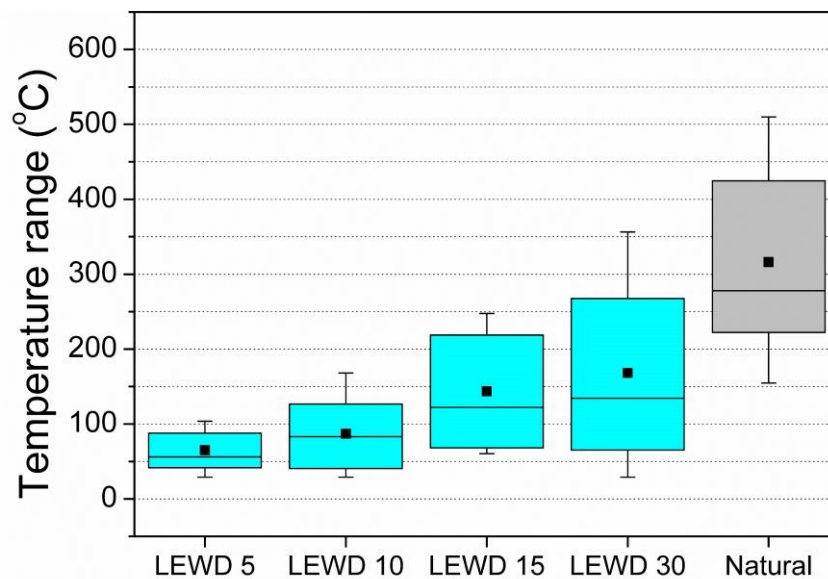

Figure 4.18. Effect of the LEWD on the thermal features measured with the trailing/leading IR pyrometer

Table 4.7. Effect of the LEWD on the average forward and backward temperatures

	LEWD: 5 mm	LEWD: 10 mm	LEWD: 15 mm	LEWD: 30 mm	Natural
Forward temperature – FT (ºC)	42	40	68	65	222
Backward temperature – BT (ºC)	88	127	219	267	425

To analyze if the FT (the bottom line of de boxplot: 25%) is representative of the interpass temperature, a wall was deposited under the Natural cooling approach using the FT as the criterion to resume the deposition of a new layer, *i.e.*, in between each layer an interpass dwell time[2] was added to allow air cooling until the wall reached that specific FT value. The cross-sectional views presented in Figure 4.19 show that the

---

[2] Dwell times, including dwells in between each individual pass and each layer can be used to control interpass temperature (ASTM, 2016)

wall deposited under the Natural cooling approach with an interpass temperature equivalent to the FT achieved with the NIAC technique with the LEWD of 15 mm is quite similar to that deposited with that condition. However, due to the dwell time demanded for cooling, the deposition time under the Natural cooling approach was significantly longer (49 minutes) than that with the NIAC technique (7 minutes). Moreover, it is also important to keep in mind that, despite being able to reach an equivalent geometry, the Natural cooling approach does not eliminate deleterious consequences of long exposures to high temperatures, *e.g.*, excessive oxidation (Wu et al.. 2018), grain growth (Wang et al.. 2016), overaging (Rometsch et al., 2014), etc.
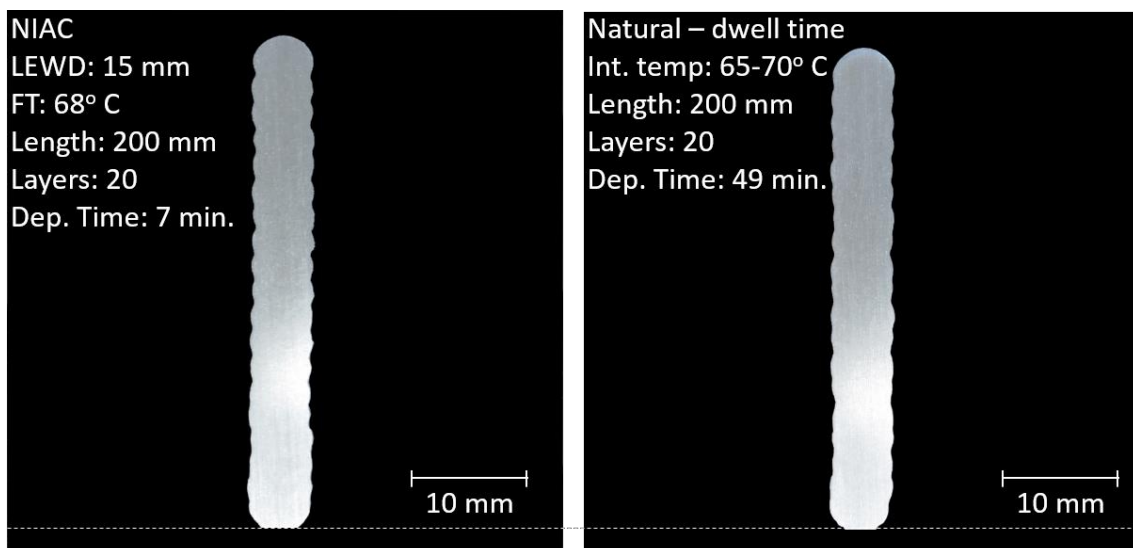

Figure 4.19. Comparison between walls deposited with the NIAC technique and with the Natural cooling approach under equivalent interpass temperatures

Among the many advantages reported in the current literature, the WAAM is referred to as being suitable for the deposition of large metallic components, typically heavier than 10 kg (Williams et al., 2016). However, large components may have a few minor localized features, which could lead to deposition concentration and, without the appropriate thermal management, to localized heat accumulation, typically as the example shown in Figure 4.20. Therefore, a set of experiments were performed to evaluate the NIAC technique performance in terms of conditions with concentration of deposition.
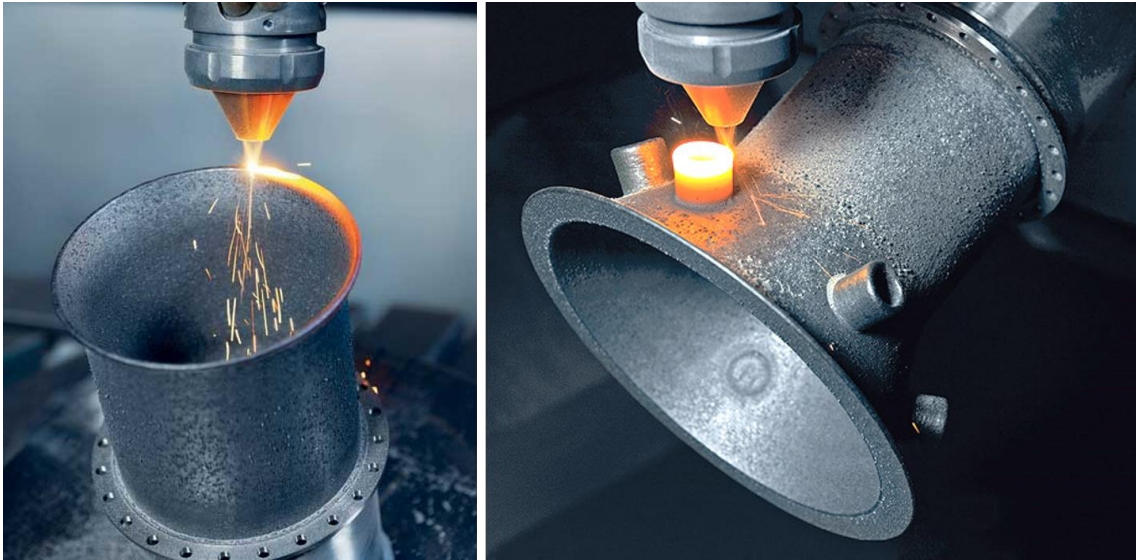
Figure 4.20. Example of deposition concentration on laser metal deposition of a stainless steel turbine housing with dimensions of 180 x 150 mm (DMG-MORI, 2019)

To simulate different levels of concentration of deposition, walls with different lengths were deposited with the NIAC and the Natural cooling approaches. The deposition parameters, the LEWD (15 mm) and the number of total number of layers (20) were kept constant. For the Natural cooling condition, it can be clearly seen in the cross-sectional views presented in Figure 4.21 that the shorter the wall length the higher the heat accumulation. The temperature data distribution showed in Figure 4.22 confirms that the more deposition concentration exists the warmer the preform. For walls shorter than 100 mm, the molten pool tends to collapse due to its very large volume. As the length of the walls is increased, they become taller and slender because of the longer deposition times and, consequently, the longer cooling times until the depositions are finished. It could be expected that above a certain length the deposition time of one layer would be long enough to suppress the heat accumulation.

In contrast, the walls deposited under the NIAC technique were quite similar compared to each other for all lengths tested. Besides geometry, the walls deposited with the NIAC technique displayed similar temperature data distribution as shown Figure 4.22, which can be translated into the ability that this thermal management approach has to keep similar cooling rates and thermal histories independently of the preform geometry.
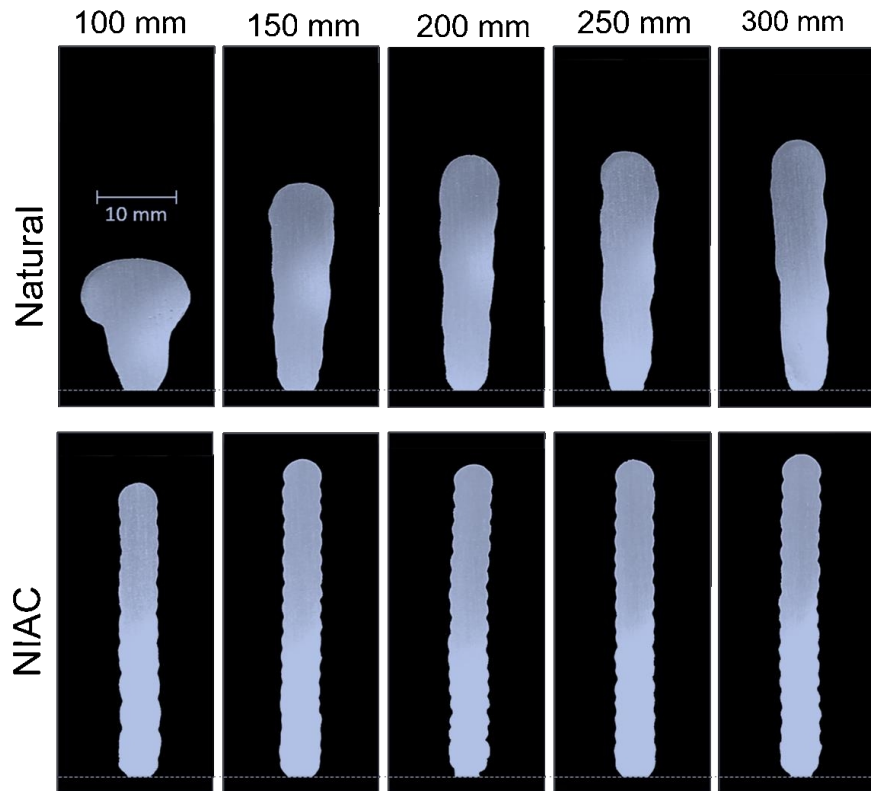
Figure 4.21. Effect of the deposition concentration (walls with different lengths) on the geometry of walls deposited with the NIAC (LEWD of 15 mm) and the Natural cooling approaches
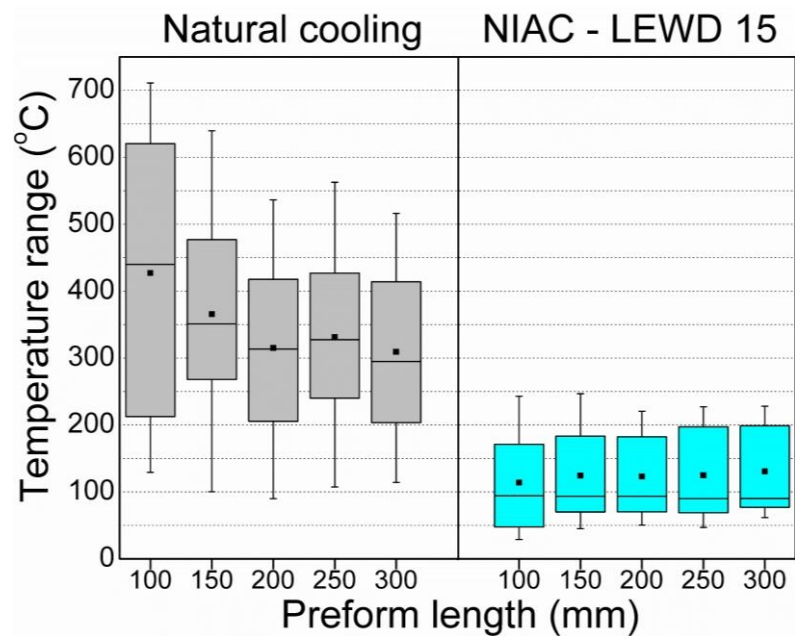

Figure 4.22. Comparison between temperature data distributions of walls built with different lengths deposited under the NIAC (LEWD of 15 mm) and the Natural cooling approaches

4.5 Partial remarks

- The water level control through the magnetic float switch was able to keep the LEWD constant during all the deposition times;
- The variation of the LEWD had no significant effect on the total width (external width), while the effective width increased with an increasing LEWD;
- The surface waviness was higher for lower LEWD values;
- In general, the porosity level was in concordance with the numbers reported in the current literature. However, it tends to significantly increase with LEWD values lower than 10 mm;
- In terms of geometry and porosity, the walls deposited under the NIAC technique with LEWD values between 15 and 20 mm showed better results, so that this range will be used for the next steps of this thesis;
- The temperature data from the trailing/leading IR pyrometer extracted during all the deposition time tends to fit a bimodal distribution and the first quartile (Q1) is representative of the interpass temperature;
- Walls deposited with the NIAC and the Natural cooling approaches can assume quite similar geometries if they are built with equivalent interpass temperatures. However, the deposition time with the latter approach is significant longer due to demanded interpass dwell time; and
- The NIAC technique has been proved as able to cope with the heat accumulation due to deposition concentration. Moreover, it showed to be capable of aiding the continuous building of small components and/or features by WAAM.

4.5 Difficulties observed

- The use of WAAM with the NIAC technique is limited to a flat position, although angled walls are also allowed within some limits (overhang angle). Therefore, especially in multi-axis manufacturing systems with a moving worktable, other cooling strategies should be applied;
- Although the magnetic float switch fulfills the goal of controlling the water level, for more complex preform geometries it could shock to the preform. Therefore,

another water level sensor should be used in an industrial application, for example, a capacitive kind;

- It is still not possible to control the water temperature for aiming at a more effective thermal management; and
- The temperature measurement of the preform as proposed is limited to simple geometries since the pyrometer might miss the preform itself in more complex geometries.

CHAPTER V - PARAMETER SELECTION PROCEDURE FOR WAAM WITH THE NIAC

5.1 Contextualization

The success and efficiency of WAAM of a component strongly depends on the accurate selection of the deposition parameters need for a target geometry. Differently from the PBF techniques, whose transition from a 3D model data to a machine code can be considered automatic, WAAM still requires a labor-intensive process for parameter investigation and selection. Although numerical models are becoming increasingly accurate across a wide spectrum, especially in terms of thermomechanical-related features, they still require expensive hardware, highly-skilled labor and are often slow. In this sense, empirical models have proven to be a useful tool as per Almeida and Williams (2010), for WAAM of Ti6Al4V with the CMT process, and Martina et al., (2012), for WAAM of Ti6Al4V with the PA and GTA processes. This chapter assesses hardware capabilities, develops an operational envelope, and proposes a parameter selection procedure for the making of Al preforms via WAAM with the NIAC technique.

5.2 Experimental procedures

The experimental set-up was the same as that described in Chapter 4. The deposition conditions are summarized in Table 5.1. The experimental trials were carried out on a vertically clamped substrate to mimic a wall-like preform in terms of heat flux and stiffness. To mitigate the effects of the external sources of hydrogen and, consequently, the porosity, the substrate was lightly sanded just before deposition and the wire surface was continuously cleaned by a felt clamped to the wire just before the feeder rolls, as shown in Figure 5.1.

Table 5.1. Deposition conditions for the parameter selection procedure

| Arc deposition equipment	Fronius CMT - TransPuls Synergic 500
Wire (deposition material)	AWS ER 5356 - Ø 1.0 mm
Substrate	Al5052 (220 x 38.1 x 6.4 mm)
CTWD*	12 mm
Shielding gas	Commercial argon - 15 L/min
Cooling liquid	Tap water at around 20 ºC
Work tank volume	50 L
Preform geometry	Single wall with 12 layers and length of 200 mm
Building strategy	Single-pass multi-layers bidirectional depositions
Dwell time	10 s/layer

*CTWD: contact tip to work distance
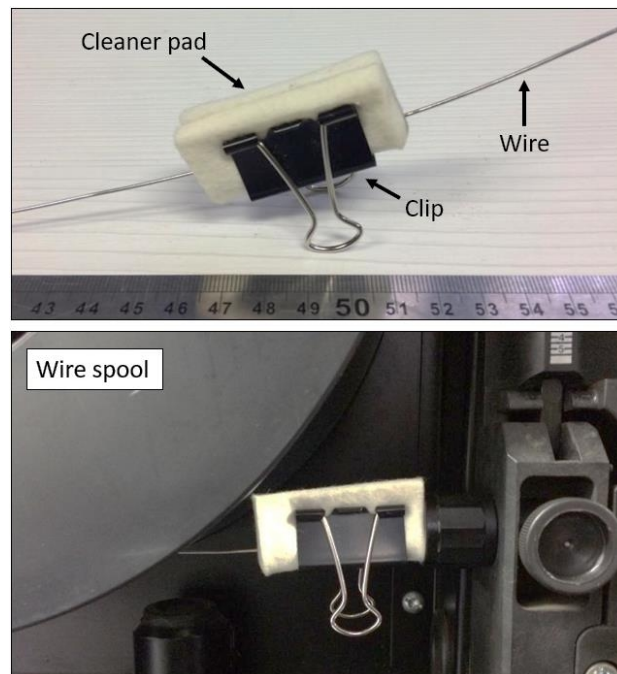
Figure 5.1. Wire cleaner felt used to mitigate the effect of external impurities

5.2.1 Measurements

The following responses were measured:

- Deposition parameter: voltage (U), current (I) and WFS;
- Relative density by the Archimedes method;
- Total Wall Width – TWW (Martina et al., 2012);
- Effective Wall Width – EWW (Martina et al., 2012);
- Surface Waviness – SW (Martina et al., 2012); and
- Layer Height – LH (Martina et al., 2012).

The actual deposition parameters were measured with the DAQ system described in Chapter 4. For the measurement of the voltage, the probes were attached to both the contact tip and plate support to eliminate the inductive effect of the power source cables. The current was measured by a hall-effect transducer. The wire feed speed measurements were performed by an optical encoder-based system clamped to wire just before the feeder rolls. As a rule of thumb, the DAQ system was warmed up for 30 minutes at the start of each day of tests.

The average instantaneous power method (Jorge et al., 2017) was employed to calculate the arc energy per unit length of deposit as given by Eq. (5.1).

$$Arc\ enery = \frac{P_{i\,nst}}{TS} = \frac{\frac{1}{n}\sum_{k=1}^{n} U_k * I_k}{TS} \qquad (5.1)$$

where:

- Arc energy: arc energy per unit length of deposit (J/mm);
- P_{inst}: average instantaneous arc power (W);
- TS: travel speed (mm/s);
- U: voltage (V); and
- I: current (A).

The porosity was indirectly assessed through the relative density using the Archimedes principle. The wire density was estimated by the same method and used as the reference. Considering Martina et al. (2012) definitions illustrated in Figure 5.2, the TWW, EWW and SW were measured from cross-section macrographs by using an image analyses algorithm developed in MatLab®. It is worth mentioning that although there are others standardized parameters to characterize surface textures, *e.g.* ANSI/ASME B46.1, the Martina et al. (2012) definition became common in the WAAM literature, so it was chosen to be used to enable a comparison with the literature results.
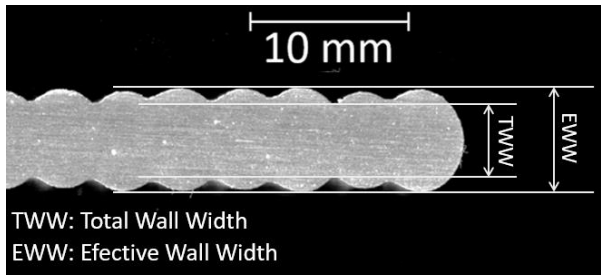
Figure 5.2. Definition of geometrical features according to Martina (2012) (by the author)

$$SW = \frac{TWW - EWW}{2} \qquad (5.2)$$

During the building process, the heights of the preforms from the substrate at the 4th (PH$_{L4}$) and 12th (PH$_{L12}$) layers were measured with a Vernier caliper at the 50, 100 and 150 mm horizontal lengths. These data were used to estimate the average LH as following:

$$LH = \frac{PH_{L12} - PH_{L4}}{8} \qquad (5.3)$$

This value was used to determine the height increment for deposition of the following layers. The first 4 layers were disregarded to ensure that the process had already reached a steady-state regime.

5.3 Operational map and working envelope

Initially it is important to distinguish an operational map from a working envelope. In the present thesis, the operational map is a wider view of the hardware capability/limitations. While the working envelope is an area inside the operational map, where parameters result in preforms that meet some acceptance criteria.

5.3.1 Definition of the operational map boundaries: hardware capabilities

Preliminary depositions were carried out to determine the operational map boundaries, *i.e.*, the constraints on the deposition parameters that separate the feasible from the unfeasible combinations. According to Almeida and Williams (2010), as well as, from the know-how gained up to this point, the TS and WFS are the

variables with higher effect on preform geometry. Although there are many other secondary variables, TS and WFS were select to reduce the number of independent variables investigated and therefore the complexity of this preliminary experiment. The LEWD value was kept constant in 20 mm.

For a given WFS, the TS was increased and decreased from an average value (10 mm/s) in steps of 1.67 mm/s up to reach the wall quality limits, which were visually assessed. The interpass temperature was kept below 50 °C and the contact tip to work distance (CTWD) was adjusted for each layer. This approach was inspired by Yehorov et al. (2019), but, while they increased the TS during the ongoing deposition, in this thesis the TS was variated for each layer.

The operational map is graphically presented in Figure 5.3. The WFS and TS upper limits are due to the hardware limitations, while the lower limits are due to the tendency of lack of fusion, poor wettability between layers and low production. For relatively low WFS and high TS values, the layer tends to become undulated (with humping), corroborating what is reported in the welding literature. In contrast, for high WFS and low TS values the molten pool grows and tends to collapse due to its large volume.
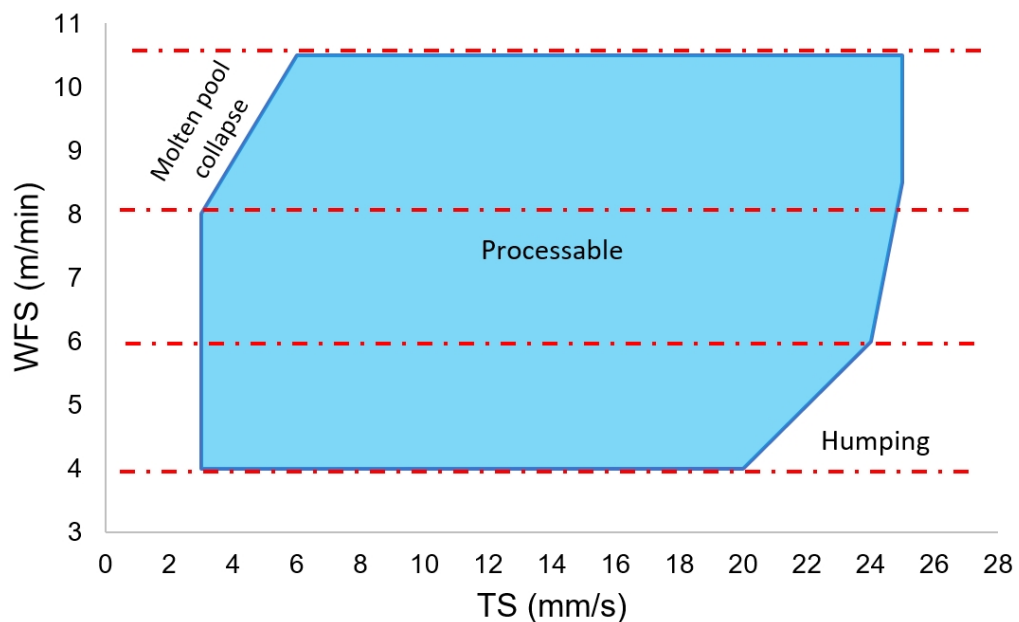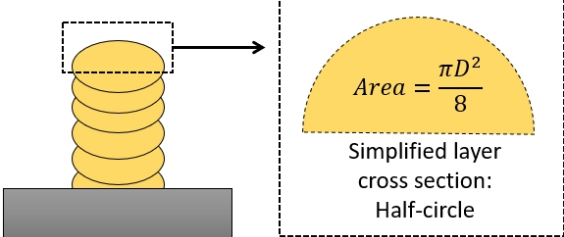

Figure 5.3. Operational map

5.3.2 The working envelope: first approximation (analytical model)

As a first approximation for the development of the working envelope, the layer geometry was considered as a semi-cylinder, where its diameter and radius represents the layer width and height, respectively, as illustrated in Figure 5.4. In fact, Ríos et al. (2018) showed that the layer geometry tend to fit a semi-cylindrical geometry due to surface tension effects.

By considering a feasible wall width range as between 4 and 7 mm, which is in concordance with the literature (C. Zhang et al., 2018), the WFS, TS and layer height were predicted through a geometrical correlation, as presented in Figure 5.4 – Eq. (5.4). A similar correlation is often used in welding technology to estimate the number of passes to fulfill a groove for a given WFS and TS.

$$\frac{\pi * \text{TWW}^2}{8} = \frac{\text{WFS}}{\text{TS}} * \text{Wire}_{\text{area}} \qquad (5.4)$$

Figure 5.4. First approximation of the cross-sectional layer geometry and its correlation with the deposition parameters (by the author)

where:

- TWW: total wall width;
- WFS: wire feed speed;
- TS: travel speed;
- WFS/TS: wire deposition per unit length of deposit; and
- Wire$_{\text{area}}$: wire cross section area.

Figure 5.5 shows the predicted working envelope, which was built considering a wall width variation in steps of 1 mm. It can be noticed that the estimated WFS and TS values fall into a processable area of the operational map (Figure 5.3). In this parametric chart, the WFS and TS parameters can be selected for a target wall width (y-axis). Moreover, through the WTS/TS ratio (horizontal lines), values for the WFS

and TS could be selected to achieve more productivity. However, some divergences are expected in the practical scenario due to the plasma jet pressure over the molten pool and as well as to effects caused by the interaction of the Earth's gravity, the molten pool volume and its surface tension, which were not considered in this simplified model.
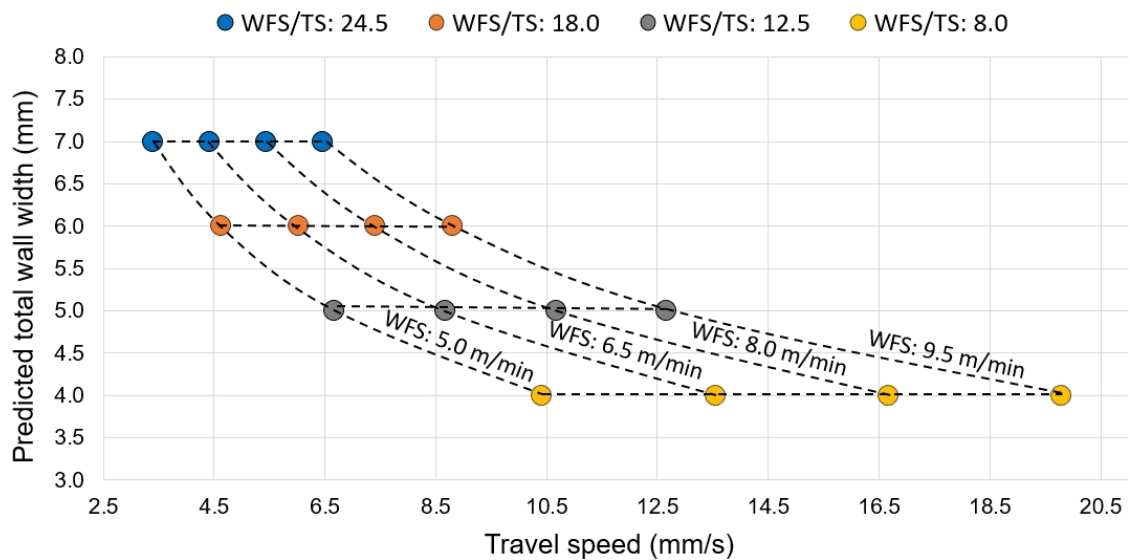

Figure 5.5. Predicted working envelop (by the author)

5.3.3 The working envelope: matrix of experiments

Table 5.2 shows the matrix of experiments used in the experimental approach of the working envelope. This matrix was based on the proposed analytical model (Figure 5.4) and corresponds to the same data used to build the predicted working envelope from Figure 5.5.

Table 5.2. Matrix of experiments to build the experimentally-based working envelop

Run	Predicted TWW [mm]	Predicted LH [mm]	WFS [m/min]	TS [mm/s]	WFS/TS* [1]
1	7.0	3.5	5.0	3.4	24.5
2	6.0	3.0	5.0	4.6	18.0
3	5.0	2.5	5.0	6.7	12.5
4	4.0	2.0	5.0	10.4	8.0
5	7.0	3.5	6.5	4.4	24.5
6	6.0	3.0	6.5	6.0	18.0
7	5.0	2.5	6.5	8.7	12.5
8	4.0	2.0	6.5	13.6	8.0
9	7.0	3.5	8.0	5.5	24.5

10	6.0	3.0	8.0	7.4	18.0
11	5.0	2.5	8.0	10.7	12.5
12	4.0	2.0	8.0	16.7	8.0
13	7.0	3.5	9.5	6.5	24.5
14	6.0	3.0	9.5	8.8	18.0
15	5.0	2.5	9.5	12.7	12.5
16	4.0	2.0	9.5	19.8	8.0

* The WTS/TS ratio is dimensionless and hence to calculate it the WFS and TS values must be in the same unit

5.3.4 The working envelope: acceptance criteria

As aforementioned, the working envelope is an area inside of the operational map (Figure 5.3) where the preforms reach one or more acceptance criteria. As no specific standards for WAAM of aluminum were found, some acceptance criteria were established based on welding standards (*i.e.* AWS D1.2 Structural Welding Code – Aluminum) and on the literature, as presented in Table 5.3.

Table 5.3. Acceptance criteria used to build the working envelope

Feature	Method of inspection	Acceptance criteria
Surface aspect	Visual	The surface of the layer shall be smooth, shiny and sufficiently free from coarse undulations, grooves, overlaps, abrupt ridges, and valleys.
Surface waviness	Cross section analyses	The surface waviness shall be lower than 0.5 mm (Williams et al., 2016).
Relative density	Archimedes principle	The preform relative density shall be higher than 97% (Da Silva and Scotti, 2006).

5.3.4 The working envelope: experimental results

Two very important factors to describe the thermal and geometric features in welding and WAAM are the arc energy per unit length of deposit (hereinafter referred to as arc energy) and the wire deposition per unit length of deposit (hereinafter referred to as WFS/TS). For non-consumable arc processes, like the PA and the GTA ones, these factors are independent, *i.e.*, they can be separately adjusted. However, this is not the case for a consumable electrode arc process, like the GMA one. In the CMT process (a variant of the GMA process), where the arc length is maintained very short, the WFS/TS ratio may be proportional to the arc energy for a given WFS range. Aiming

at a validation of this assumption, the WFS/TS ratio was plotted against the arc energy, as shown in Figure 5.6. The relationship between the arc energy and the WFS/TS ratio can be quite fitted to a linear behavior, so that it can be concluded that within the range of the WFS used, the arc energy is directly proportional to the WFS/TS ratio. In practice, this supports the statement that the higher the WFS/TS ratio the higher the arc energy per unit length of deposit.
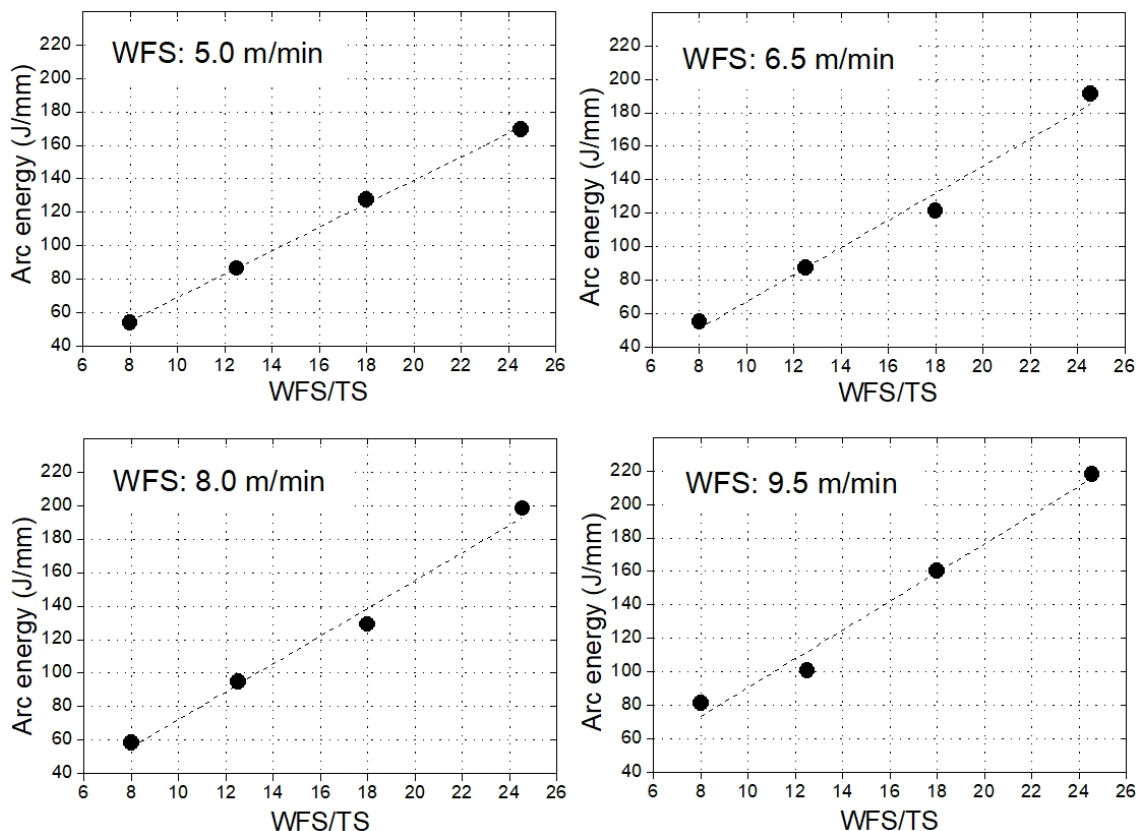

Figure 5.6. Correlation between the WFS/TS ratio and the arc energy per unit length of deposit for the CMT process

The preforms deposited with the WFS of 8.0 and 9.5 m/min did not reach the acceptance criteria of surface aspect. For these conditions, the preform surface was always rough and matte due to excessive oxidation, as shown in Figure 5.7. This behavior could be related to a poor shielding action. In fact, the nozzle that was used is designed for welding, where the shielding gas flux hits the plate in a large area (equivalent to the gas nozzle) and spreads. However, for WAAM of thin walls (usually narrower than the gas nozzle) most of the shielding gas flux tends to pass straight laterally along the wall sides, losing part of its shielding capability.
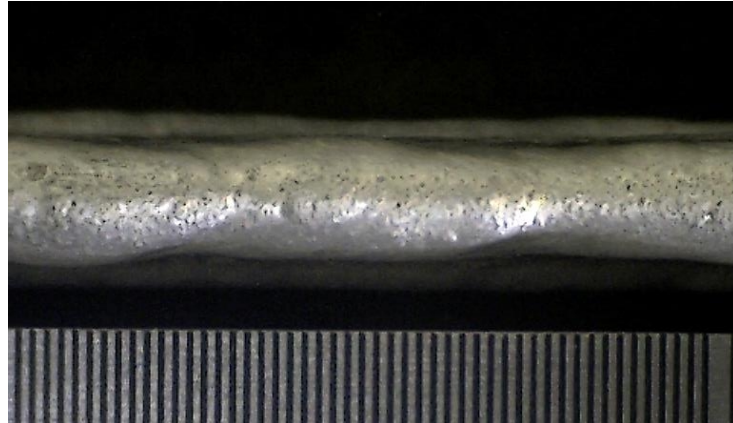
Figure 5.7. Surface aspect of run 12 of Table 5.4 (WFS of 8 m/min), which did not meet the acceptance criteria

In terms of relative density, all preforms reached an acceptable level, as shown in Figure 5.8. Interestedly, this set of experiments showed higher relative density than those from Chapter 4, fact that could be related to the cleaning of the wire surface. Figure 5.9 evidences the impurities removed from wire surface by the cleaner felt. However, more detailed investigations are needed to assess the effectiveness of it on porosity, but this is out of the scope of this thesis.
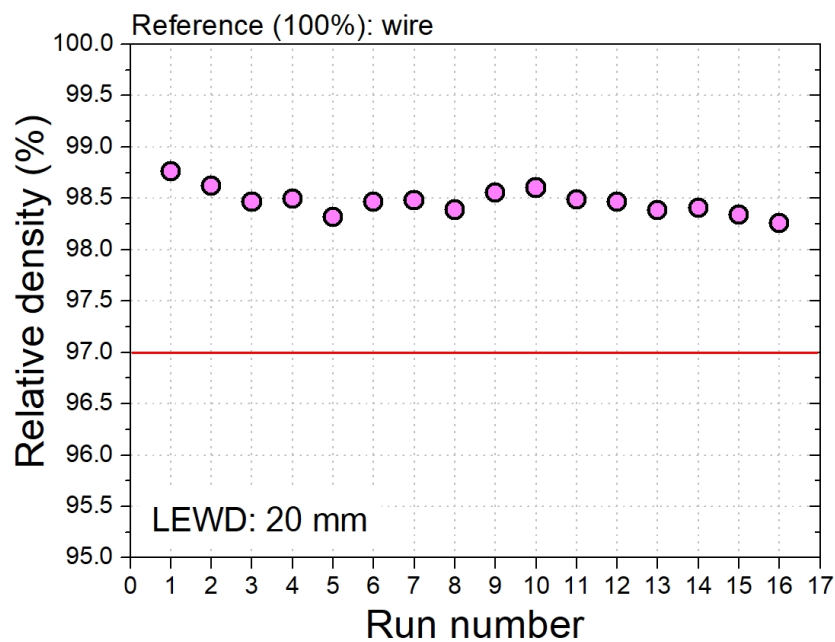

Figure 5.8. Relative density of the preforms produced according to Table 5.5 (acceptance criteria: above the red line)
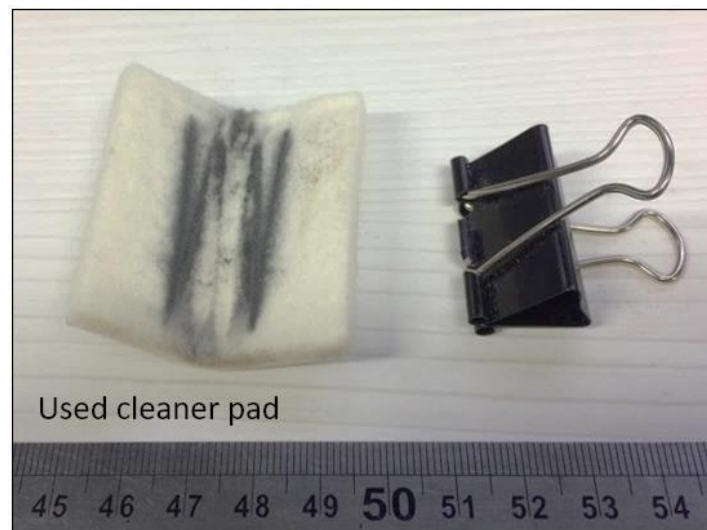
Figure 5.9. Wire cleaner felt after performing 16 depositions (Table 5.6)

An atlas of the cross-sections of the preforms produced is presented in Figure 5.10. In this atlas, the WFS is separated in the lines while the WFS/TS ratio appears in the columns. For all the conditions the wall width remained nearly constant along the height, which suggests that there was no significant heat accumulation and that all deposition conditions were kept constant along the layers manufactured. These cross-sections macrographs were used to determine the TWW, EWW and SW levels through an image analysis algorithm developed in MatLab®.

In general, the SW numbers were higher for lower WFS values and the preforms deposited with the WFS of 5.0 m/min did not reached the acceptance criteria, as shown in Figure 5.11. It is interesting to notice in Figure 5.11 that for all conditions the SW evolution tend to fit a parabolic pattern with minimum values around the WFS/TS of 12.5 (arc energy per unit length of deposit: 90-100 J/mm). This behavior may be related to the amount of remelting of the previous layer. Just like for a welding penetration, there may be a competition between the effects caused by the WFS/TS ratio and the arc energy per unit length of deposit as the following possibilities:

1. Due to higher a WFS/TS, *i.e.*, a higher wire deposition per unit length of deposit, the liquid volume interposed between the arc root and the previous layer is large, so that the heat inputted by the arc needs to pass through this liquid barrier to reach the solid previous layer and melt it more effectively; and

2. Due to lower a WFS/TS, *i.e.*, a lower arc energy per unit length of deposit, there is insufficient remelting of the previous layer.
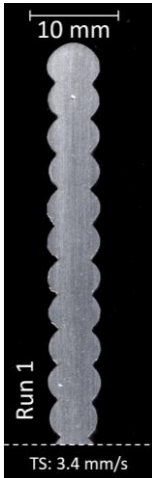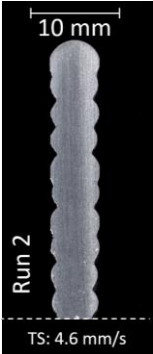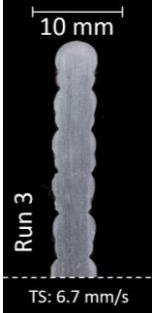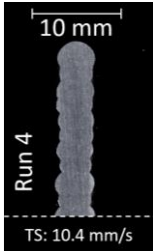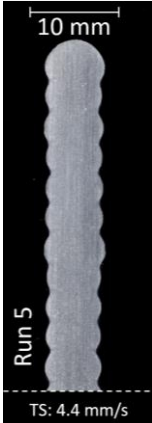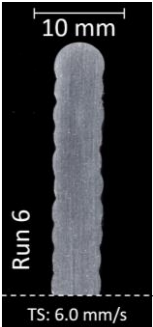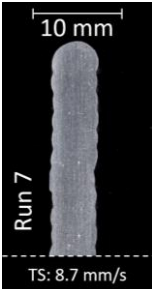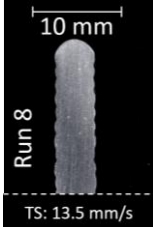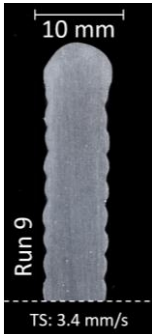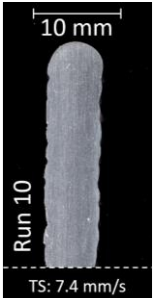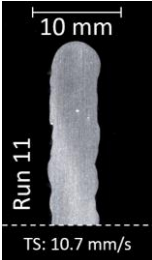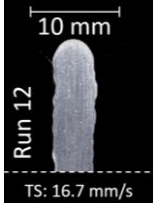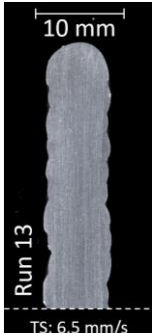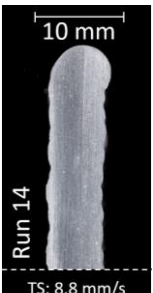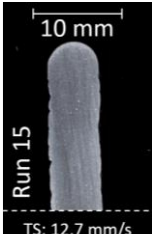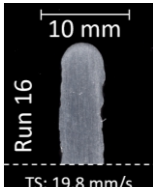
Figure 5.10. Atlas of the cross-sections of the preforms in terms of WFS values and WFS/TS ratios
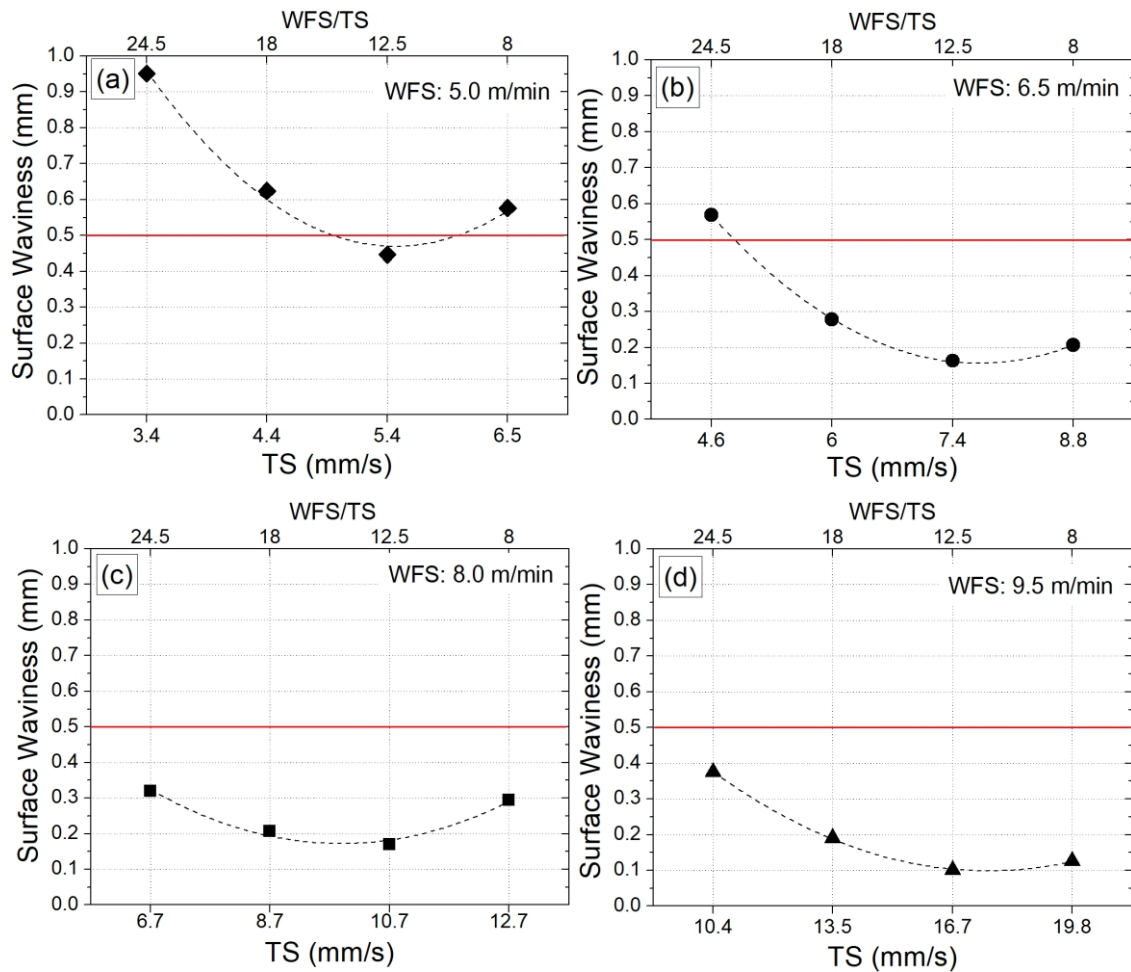
Figure 5.11. Surface waviness (acceptance criteria: below the red line)

5.3.5 The working envelope: troubleshooting

Up to this point, the working envelope resultant from the experimental approach applied is quite limited, i.e., only 3 out of 16 runs met all the acceptance criteria (Table 5.3), as indicated in Figure 5.12. It is interesting to notice in this parametric chart that the keeping of a similar WFS/TS/arc energy ratio is no guarantee of satisfactory preforms.

The main limitations seen in the operational map were the excessive oxidation of the layer top surface deposited with higher WFS values and the excessive SW of the preform lateral surface deposited with lower WFS values. Aiming at the expansion of the working envelope a few actions were taken to deal with these setbacks.
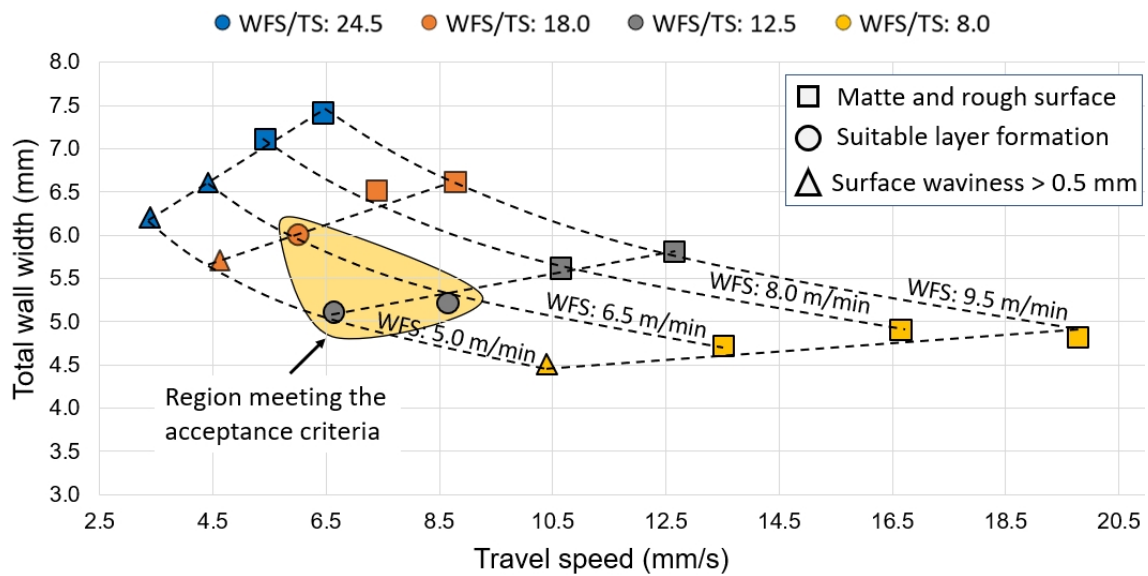
Figure 5.12. Experimentally-based working envelope: initial results

To deal with the excessive oxidation, a supplementary shielding gas system was developed, as shown in Figure 5.13. This aluminum-body device is filled with titanium chips, which act as a gas diffuser as well as an active filter for the shielding gas due to its high affinity with oxygen. A Ni-alloy honeycomb was placed at the exit of the device to laminarize the gas flow as it goes out. Through simple smoke tests, it was verified that a laminar gas flow is indeed achieved for a gas flow rate between 3-5 L/min.
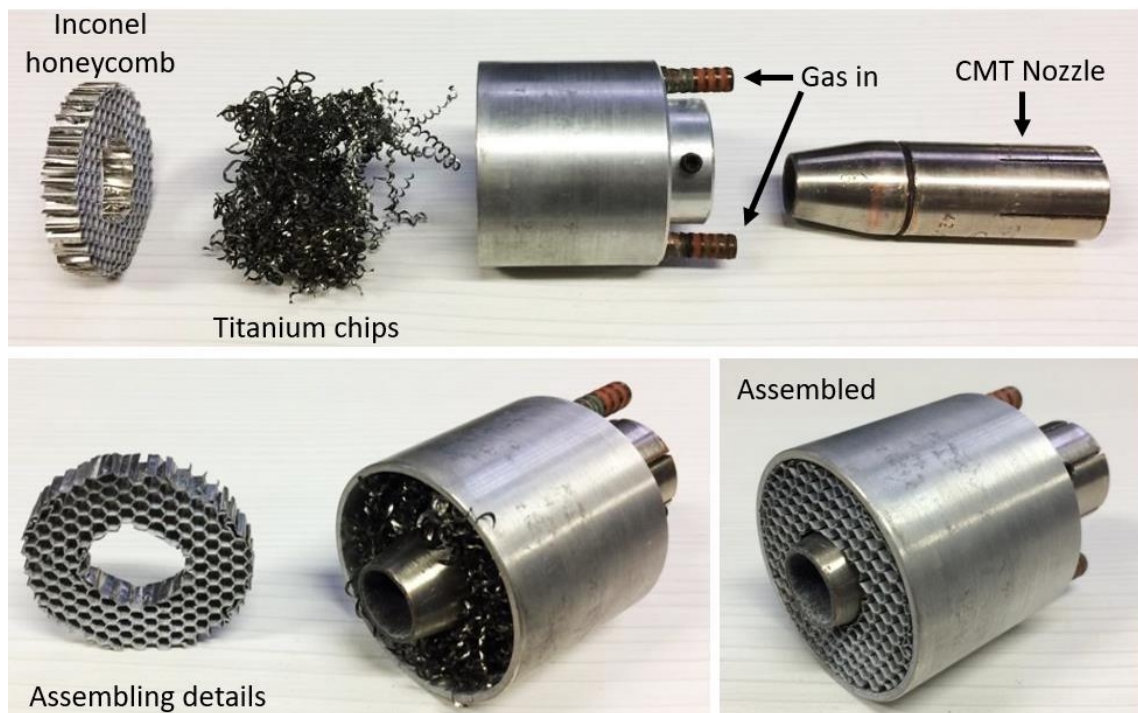
Figure 5.13. Supplementary shielding gas system developed

The effectiveness of the supplementary shielding gas device is highlighted in Figure 5.14. It can be clearly seen that the preforms deposited using this device were free of excessive oxidation, smoother and brighter. Therefore, one can say that de excessive oxidation issue was troubleshooted.

Without supplementary gas shielding

| Run 11 | Run 12 | Run 13 | Run 14 | Run 15 | Run 16 |

With supplementary gas shielding

| Run 11 | Run 12 | Run 13 | Run 14 | Run 15 | Run 16 |
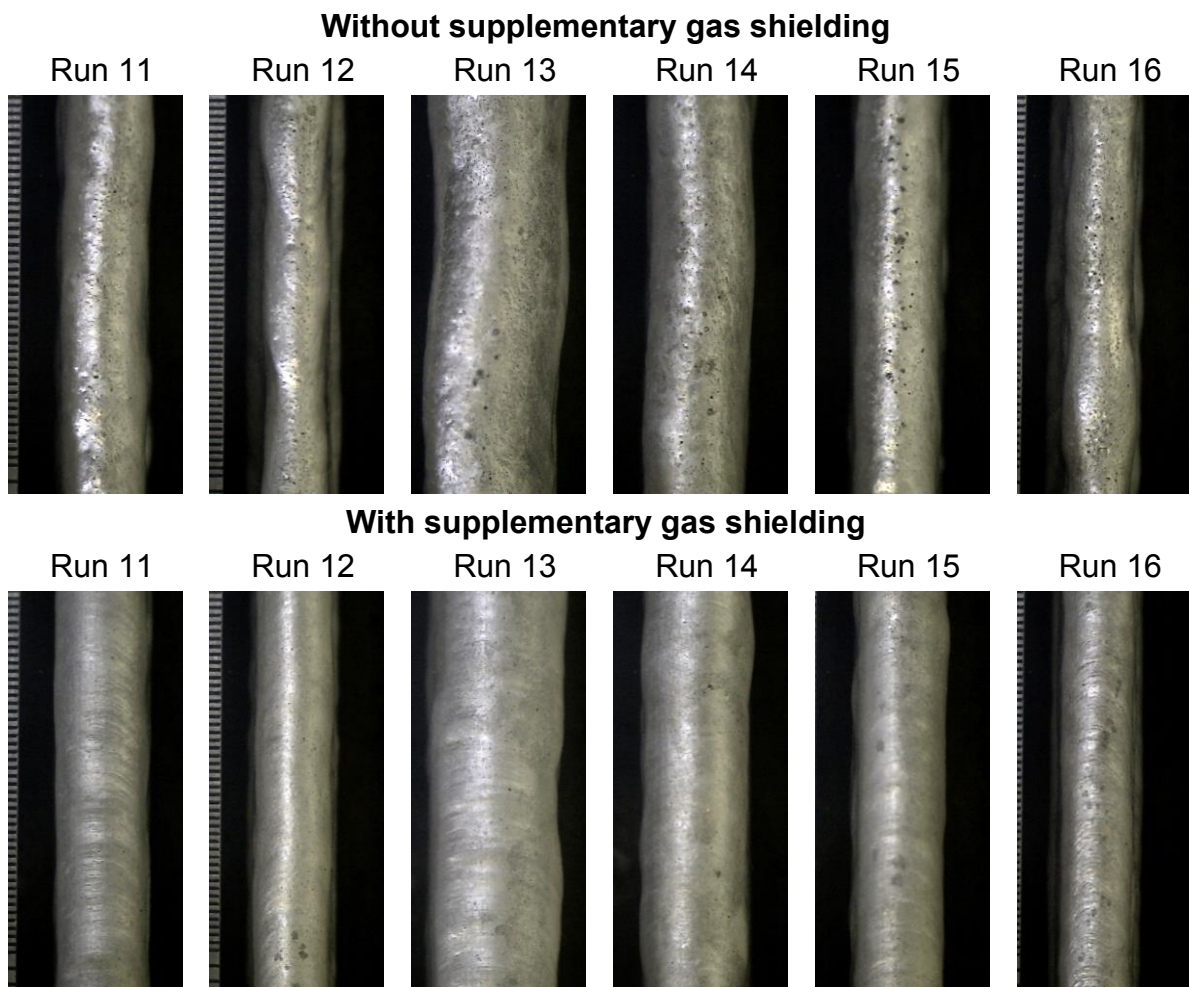
Figure 5.14. Effectiveness of the supplementary shielding gas device

As stated previously, the higher surface waviness for the preforms deposited with the WFS of 5 m/min may be related to the low remelting of the previous layer. Aiming at a validation of this statement, the deposition conditions used for the WFS of 5 m/min were repeated with a LEWD of 30 mm. The idea was to reduce the NIAC´s heat sink effect to promote a higher remelting of the previous layer.

As expected, no significant changes on the relative density were observed due to the LEWD increase from 20 to 30 mm, as shown Figure 5.15. In terms of geometry, the TWW level remained quite similar, but the preform deposited with the LEWD of 30

mm was more regular than those ones accomplished with the LEWD of 20 mm, as it can be seen in the comparison of cross-sections presented in Figure 5.16. The effectiveness of the proposed approach to improve the SW is highlighted in Figure 5.17, where it is clearly seen a lower surface waviness for the preforms deposited with the LEWD of 30 mm, being run 1 an exception. It is believed that further improvement of this condition could be achieved by using a LEWD even larger than 30 mm.
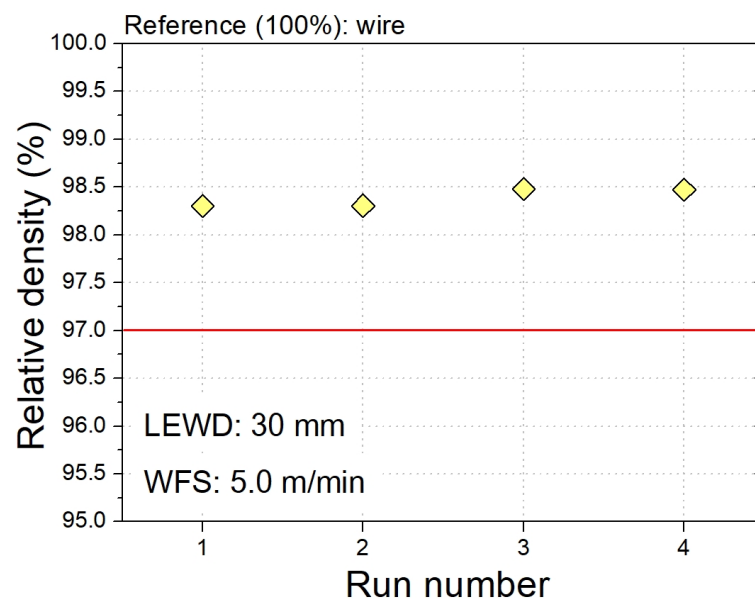
Figure 5.15. Relative density of the preforms deposited with the WFS of 5.0 m/min and with the LEWD of 30 mm (acceptance criteria: above the red line)

	WFS: 5.0 m/min			
	WFS/TS: 24.5	WFS/TS: 18.0	WFS/TS: 12.5	WFS/TS: 8
LEWD: 20 mm	10 mm Run 1 TS: 3.4 mm/s	10 mm Run 2 TS: 4.6 mm/s	10 mm Run 3 TS: 6.7 mm/s	10 mm Run 4 TS: 10.4 mm/s
LEWD: 30 mm	10 mm Run 1.1 TS: 3.4 mm/s	10 mm Run 2.1 TS: 4.6 mm/s	10 mm Run 3.1 TS: 6.7 mm/s	10 mm Run 4.1 TS: 10.4 mm/s
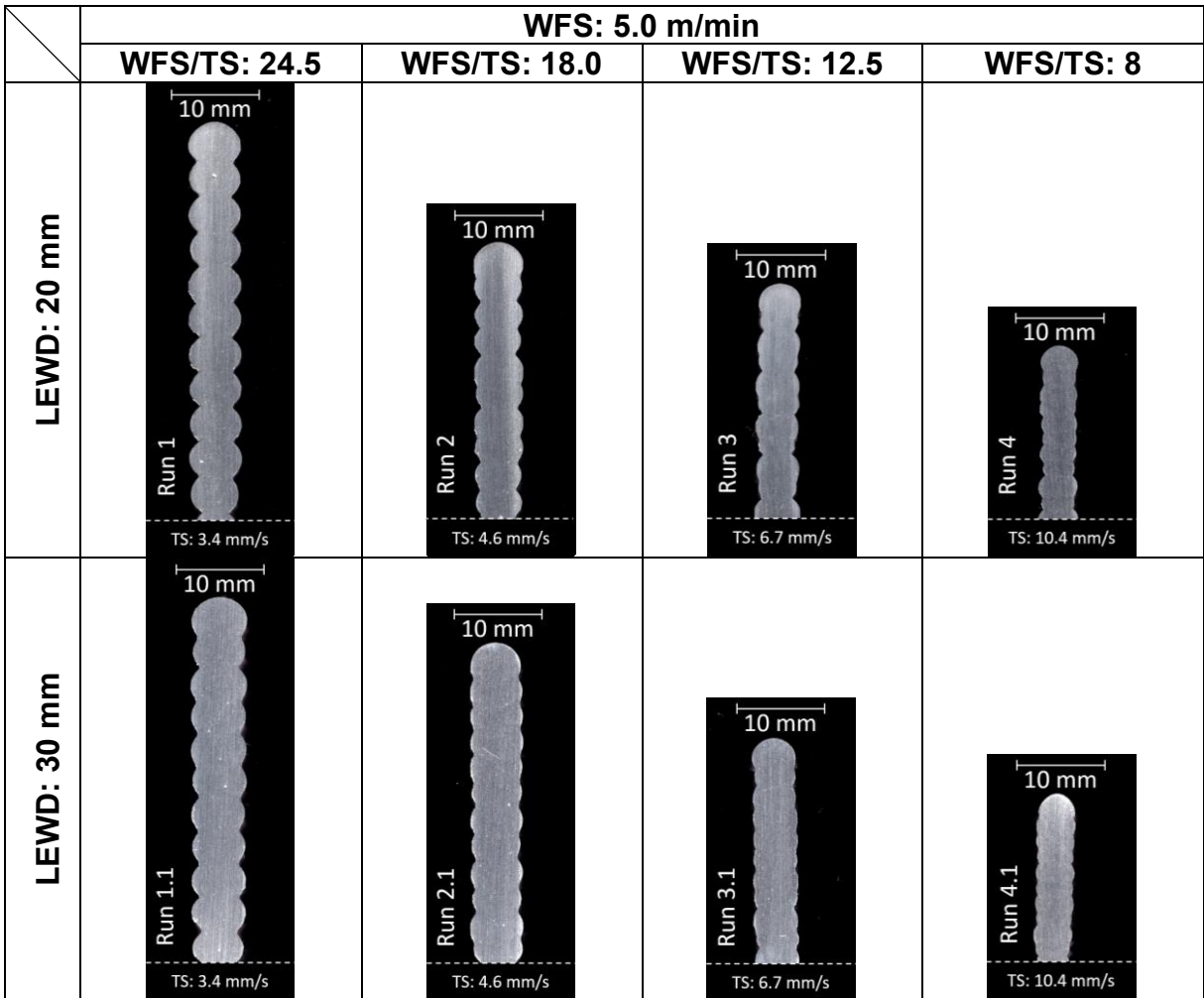
Figure 5.16. Preforms deposited with the WFS of 5 m/min: a comparison of cross-sections for the LEWD set in 20 and in 30 mm
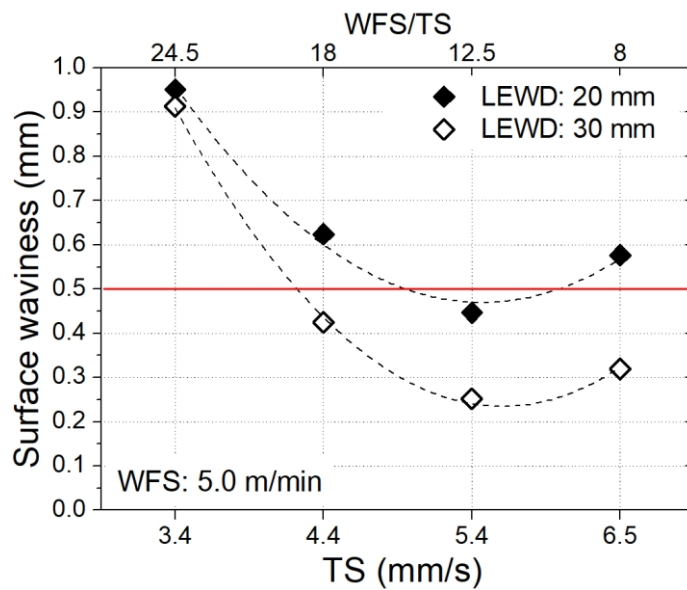
Figure 5.17. Preforms deposited with WFS of 5 m/min: a comparison of SW for the LEWD set in 20 and in 30 mm (acceptance criteria: below the red line)

5.3.6 The working envelope: the final version

After troubleshooting the excessive oxidation and the high SW for low WFS conditions, the experimental-based working envelop was updated, as shown in Figure 5.18. The working envelope area that met the acceptance criteria was significantly expanded compared to the initial one (Figure 5.12). Besides the WFS and TS parameters, this updated parametric chart now considers the LEWD level and the mandatory use of the supplementary shielding gas device for all the conditions.

Concerning geometry, it can be said that the trends predicted by the analytical model find experimental support, so that it can be used as a first approximation for parameter selection. Compared with the predicted working envelope (Figure 5.5), the main difference on the experimental results is the increasing of the TWW when increasing the WFS and TS even if keeping the WTS/TS ratio constant. This behavior may be related to the increase of the plasma jet pressure over the molten pool due to the increase of the WFS and, consequently, of the electrical current.
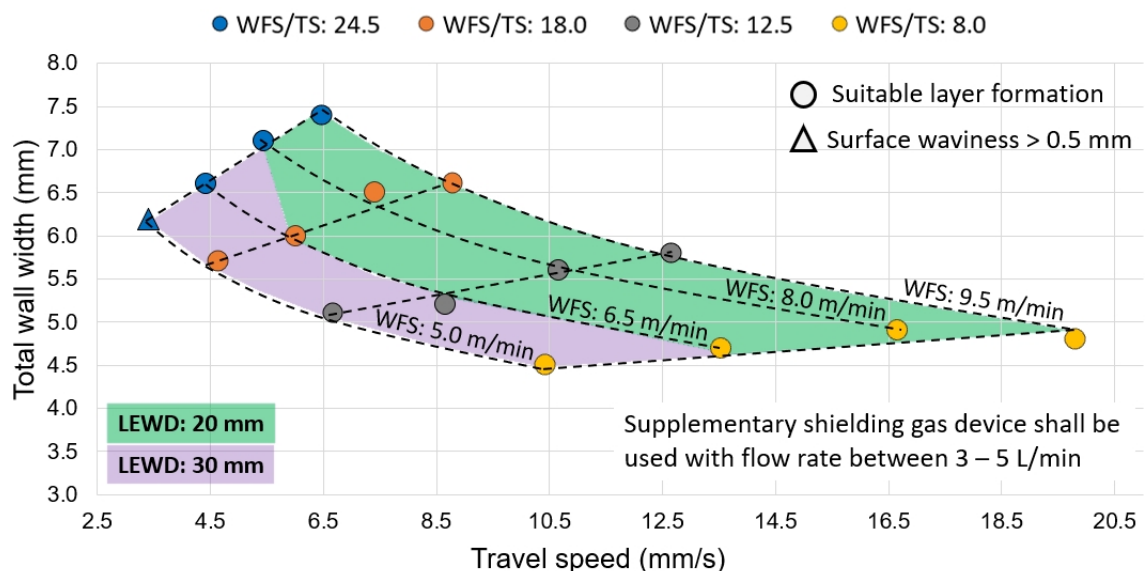
Figure 5.18. Experimentally based working envelope after troubleshooting excessive oxidation and SW issues

Different from PBF processes, where the LH is a settable variable within some limits, in the DED processes the LH depends on the deposition parameters. For WAAM, if the programed height increment between layers does not correspond to the actual individual layer height, it could lead to CTWD variations and, consequently,

affects deposition. Given the importance of the LH outcome, Figure 5.19 compiles the layer height results that correspond to the working envelope (Figure 5.18).
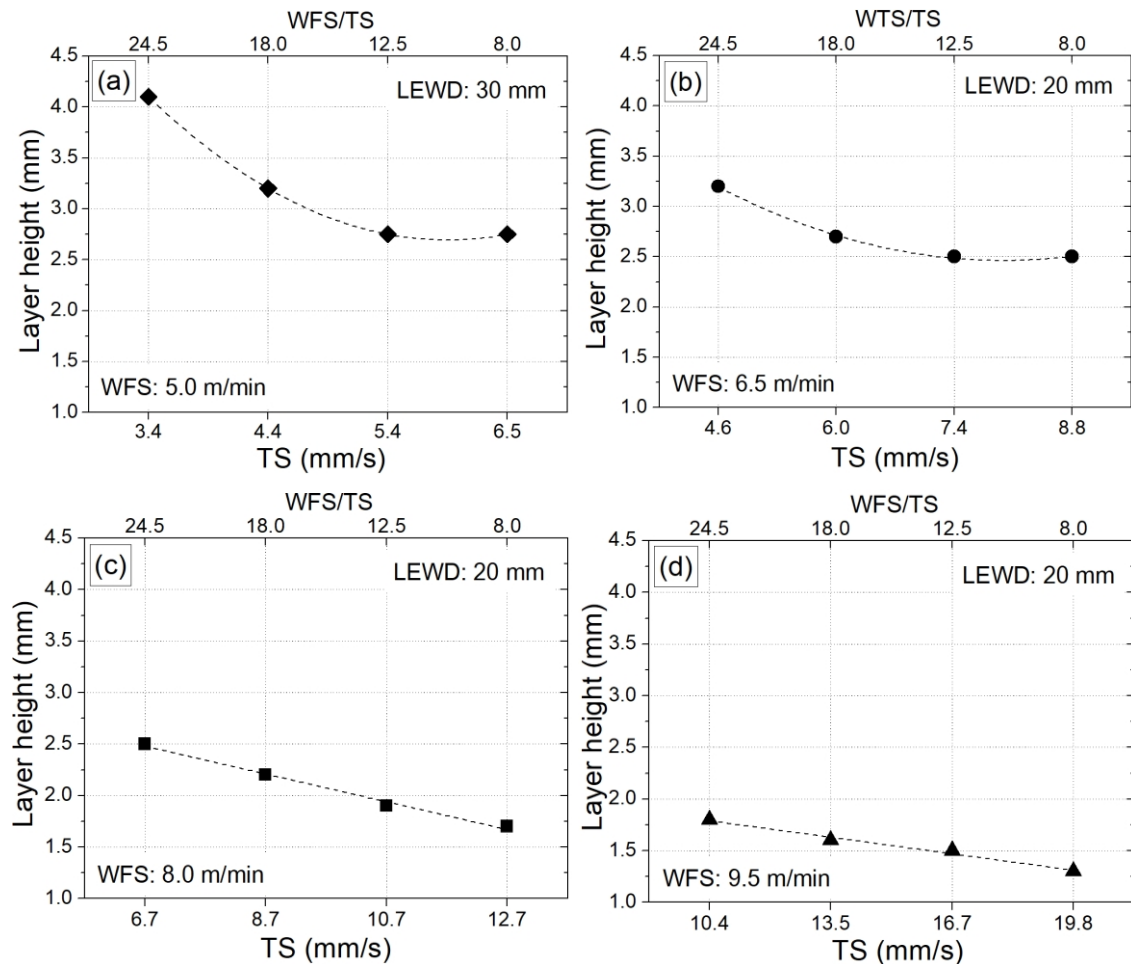
Figure 5.19. Layer height values that correspond to the work envelope

5.4 Proposal of parameter selection procedure for WAAM with the NIAC

The success and efficiency of WAAM operation strongly depends on the accurate selection of the deposition parameters. In this sense, the developed working envelope chart (Figure 5.18) can be a useful tool. However, when production cost and surface quality are taken into account, the task selecting parameters becomes more complex as stated by Yehorov et al. (2019).

Surface quality is directly related to SW, so that the lower the SW the higher the surface quality. For high-cost and difficult-to-machine materials, a minimal SW is desirable, since the higher SW the higher the excess of material to be machined on

post-processing and the higher material waste. In contrast, for non-expensive and easy-to-machine materials, a moderate SW level can be acceptable if the production is allowed to be high, *i.e.*, if high WFS and TS values can be applied.

Considering the cost of the material and its machinability, a parameter selection procedure for WAAM is proposed based on the following route:

1. For non-expensive and easy-to-machine materials, a moderated SW is acceptable, then the parameters to improve the production can be selected directly from the developed working envelope (Figure 5.18); and
2. For high-cost and difficult-to-machine materials, a minimum SW is required, then empirical modeling and numerical optimization should be performed simultaneously to meet a target geometry with a minimum SW.

5.4.1 Empirical modeling of the working envelope

An empirical model for the working envelope was developed by using the software Statistica® according the following steps:

a) Multiple regressions were performed considering all the predictors;
b) The significance of each predictor was evaluated through ANOVA (p-value);
c) The model was systematically reduced by removing the terms with the highest p-values one at a time until only the significant predictors were left;
d) A critical analysis of the model was carried out considering the R^2 value;
e) The residual plots were evaluated; and
f) The response surfaces were plotted, and their equations extracted.

The final modeling is summarized in Figure 5.20. The R^2 coefficients were higher than 0.90, *i.e.*, over 90% of the data variability can be explained by the models. In practice, this means that the developed model is not perfect but can be very useful. For all cases, the residuals tend to fit a normal distribution uniformly dispersed around the zero level, indicating that there was no systematic error during the experimental approach.

Total Wall Width - R²: 0.95
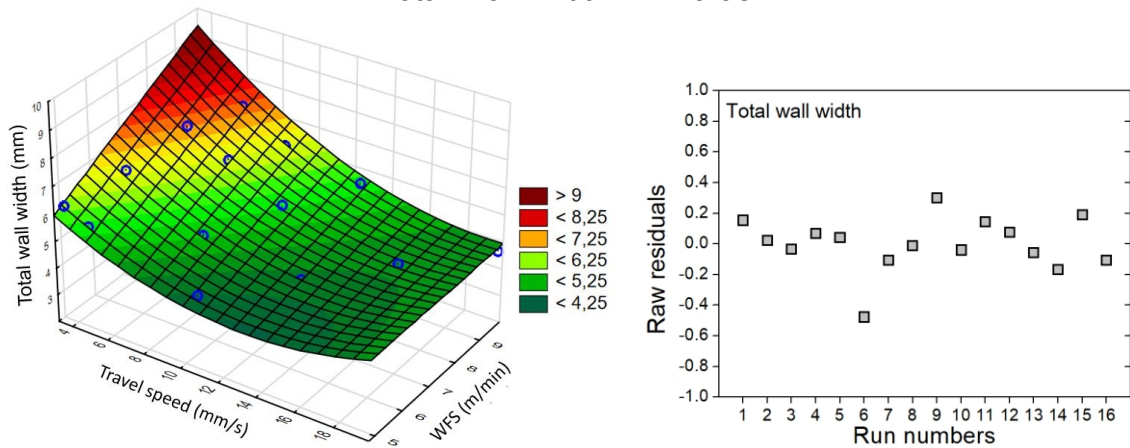
$$f(TWW) = 3.337 + 0.815 * WFS - 0.267 * TS + 0.017 * TS^2 - 0.041 * WFS * TS \quad (5.5)$$

Effective Wall Width - R²: 0.95
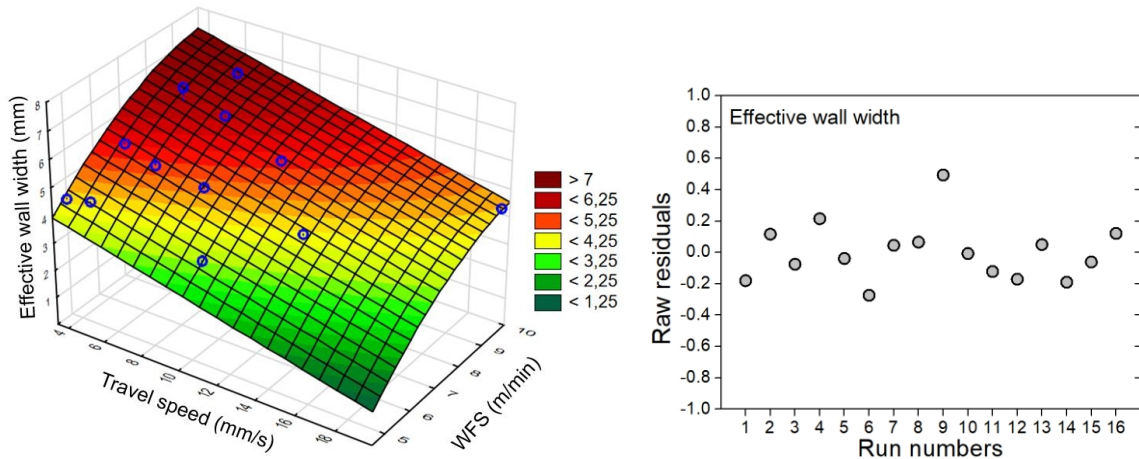
$$f(EWW) = 2.134 - 0.086 * WFS^2 + 1.861 * WFS - 0.166 * TS + 0.0005 * LWED^2 \quad (5.6)$$

Layer Height - R²: 0.90
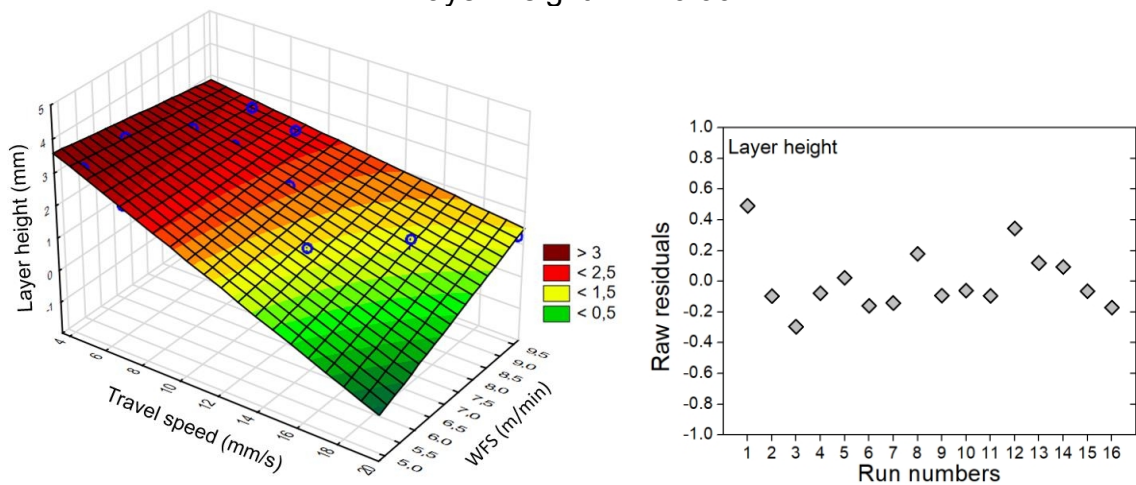
$$f(LH) = 5.865 - 0.280 * WFS - 0.426 * TS + 0.0355 WFS * TS \quad (5.7)$$

Figure 5.20. Summary of the multi-variate regression performed for the TWW, EWW and LH responses: Response surfaces, residual plots and regression equations

5.4.2 Numerical optimization and experimental validation

The empirical model was numerically optimized though the Differential Evolution[3] (Storn and Price, 1996) method in conjunction with a multi objective function based on the individual mean squared error (Koksoy and Yalcinoz, 2006). The aim of this optimization was to estimate the WFS, TS, LEWD and LH values for a given target wall width with a minimum difference between TWW and EWW, *i.e.*, with the minimum SW or highest surface quality possible. This aim was translated into the following composite objective function based on the individual mean squared errors:

$$Mi\,ni\,mi\,ze\left[\left(T - f(EWW)\right)^2 + \left(f(TWW) - f(EWW)\right)^2\right] \qquad (5.8)$$

where:

- T: target wall width;
- f(EWW): effective wall width function - Eq. (5.6); and
- f(TWW): total wall width function - Eq. (5.5).

Table 5.7 shows the WAAM parameters that were estimated for different target wall widths (T) after the proposed optimization. As one can see, all estimated parameters fall into operational map (Figure 5.3). Moreover, lower SW is expected because of the WFS/TS ratios were in a range between 8 and 16 (Figure 5.11).

Table 5.7. WAAM parameters that were estimated through the numerical optimization for different target wall widths (T)

T (mm)	4.0	4.5	5.0	5.5	6.0	6.5
WFS (m/min)	6.9	7.7	8.7	8.5	9.4	9.4
TS (mm/min)	14.1	14.8	15.2	11.7	10.8	9.3
LH (mm)	1.4	1.5	1.7	2	2.2	2.3
LEWD (mm)	27	22	20	20	20	20

---

[3] The DE MATLAB® code is available at International Computer Science Institute of Berkeley University website by courtesy of the Springer publisher.

The experimental validation of the empirical modeling and optimization procedure was performed by means of a deposition with the combination of parameters found for a target wall width (T) of 5 mm. As shown in Figure 5.21, the predicted parameters resulted in a preform with a EWW value quite near the target and with very low SW.

TWW (mm)	5.30
EWW (mm)	5.06
LH (mm)	1.7
SW (mm)	0.12
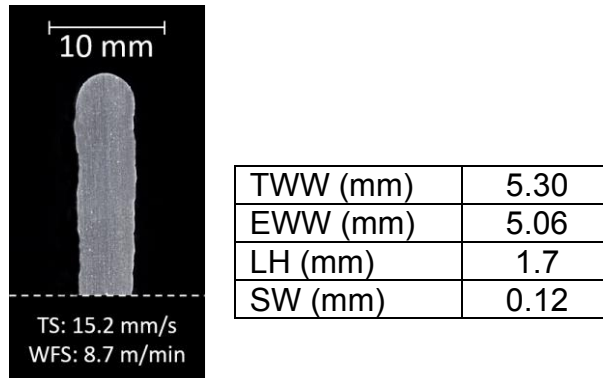
Figure 5.21. Experimental validation of the empirical modeling and optimization procedure and WAAM parameters for a target wall width (T) of 5.0 mm

5.4.3 Flowchart of the parameter selection procedure for WAAM

Figure 5.22 illustrates the procedure that was established for selecting the parameters in WAAM in form of a flowchart. It all begins with a critical analysis of the model considering the design rules postulated by Lockett et al. (2017). If there is no working envelope developed for the material specified in the project, the feasibility of developing one should be assessed considering the material weldability, commercial availability, development cost, etc. The target wall width is determined by the minimum section of the component. It could be a stacked single pass deposition or a combination of multiple passes, as discussed by Yehorov et al. (2019). The parameters may be changed along the building process, even though most of the commercial AM equipment does not allow such an approach. The required surface quality is linked to the material cost and its machinability. Depending on the case, the parameters can be selected directly from the working envelope or through a numerical optimization. Regardless of the selection parameter procedure, both should be experimentally validated before slicing the CAD model, which precedes the generation of the deposition path and the following execution of the actual deposition of material via WAAM.
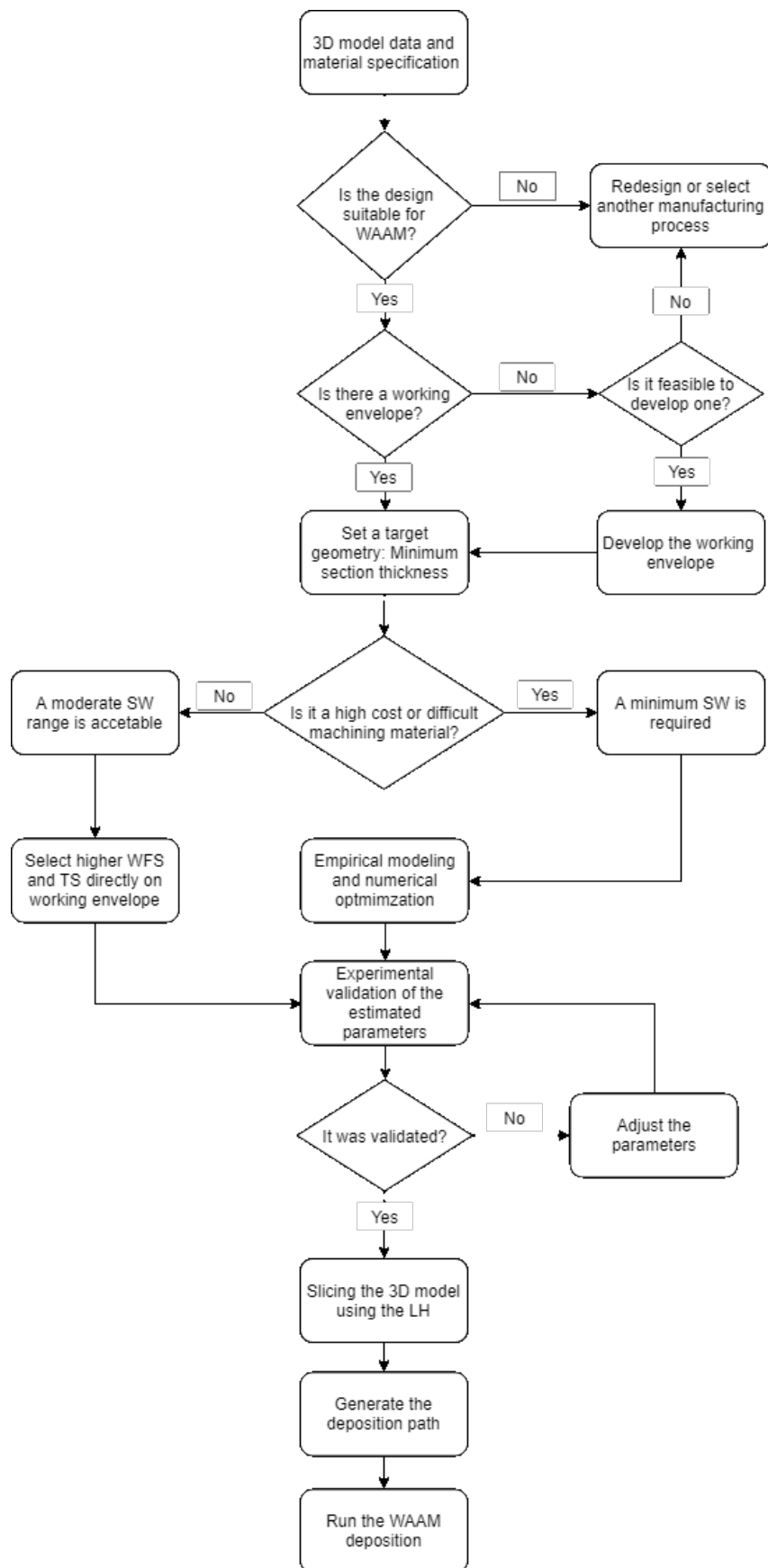
Figure 5.22. Flowchart of the procedure for selecting the parameters in WAAM (by the author)

5.5 Partial remarks

- In the first approximation, the experimentally based working envelope was quite limited. The main limitations were the excessive oxidation of the layer top surface of the preforms deposited with high WFS values and the excessive SW of the lateral surfaces of the preforms deposited with lower WFS values. All the preforms reached and acceptable level of relative density;

- To deal with the excessive oxidation, a supplementary shielding gas system was devised. The LEWD was increased from 20 to 30 mm to reduce the surface waviness, after a few troubleshooting steps, the working envelope was significantly expanded;

- The trends predicted by the analytical model found experimental support, so that it can be used as a first approximation for the working envelope development;

- For all the conditions assessed the SW levels tended to fit a parabolic behavior with minimum values at a WFS/TS around 12.5 (arc energy per unit length of deposit: 90-100 J/mm). However, it is worth mentioning that even the maintenance of a constant WFS/TS ratio does not guarantee satisfying results;

- For non-expensive and easy-to-machine materials a moderated SW is acceptable, hence the parameters for high production can be selected directly from the developed working envelope; and

- For high-cost and difficult-to-machine materials a minimum SW is required, hence the empirical modeling and the numerical optimization should be performed to meet a target geometry with a minimum SW simultaneously.

CHAPTER VI - ASSESSMENT OF THE NIAC FUNCTIONALITY IN A RELEVANT ENVIRONMENT: WAAM OF SCALMALLOY®

6.1 Contextualization

Based on the information collected in the literature and compiled in Table 6.1, it can be said that there is a gap of information related to DED of Scalmalloy®, which might be related to the possibility of its in-process overaging due to thermal history imposed by the deposition as reported by Rometsch et al. (2014) for Laser Metal Deposition (LMD). The Scalmalloy® overaging problem resides in the fact that it cannot be reversed through a post heat treatment, because the solubilization temperature of the scandium aluminides is close to the melting temperature of the Al-Mg matrix (Røyset and Ryum, 2005). This potential setback might be even more harmful in WAAM due to its characteristic high heat input and, without proper thermal management, heat accumulation. In this sense, thermal management techniques that may allow the Scalmalloy® to be processed by high deposition processes, such as by WAAM, without compromising its mechanical properties are of great interest and this is the subject of this chapter.

Table 6.1. A brief state of the art on Scalmalloy® processing and aging treatment

Reference	Experimental approach	Main remarks
Lohar et al. (2010)	Al-0.3Sc-0.15Zr alloy was cast under different cooling rates (from 0.16 to 7,69 °C/s). One set of experiments consisted of the samples aged for 2 h at temperatures of 300, 400, 500 and 600 °C. Another set of samples were aged at 300 °C for variable times starting at 30 min and going up to 24 h.	The higher the cooling rate the greater the aging response. The peak age hardness was with 300 °C and 3 h. There is a drop on hardness on ageing at 400 °C in all the samples due to an overaging effect.
Rometsch et al. (2014)	A 115 mm high bar of Al 0.9 wt.% Sc was fabricated by LMD to evaluate the effect of thermal history on the aging response. The aging treatments were carried out during 0.2 - 2 - 24 - 192 h at 325 °C.	In the as-fabricated condition, the hardness decreases from 78 HV5 at the bottom to 34 HV5 at the top of the bar. Upon ageing, there is no ageing response up to a height of about 70 mm due over aging caused by the thermal history imposed by the process. The hardness quickly reaches a relatively flat peak with 2 h and 325 °C.
Taendl et al. (2014)	Al-Mg4-Sc0.4-Zr0.15 alloy with different solidification rates were compared in as-cast and aged conditions. Furthermore, a sample was re-solidified using an electron beam process, and the microstructure and hardness in re-solidified and aged conditions were compared to that of the as-received material. Samples were aged at 325 °C for 1h, which led to peak hardening.	The hardness before ageing reaches a similar level for all samples. With increasing solidification and cooling rates, the precipitation of $Al_3(Sc,Zr)$ is suppressed, leading to more Sc and Zr supersaturation at room temperature. The aging response increases with an increase in the Sc-Zr supersaturation prior to ageing and it is hence related to an increasing solidification rate.
Taendl et al. (2016)	The authors investigated the age hardening behavior of Al-Mg4-Sc0.4-Zr0.12 alloy in a temperature range between 250 and 400 °C within 180 min as a function of the quantitative degree of scandium supersaturation prior to ageing.	For a Sc-content of 0.37 wt.%, it was showed that the peak ageing can be achieved after ageing at 325 °C for 180 min, leading to a considerable hardness increase of around 70%. The samples with a higher degree of Sc supersaturation showed more pronounced age hardening response.
Tang et al. (2017)	Al-0.2Sc and Al-0.4Sc alloys were cast. The specimens for microstructure observation and tensile test were cut from the casts, and some were subjected to further heat treatment: solubilized at 640 °C for 24 h, followed by a water quench at room temperature, and aged at 300 °C for 3 h.	After further aging at 300 °C for 3 h, a great number of fine Sc_3Al particles are precipitated in the Al matrix, which leads to a considerable precipitation hardening effect.

*to be continued

Table 6.1. A brief state of the art on Scalmalloy® processing and aging treatment (continuation)

Ref	Experimental approach	The main remarks
Spierings et al. (2017)	Scalmalloy® powder with a nominal composition of Al-4.6Mg-0.66Sc-0.42Zr-0.49M was deposited by PBF-L. In order to determine relevant heat temperature ranges where precipitation occurs, heat treatments at temperatures between 250 °C and 500 °C (at steps of 50 K) are applied for 4 h. In addition, the effects of the treatment hold duration were analyzed for 0.5, 1, 2, 5, 10 and 24 h at 275, 325 and 375 °C.	At higher temperatures exceeding 400 °C (with soak time of 4 h), the hardness reduces significantly (overaging). It appears that 275 °C is not enough to reach the full hardness, as even after prolonged ageing times the hardness level still increases. The aging treatments performed at 325 °C and not exceeding 350 °C, with an aging duration of 4 h, showed the best compromise between hardness and mechanical properties.
Shi et al. (2018)	Al-3.4Mg-1.08Sc-0.23Zr-0.5Mn-0.5Cu powder was processed by PBF-L. The aim was to assess how microstructure, porosity characteristics, aging response and mechanical properties change when the platform temperature is increased from 35 to 200 °C. Aging treatments were carried out at 300 °C.	The peak hardness occurs after about 12 h at 300 °C. In the as-fabricated condition, the hardness of samples built on top of a 200 °C platform is higher than that built at 35 °C. This is due to the aging effect provided by the higher platform temperature. There is no significant difference in hardness between the use of the two platform temperatures after peak aging. The mechanical properties had a behavior similar to that of the hardness.
Zhao et al. (2018)	Al-4.55Mg-0.51Mn-0.65Sc-0.30Zr was processed by DED-L in a bi-directional and uni-directional strategy. Hardness tests were conducted on specimens aged at 300 °C for up to 19 h to observe the ageing responses.	The grain size is lower at the top than at the bottom of the parts. The difference in grain size correspond to a small difference in hardness. The aging response is more significant in the first 3 hours. It appears that a lower laser energy and a unidirectional deposition strategy showed better aging response.
Schmidtke et al. (2011)	Al-4.5Mg-0.66Sc-0.37Zr-0.51Mn was processed by PBF-L. The most suitable ageing response was expected at 325° for 4 hours. Aging response was assessed through hardness tests.	The aging treatment at 325°C for 4 hours showed the desired effect. The average hardness increased from 105 to 177 HV0.3. The high strength properties indicate that sufficiently high cooling rates occurred during the laser additive manufacturing and that a supersaturated solid solution was realized. The stress-strain-curves of the specimens were nearly identical for each orientation, indicating high isotropy level. The addition of scandium led to high strength but ductile behavior. A grain refinement was achieved that caused high plasticity compared to other high strength Al alloys.

6.2 Methodology

In order to evaluate the functionality of the NIAC technique in a relevant environment, thin walls of Scalmalloy® were deposited by WAAM with the NIAC technique under different processing conditions. For comparison purposes, preforms were also deposited under the Natural cooling approach, but always waiting for the preform to cool down up to a given interpass temperature before the deposition of a new layer. This interpass temperature was estimated from the measurements taken from the depositions with the NIAC. After deposition, the preforms were cut in half in their lengths, being those parts cut again in half, one part to allow the geometric aspects and porosity to be evaluated, and the other subjected to heat treatment. Hardness profiles were conducted along the height of preforms in an as-built and in a heat-treated condition to assess the precipitation response as well as the in-process overaging. The current literature employs several advanced microscopy techniques to characterize Al alloys for AM, as per Taendl et al. (2016), Spierings et al. (2018), Yang et al. (2018), among others. However, considering the proposal of this chapter, the analyses were focused on hardness because, while being simple, it is an inexpensive, affordable and effective approach for evaluating the effect of processing in a whole sample. The following hypotheses were raised depending on the possible precipitation responses:

1) If the hardness varies significantly along the preform height it means that precipitation or coalescence has occurred due to thermal history imposed by the layered approach of WAAM;

2) If hardness increases after the heat treatment (positive precipitation response), it means that a share of scandium remained in the supersaturated solid solution during processing and Al_3Sc precipitated due to the heat treatment;

3) If the hardness remains similar after the heat treatment (no response to precipitation), it means that Al_3C precipitated during deposition and the heat treatment did not promote overaging. It is also reasonable to assume that the samples were already overaged in the "as-built" condition and therefore did not respond to precipitation; and

4) If the hardness decreases after the heat treatment (negative precipitation response), it means that Al_3Sc precipitated during the deposition and overaged due to the heat treatment.

6.3 Experimental procedures

The experiments were performed on the NIAC functional prototype described in Chapter 4. The deposition conditions were like those ones described in Chapter 5 and are summarized in Table 6.2. The experimental trials were carried out with the supplementary shielding gas device to mitigate excessive oxidation. In addition, good welding practices regarding the substrate and the wire cleaning were also applied.

Table 6.2. Deposition conditions for WAAM of Scalmalloy®

Arc deposition equipment	Fronius CMT - TransPuls Synergic 500
Wire (deposition material)	Scalmalloy® - Ø 1.0 mm
Substrate	Al5052 (260 x 38.1 x 6.4 mm)
CTWD*	12 mm
Shielding gas	Commercial argon - 15 L/min
Cooling liquid	Tap water at around 20 ºC
Work tank volume	50 L
Preform geometry	Thin wall with a height of 50 and length of 250 mm
Building strategy	Single-pass multi-layers bidirectional depositions
Dwell time	10 s/layer

*CTWD: contact tip to work distance

The deposition parameters were selected from the developed working envelope (Chapter 5) and are presented in Table 6.3 and in Table 6.4. Although the working envelop was developed to the ER 5356 alloy (Al5Mg), it is expected that it also works for the Scalmalloy® case because their chemical compositions are quite similar in terms of major elements, as shown in Table 6.5.

Table 6.3. Matrix of experiments for WAAM of Scalmalloy®: variation of WTS/TS for a constant LEWD

Run	WFS (m/min)	TS (mm/s)	WFS/TS (1)	Z increment (mm)	LEWD (mm)
1		4.4	24.5	3.2	
2		6.0	18.0	2.7	
3	6.5	8.7	12.5	2.2	20
4		13.6	8.0	1.6	
5		24.1	4.5	1.4	

Table 6.4. Matrix of experiments for WAAM of Scalmalloy®: Variation of LEWD for a constant WTS/TS

Run	WFS (m/min)	TS (mm/s)	WFS/TS* (1)	Z increment (mm)	LEWD (mm)
6					10
7					20
8	6.5	8.7	12.5	2.2	30
9					40
10					Natural IT: 65 - 75 ºC*

* This interpass temperature (IT) range was estimated from the measurements taken in run 3 of Table 6.3 (from the depositions with the NIAC)

Table 6.5. Results of the Scalmalloy® wire chemical analysis (provided by the supplier)

Spool	Al	Mg (wt. %)	Sc (wt. %)	Zr (wt. %)	Ti (wt. %)
1	Balance	4.68	0.42	0.086	0.13
2	Balance	4.64	0.44	0.095	0.15

The actual deposition parameters (WFS, current and voltage) were measured with the DAQ system described in Chapter 4. The average instantaneous power method (Eq. (5.1)) was employed to calculate the arc energy per unit length of deposit.

The preform temperature was measured by a pyrometry (as in Chapter 4). A parallel critical review on measuring thermal cycles with pyrometers was made by the author and published somewhere else (Silva et al., 2019). In this review the advantages and drawbacks of IR pyrometry in comparison with other techniques were presented. Based on the brief state of the art compiled, IR pyrometry with a focusable optics might be considered as a feasible technique for non-contact and in-situ interpass temperature measurements with high spatial resolution (small spot size), yet there are still ongoing promising advancements. The main setback presented in this paper is

related to the difficulty to set the emissivity of the material of interest. In the present work, data from a K-type thermocouple (Ø 0.6 mm each wire) was used to estimate the emissivity in 20%.

The porosity was indirectly assessed through relative density by using the Archimedes principle. The wire density was estimated by the same method and used as the reference. Geometrical features (TWW, EWW and LH) were measured considering the definitions of Martina et al. (2012), as described in Chapter 5.

The heat treatment was performed in a calibrated muffle furnace and the parameters used followed the Scalmalloy® supplier's recommendations (APWorks, 2017): 325 °C during 4 hours. Initially, the furnace was preheated for 4 hours to stabilize its internal temperature. After 4 hours of treatment, the samples were through water quenching.

The Vickers hardness profiles were performed at longitudinal sections as illustrated in Figure 6.1. The samples for that were machined to obtain a flat surface and then were ground according to standard procedures. A load of 1 kg (HV1) and a step distance of 1 mm between indentations were used.
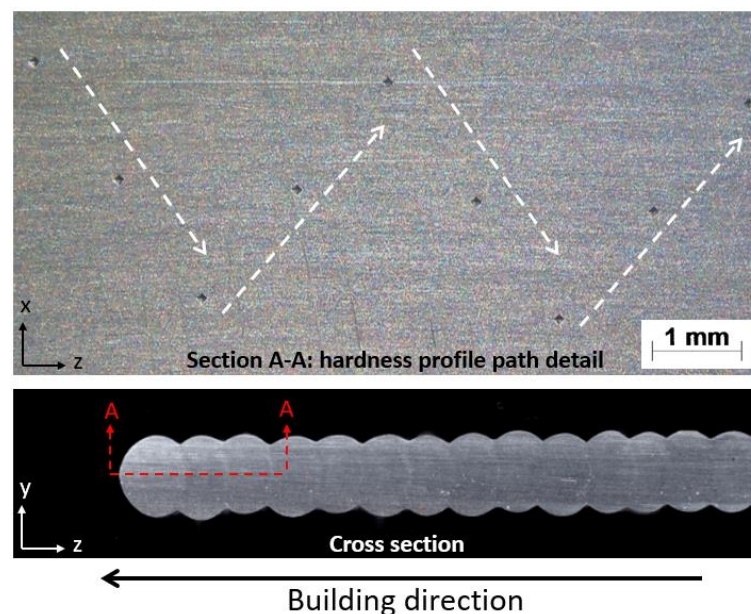

Figure 6.1. Example of a hardness profile performed along a a sample of Scalmalloy® produced via WAAM (by the author)

The precipitation response was estimated according to Eq. (6.1).

$$PR \; = \frac{H_{ht} - H_{ab}}{H_{ht}} * 100\% \qquad\qquad (6.1)$$

Where:

PR: precipitation response (%);

H_{ab}: average sample hardness in the as-built condition; and

H_{ht}: average sample hardness in the heat-treated condition.

An identification of phase was tried via X-ray diffraction (XRD) with Cu Kα radiation in a continuous scan mode at 40 kV and 40 mA. A quick scan speed of $4°\text{min}^{-1}$ was first applied over a wide range of $2\theta = 30\text{-}80°$ to get a general overview of the diffraction peaks. Then, a slow scan rate at $1°\text{min}^{-1}$ was performed over $2\theta = 37\text{-}39°$ to obtain a further accurate information about Al_3Sc diffraction peaks (Li et al., 2019). These analyses were performed along longitudinal sections just as for the hardness case.

6.4 Results and discussion

6.4.1 Analysis of the deposition parameters

Initially, the arc energy per unit length of deposit (AE) was plotted against the WFS/TS ratio to validate the assumption that these factors are directly proportional. As one can see in Figure 6.2, the relationship between the arc energy (AE) and the WFS/TS quite fit a linear behavior. In practice, these results allow to state, for the tested conditions, that the higher the WFS/TS ratio the higher the arc energy. This is expected since the CMT synergistic control keeps the arc length very short and constant and due to the fact that the WFS/TS was kept constant while the TS was varied (Table 6.3).
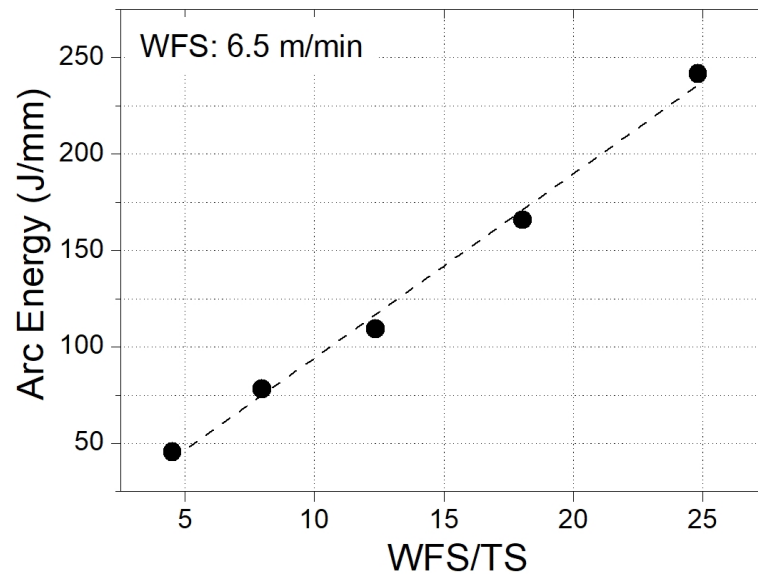
Figure 6.2. Correlation between WFS/TS and arc energy for WAAM of Scalmalloy®

6.4.2 Thermal features

6.4.2.1 Average interpass temperature estimation

As described in Chapter 4, the temperature data from the trailing/leading IR pyrometer during all the deposition time tends to fit a bimodal distribution and the first quartile (Q1) is representative of the average interpass temperature. Figure 6.3 shows the boxplot of the temperature data measured by the trailing/leading pyrometer for WAAM of Scalmalloy®, where Q1 is the bottom line of the box. As expected, for a constant LEWD, the lower the WFS/TS ratio or the arc energy value the lower the average interpass temperature. Conversely, for a constant WSF/TS and arc energy, the higher the LWED the higher the average interpass temperature. The average interpass temperature values for both conditions are presented in Table 6.6 and in Table 6.7.
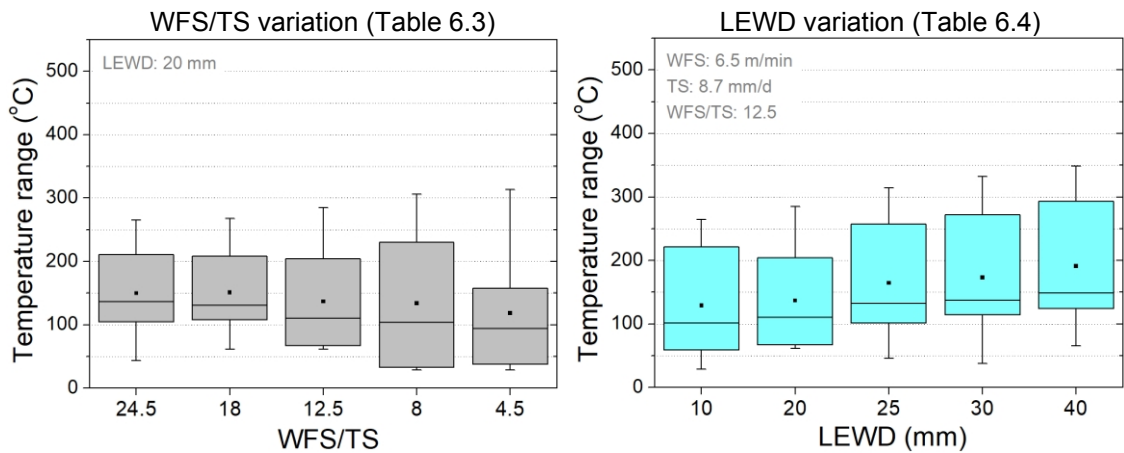
Figure 6.3. Effect of the WFS/TS ratio and LEWD value on the thermal features measured with the trailing/lading IR pyrometer for WAAM of Scalmalloy®

Table 6.6. Average interpass temperature versus the WFS/TS variation for WAAM of Scalmalloy® (Table 6.3)

	WFS/TS: 24.5	WFS/TS: 18	WFS/TS: 12.5	WFS/TS: 8	WFS/TS: 4.5
Average IT (°C)	104	108	67	33	39

Table 6.7. Average interpass temperature versus the LEWD variation for WAAM of Scalmalloy® (Table 6.4)

	LEWD: 10 mm	LEWD: 20 mm	LEWD: 25 mm	LEWD: 30 mm	LEWD: 40 mm
Average IT (°C)	59	67	101	114	124

6.4.2.2 Cooling rate estimation procedure

The cooling rates for WAAM of Scalmalloy® were estimated by the following procedure:

1) Measurement of the thermal history experienced by a fixed target of the preform during the deposition of some layers or until the water level reaches the fixed target;

2) Determination of the trends (fitting curve) of the peak temperature as a function of the distance from the top layer;

3) Establishing a correlation between the peak temperature reached and the cooling rate. The cooling rate for each thermal cycle was estimated considering the temperature range between 90 and 70% of the peak temperature; and

4) Estimation of the cooling rate for a given peak temperature.

The thermal history of the preforms was measured at a fixed target by pyrometry, as described in Chapter 4. A typical thermal history of a Scalmalloy® preform deposited by WAAM with the NIAC technique is presented in Figure 6.4, where each thermal cycle corresponds to the deposition of a layer. The peak temperature measured at a fixed point tends to decrease as the layers are deposited because the arc moves away from the measurement point. Unlike expected, the peak temperature in the first two measurements was lower than in the following ones. This fact may be related to a lower emissivity in the area of cathodic cleaning produced by the arc. Therefore, the first two measurements were not considered.
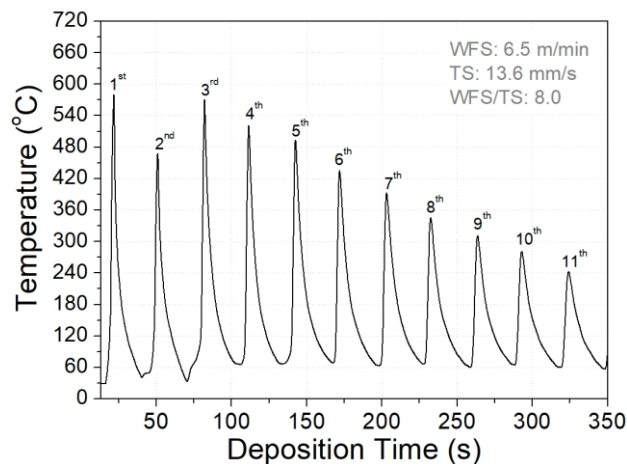
Figure 6.4. Example of thermal history measured by pyrometry in a fixed target of a Scalmalloy® preform deposited by WAAM

The peak temperatures observed in the thermal history (Figure 6.4), except the first two, were used to determine trends between peak temperature as a function of the distance from the top layer, as shown in Figure 6.5. It can be noticed that if the distance from the top is extrapolated to zero (*i.e.*, to the melting pool), the estimated peak temperature is in between the typical liquidus and solidus boundaries for aluminum alloys, which seems to be physically reasonable.
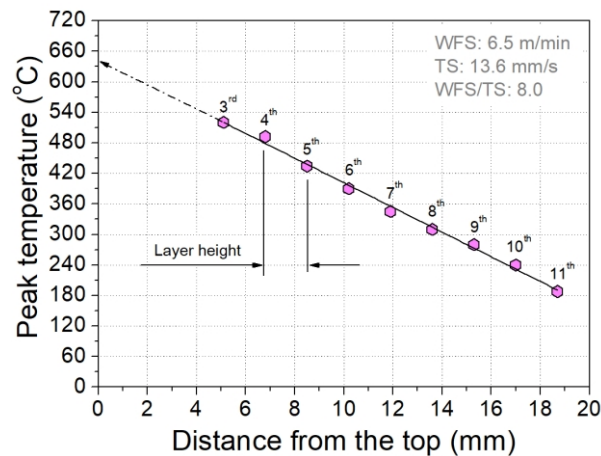
Figure 6.5. Correlation between the peak temperature of a layer and the distance from de top layer of a Scalmalloy® preform deposited by WAAM

The cooling rate for each thermal cycle was estimated considering the temperature range between 90 and 70% of the peak temperature. A typical correlation between the cooling rate and the peak temperature is showed in Figure 6.6. As expected, the cooling rate tends to increase as the peak temperature increases.
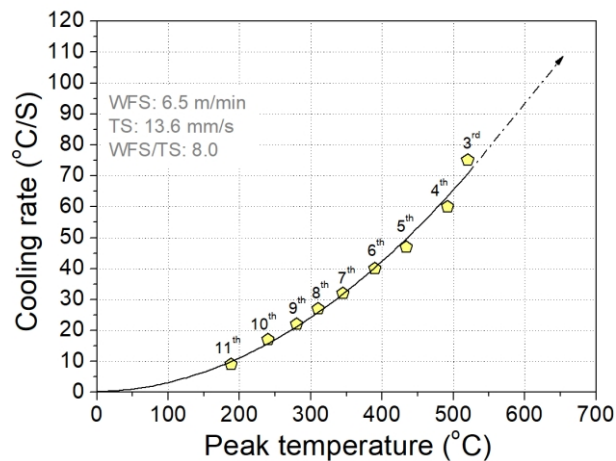
Figure 6.6. Example of correlation between the peak temperature and the cooling rate of a Scalmalloy® preform deposited by WAAM

6.4.3 Effect of the processing condition on the cooling rate

The cooling rate was estimated considering a peak temperature of 650 °C, which corresponds to the solvus temperature for an aluminum alloy containing 0.4 wt.% of Sc (Røyset and Ryum, 2005).

The effect of the WFS/TS ratio and LEWD value on the cooling rate are presented in the Figure 6.7 and Figure 6.8, respectively. The higher the WFS/TS (arc energy) and the LEWD (interpass temperature) the lower the cooling rate, which is in accordance with what has been postulated for heat transfer in welding (Kou, 2002). It is interesting to notice in Figure 6.8 that the higher the LEWD the more the cooling rate tends to approach the estimated for the Natural condition, which sounds reasonable.
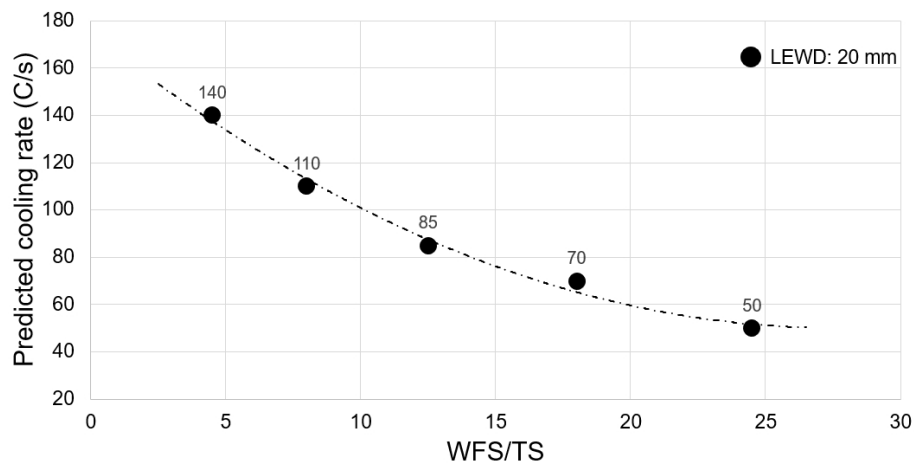
Figure 6.7. Effect of the WFS/TS ratio on the cooling rate of a Scalmalloy® preform deposited by WAAM
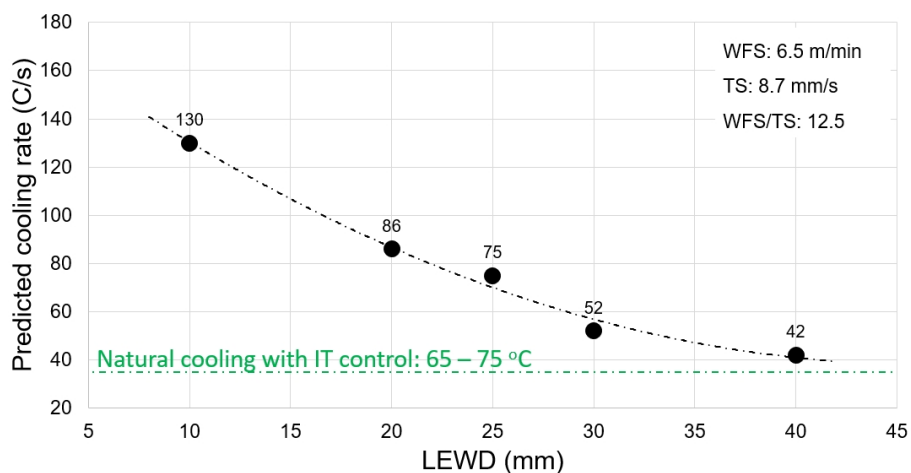
Figure 6.8. Effect of the LEWD value on the cooling rate of a Scalmalloy® preform deposited by WAAM

As just shown, the cooling rate can be changed through the WFS/TS ratio and/or the LEWD value. However, variations of these parameters imply variation in geometry. In this sense, Figure 6.9 highlights the potentiality that the NIAC technique has to

change the cooling rate for a target geometry. This characteristic may allow to produce components with tailored properties along the volume.
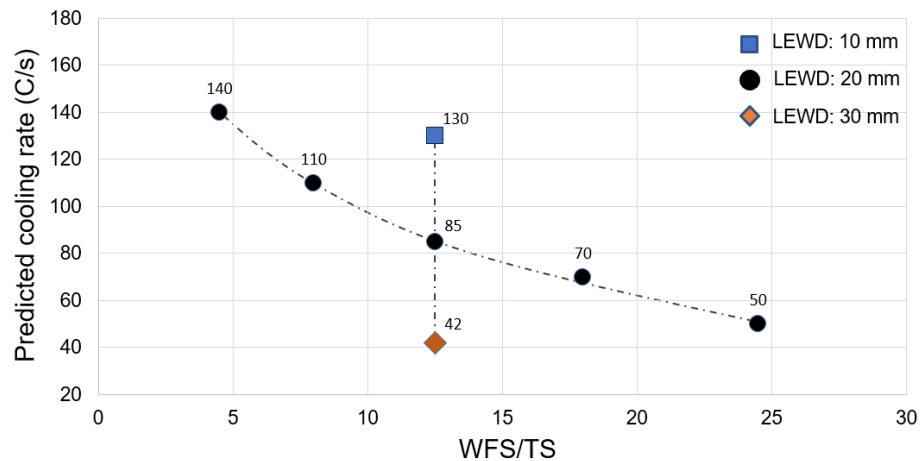
Figure 6.9. NIAC potentiality to produce components with tailored properties (data from a Scalmalloy® preform deposited by WAAM)

6.4.4 Geometrical features and relative density

In general, all Scalmalloy® preforms presented a bright and smooth surface. The surface waviness and relativity density were within acceptable ranges. The width of the walls remained virtually constant along their heights, suggesting that there was no significant heat accumulation throughout the depositions.

Figure 6.10 shows the lateral surface aspect and the cross-sectional view of the Scalmalloy® preforms deposited with different WFS/TS ratios for a LEWD of 20 mm, while Table 6.8 summarizes the geometrical values that were found. As expected, for a given WFS, the larger the TS the smaller the wall width and the lower the layer height. In addition, the SW tends to be smaller the smaller the WFS/TS.

For the WFST/TS of 12.5, the LEWD variation had no significant effect on the geometric features, as compiled in Figure 6.11 and Table 6.9. For the Natural condition, if the interpass temperature is equivalent to that obtained with the NIAC technique, the preform geometry also tends to be similar, but the deposition time is significantly longer (more than 7 times) due to dead (dwell) time in between the layers. In fact, it is expected that below a certain level, the interpass temperature will have no significant effect on the geometry.

Travel speed increases →

Lateral view

Cross section

TS: 4.4 mm/s	TS: 6.0 mm/s	TS: 8.7 mm/s	TS: 13.6 mm/s	TS: 24.1 mm/s
WFS: 6.5 m/min	WFS: 6.5 m/min	WFS: 6.5 m/min	WFS: 6.5 m/min	WFS: 6.5 m/min
WFS/TS: 24.5	WFS/TS: 18.0	WFS/TS: 12.5	WFS/TS: 8.0	WFS/TS: 4.5
AE: 240 J/mm	AE: 165 J/mm	AE: 110 J/mm	AE: 78 J/mm	AE: 45 J/mm
LEWD: 20 mm	LEWD: 20 mm	LEWD: 20 mm	LEWD: 20 mm	LEWD: 20 mm

Figure 6.10. Lateral aspect and cross-sectional view of Scalmalloy® preforms deposited by WAAM relative to the experiments from Table 6.3 : Variation of the WFS/TS ratio for a LEWD of 20 mm

Table 6.8. Geometrical features, relative density and deposition details of Scalmalloy® preforms deposited by WAAM relative to the experiments from Table 6.3: Variation of the WFS/TS ratio for a LEWD of 20 mm

WFS/TS	TWW (mm)	EWW (mm)	SW (mm)	LH (mm)	Relative Density (%)	Dep. Time* (min)	Number of layers*
24.5	6.6	5.6	0.5	3.5	98.4	18.8	16
18.0	5.9	5.3	0.3	2.8	98.3	18.4	20
12.5	5.3	4.9	0.2	2.2	98.5	16.8	24
8.0	4.8	4.0	0.4	1.7	98.0	15.5	30
4.5	3.5	3.2	0.15	1.2	97.1	14.9	44

* The deposition time and the number of layers are relative to a preform with a length of 250 mm and a height of approximately 50 mm.
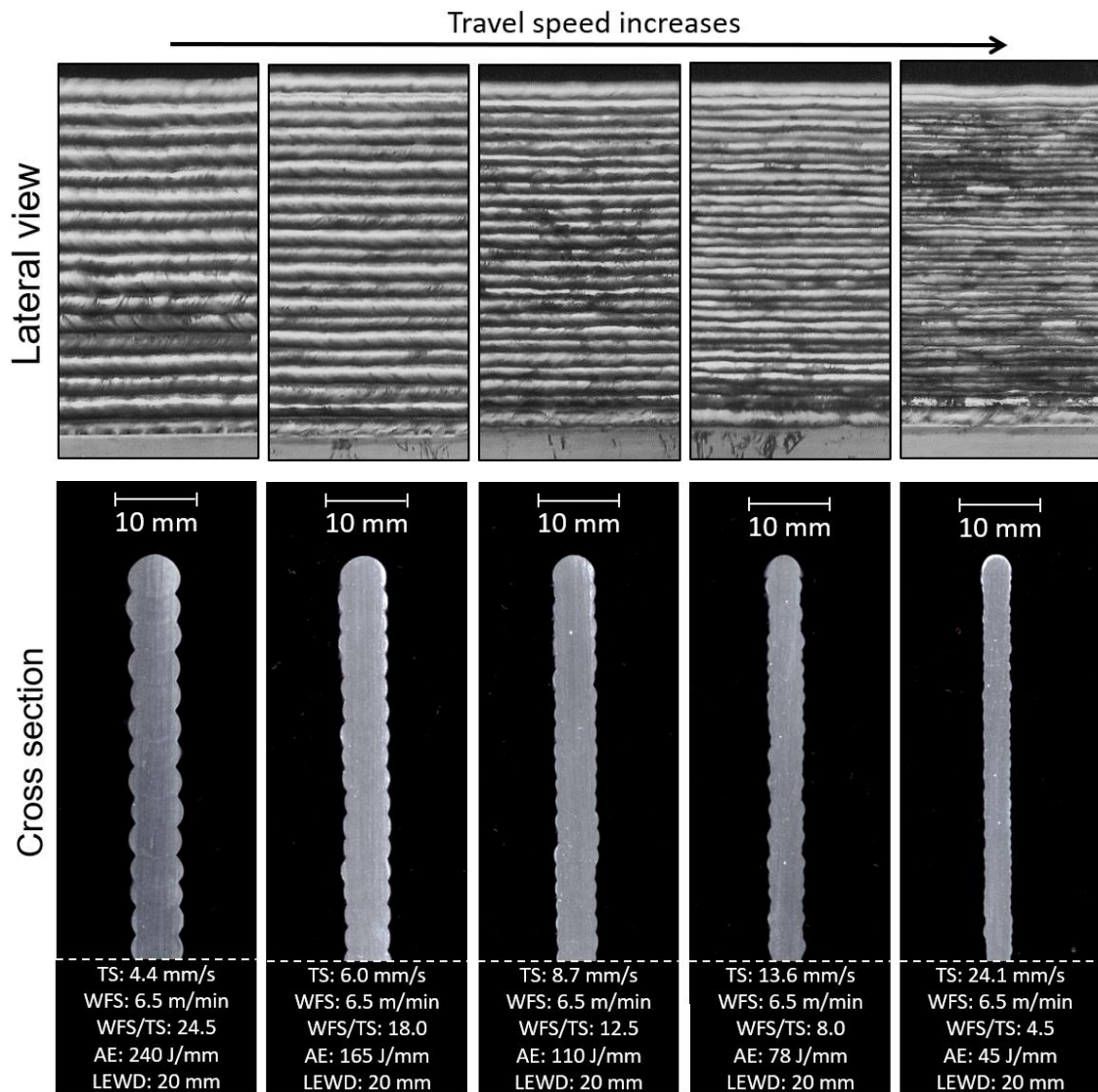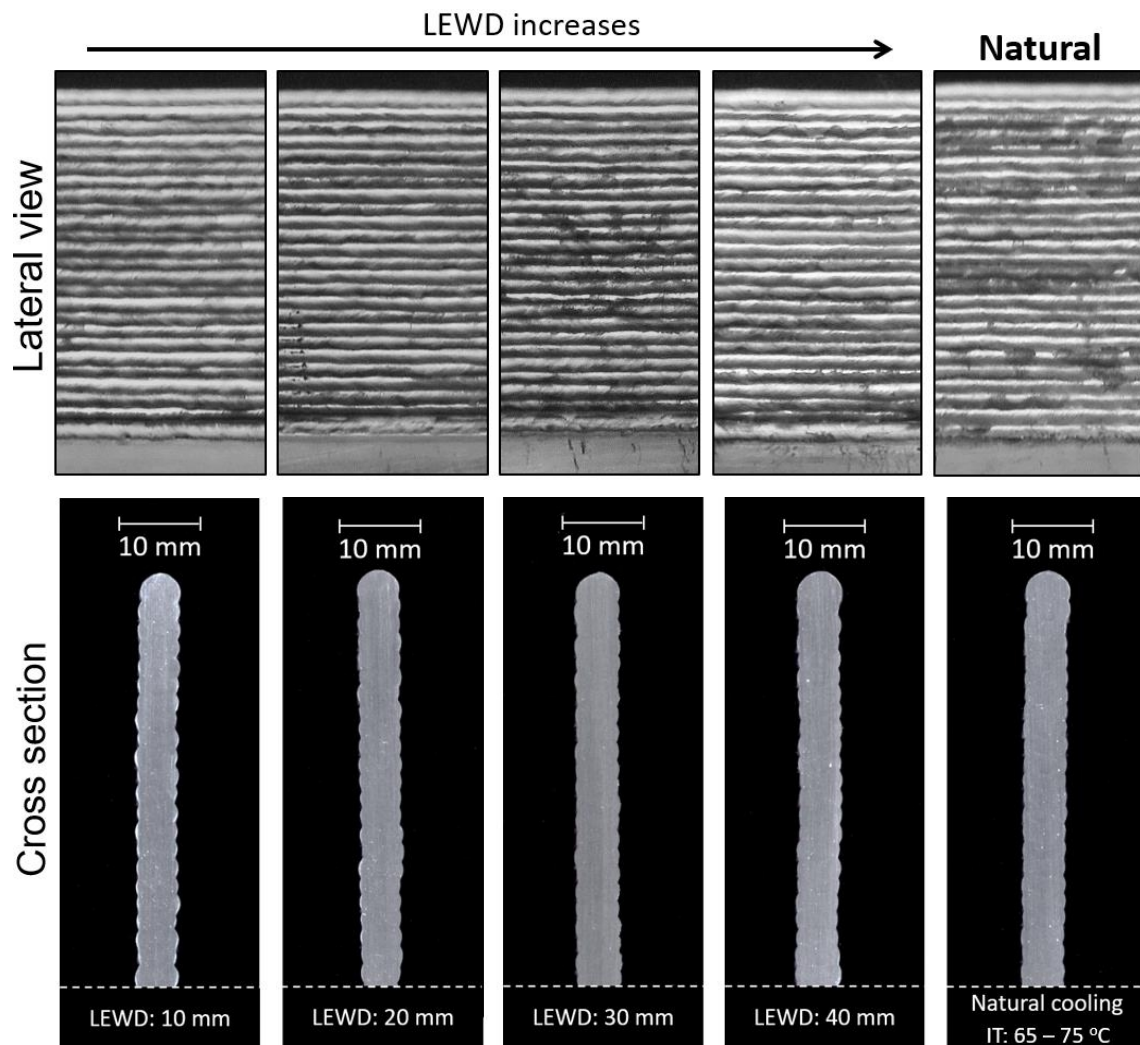
Figure 6.11. Lateral aspect and cross-sectional view of Scalmalloy® preforms deposited by WAAM relative to the experiments from Table 6.4: Variation of the LEWD value for a WTS/TS of 12.5

Table 6.9. Geometrical features, relative density, deposition details of Scalmalloy® preforms deposited by WAAM relative to the experiments from Table 6.4: Variation of the LEWD value for a WFS/TS of 12.5

LEWD	TWW (mm)	EWW (mm)	SW (mm)	LH (mm)	Relative Density (%)	Dep. Time (min)	Number of layers
10	5.2	4.8	0.2		98.1		
20	5.3	5.12	0.2	2.25	98.5	16.8	24
30	5.4	5.12	0.15		98.1		
40	5.2	4.9	0.15		96.1		
Natural**	5.5	5.1	0.2	2.25	96.2	121	

* The deposition time and the number of layers are relative to a preform with a length of 250 mm and a height of approximately 50 mm.
**In the Natural condition, the interpass temperature was kept between 65-75 ºC.

6.4.5 Precipitation response

Through the typically flat hardness profile observed in Figure 6.12 one can say that for the tested conditions no overaging occurred due to the thermal history imposed by WAAM with the NIAC technique. This result was not expected for the Natural approach because it differs from what was reported by Rometsch et al. (2014). This divergence can be explained considering that there was not enough time or temperature to promote precipitation and coalescence of precipitates. However, it could occur for longer deposition times.
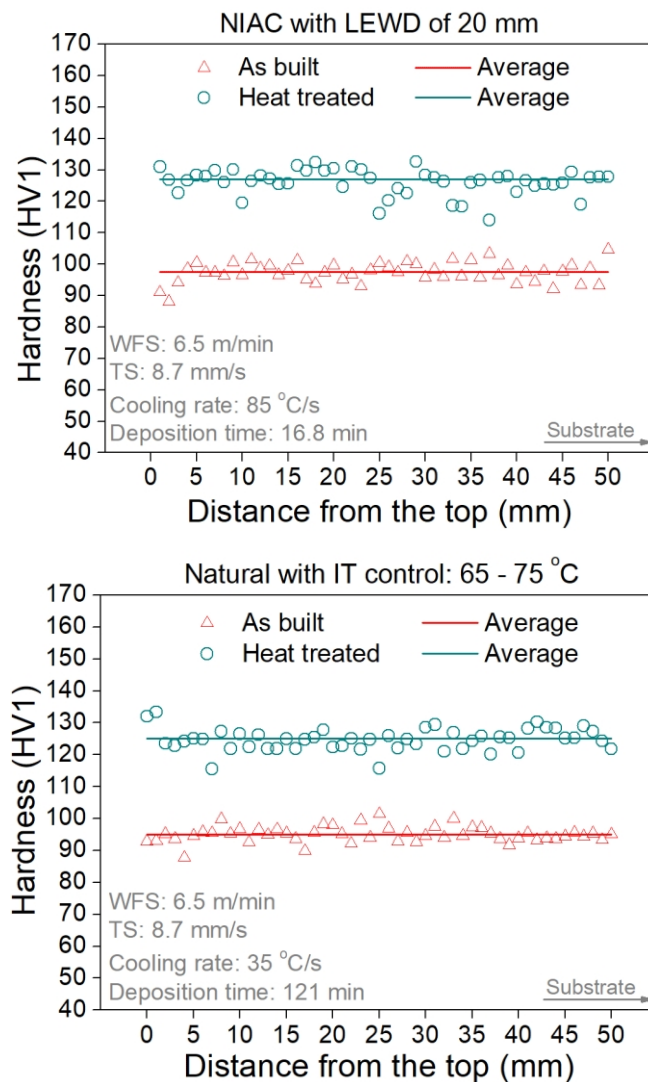

Figure 6.12. Hardness profiles performed along the height of samples of Scalmalloy® preforms produced by WAAM with the NIAC technique and the Natural cooling approach in the as built and heat-treated conditions

For all the conditions the precipitation response was positive, *i.e.*, the hardness increased significantly due to the heat treatment applied, as shown in Figure 6.13. Therefore, it can be said that most of the Sc that remained in solid solution during deposition successfully precipitated during the heat treatment. In addition, the hardness values found are comparable to those reported in the literature listed in Table 6.10.
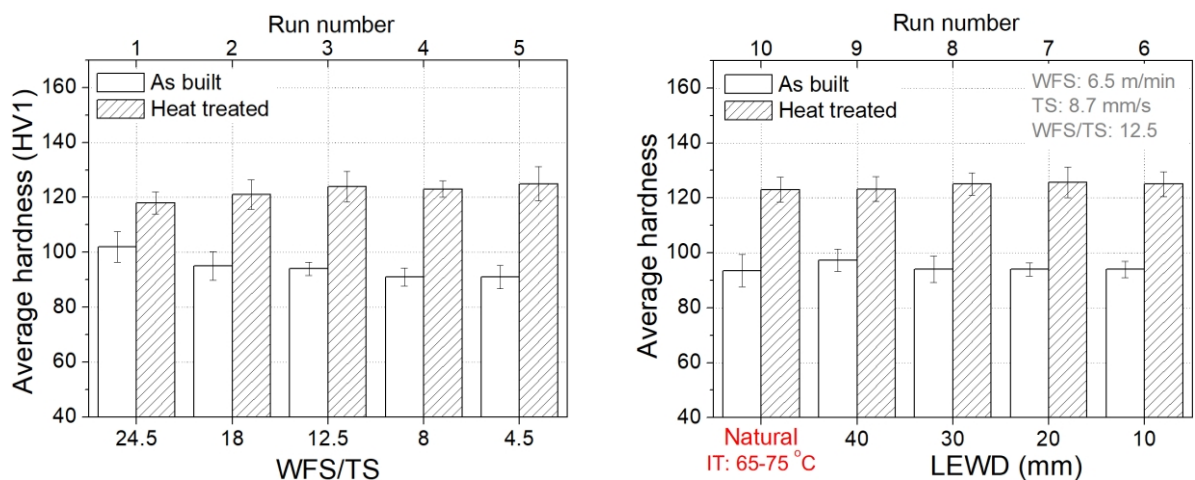
Figure 6.13. Average hardness of samples of Scalmalloy® preforms under the as-built and as the heat-treated conditions

Table 6.10. Hardness results reported in the literature for different Al-Sc alloys along with the correspondent processing techniques and heat treatment conditions

Reference	Chemical composition (wt%)	Processing technique	Aging treatment		Hardness as-built	Hardness as-aged
Lohar et al. (2010)	Al-0.3Sc-0.15Zr	casting	300 °C	3 h	44 HV10	71 HV10
Rometsch et al. (2014)	Al 0.9 wt.% Sc	DED-L	325 °C	2 h	34 HV5	65 HV5
Taendl et al. (2014)	Al-Mg4-Sc0.4-Zr0.15	casting	325 °C	1 h	82 HV0.1	105 HV0.1
Taendl et al. (2016)	Al-Mg4-Sc0.4-Zr0.12	Laser remelting	325 °C	3 h	64 HV0.1	110 HV0.1
Tang et al. (2017)	Al-0.2Sc and Al-0.4Sc	casting	300 °C	3 h	41 HV	60 HV
Spierings et al. (2017)	Al-4.6Mg-0.66Sc-0.42Zr 0.49Mn	PBF-L	325 °C	4 h	101 HB	144 HB
Shi et al. (2018)	Al-3.4Mg-1.08Sc-0.23Zr-0.5Mn-0.5Cu	PBF-L	300 °C	12 h	110 HV1	165 HV1
Zhao et al. (2018)	Al-4.55Mg-0.51Mn-0.65Sc-0.30Zr	DED-L	300 °C	3 h	110 HV10$_n$	145 HV10$_n$
Schmidtke et al. (2011)	Al-4.5Mg-0.66Sc-0.37Zr-0.51Mn	PBF-L	325 °C	4 h	105 HV0.3	175 HV0.3

Note: the average precipitation response was around 35%.

The effect of the cooling rate on the precipitation response is presented in Figure 6.14. The higher the cooling rate the greater the precipitation response, which corroborates the results presented by Taendl et al. (2016). The observed level of precipitation response is supported by the literature. Interestingly, the precipitation response of the Scalmalloy® preform deposited under the Natural cooling condition was comparable to those of the ones produced with the NIAC technique. Nevertheless, it is again worth mentioning that the deposition time without the NIAC was much longer, despite the resultant similar geometry, due to dwell time demanded.
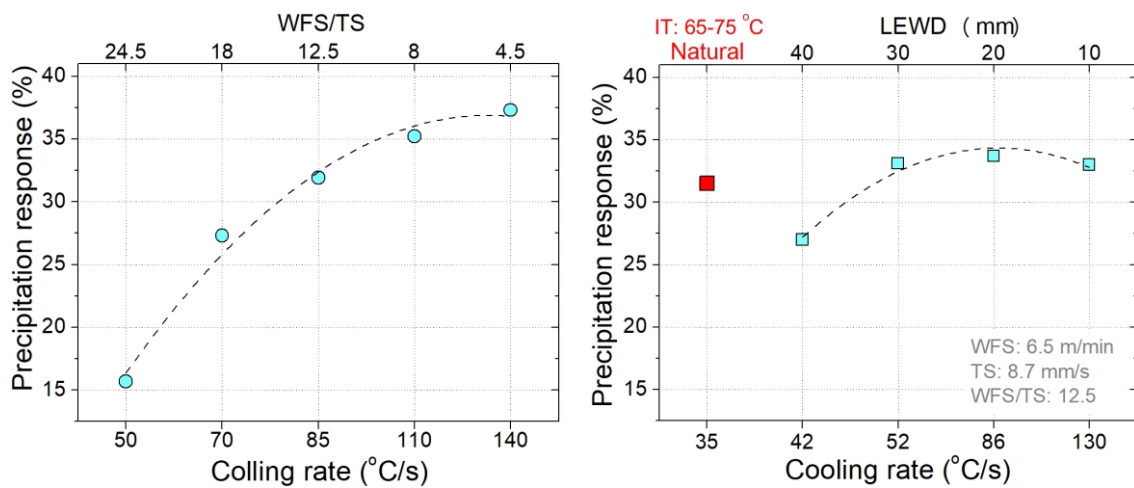
Figure 6.14. Effect of the cooling rate on the precipitation response of Scalmalloy® preforms (on the left side is the effect of the variation of the arc energy for a fixed LEWD value and on the right side is the effect of the variation of the LEWD for a fixed arc energy).

Despite the significant increase in hardness verified, no traces of scandium aluminides were identified in the diffraction patterns produced for the Scalmalloy® preforms (Figure 6.15). This fact could be explained by the limited content of this aluminide in the Al matrix, which is also commented by Zhang et al. (2018).
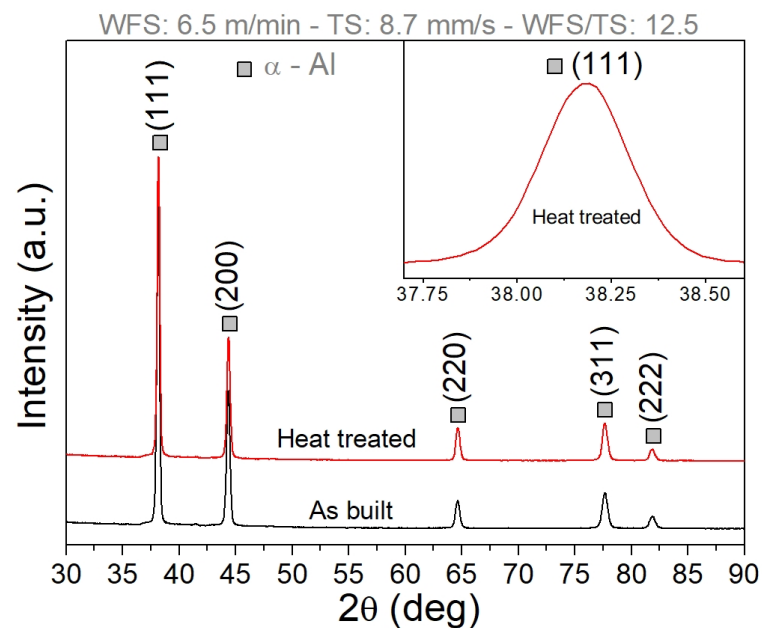
Figure 6.15. Typical XRD patterns of the samples of the Scalmalloy® preforms under the as-built and heat-treated conditions

6.5 Partial remarks

- Suitable Scalmalloy® preforms were produced by WAAM with the NIAC technique using parameters from the working envelope developed for the ER5356 wire;
- The resultant hardness profiles were almost flat, which means that no overaging occurred due to the thermal history imposed by WAAM;
- For all the conditions assessed the precipitation response was positive, *i.e.*, the hardness increased significantly due to heat treatment, but with the application of the NIAC technique the building productivity is always much higher; and
- The higher the cooling rate achieved in the preform, the greater the precipitation response.

CHAPTER VII - CLOSURE

7.1 General conclusions

Under the fundamental question on how to mitigate heat accumulation in WAAM as well as its potential deleterious consequences on the integrity of the preform and/or performance of the component without compromising the production and in a way applicable to most of the geometries as well as being environmentally sound, it was raised an hypothesis that if the preform was deposited near-immersed in water, then the heat accumulation would be uniformly mitigated without compromising production and operational performance of the component, provided that the water evaporation did not destabilize the process neither increased porosity. Therefore, the core objective of this thesis was to answer the fundamental question through the proof the raised hypothesis. The maturating process of the fundamental question with the raised hypothesis led to the establishment of the Research Questions (RQs) that could be translated into the specific objectives of the thesis. Throughout the research conducted during this doctorate thesis, the following answer can be drawn for each RQ:

RQ1: Is the NIAC technique able to effectively mitigate the heat accumulation in WAAM?

> ➢ Yes, it is. The high heat sink power of the NIAC technique can keep the preforms at lower temperatures during all the deposition time, independently of the preform height. Therefore, the NIAC technique has been proved as being able to effectively mitigate heat accumulation in WAAM of aluminum and, thus, to potentially cope with the related drawbacks.

RQ2: *Would the water evaporation destabilize the deposition process or generate porosity in WAAM of aluminum?*

> ➤ It depends on the layer-edge-to-water distance (LEWD). For a LEWD shorter than 10 mm the porosity tends to increase. For longer distances the use of water as the cooling liquid does not lead to any measurable increase in porosity. In general, the porosity in samples deposited with the NIAC with LEWD longer than 10 mm was like that of those deposited under the Natural cooling approach and both were in concordance with that reported in the current literature.

RQ3: *How to select deposition parameters for WAAM with the NIAC technique?*

> ➤ A procedure for parameter selection that considers surface quality was proposed and experimentally validated. According to this procedure, for non-expensive and easy-to-machine materials a moderated surface waviness (SW) is acceptable, then the parameters for higher production can selected directly from the working envelope that was developed. In contrast, for high-cost and difficult-to-machine materials a minimum SW is required, then an empirical modeling and a numerical optimization should be performed to meet a target geometry with a minimum SW simultaneously.

RQ4: *Is it feasible to deposit Scalmalloy® parts by WAAM with the NIAC technique?*

> ➤ Yes, it is. Suitable Scalmalloy® preforms were produced by WAAM and with better productivity with the NIAC. The flat hardness profile along the height of these preforms indicated that overaging did not take place. Moreover, the hardness increased significantly on the heat-treated samples, indicating that Sc was retained in a supersaturated solid solution during deposition. Unlike expected and reported in the literature, the samples deposited under the Natural cooling approach (air convection) showed a similar behavior. However, is worth mentioning that the deposition time in this case was much longer, despite the similar geometry achieve for the preform, due to demanded dwell time.

7.2 Thesis contributions

The main contributions of this thesis are listed below:

- Development of a thermal management technique with low cost and of easy adaptation to WAAM equipment, of high efficiency and capable of being potentially applicable to most materials and geometries;
- The NIAC technique was able to increase the WAAM productivity by reducing the cooling time in between the layers and enabled to continuously deposit small components and/or features;
- Demonstration that if the same interpass temperature is maintained, the preform geometry tends to be similar independently of the thermal management technique applied, but the deposition time will be different;
- Development of a procedure for selecting WAAM parameters for a target geometry and considering surface quality; and
- Demonstration that suitable Scalmalloy® preforms can be deposited by WAAM with support of the NIAC technique.

7.3 The NIAC limitations

The following limitations can be drawn concerning the implementation of the NIAC concept:

- DED process with the NIAC technique are limited to a flat building position. Therefore, especially in multi-axis manufacturing systems with a moving worktable, other cooling strategies should be applied;
- The thermal management system as developed does not control the water temperature;
- Although the magnetic float switch fulfills the goal of controlling the water level, for more complex preform geometries it could shock against the preform. Therefore, another level sensor should be used in an industrial application, for example, a capacitive one; and

- The temperature measurement of the workpiece with a pyrometer, as carried out, may be limited to simple geometries, as the pyrometer may miss the target in more complex geometries.

7.4 Proposal for future work

Aiming at further improvement of the NIAC technique, the following future work are proposed:

- To use the experimental data raised in this work to validate numerical simulations aiming at the understanding of the NIAC technique in a broader spectrum, especially regarding thermomechanical aspects;
- To develop a LEWD control system based on the preform temperature;
- By controlling the LEWD and water temperature, to build components with tailored microstructure and properties; and
- To assess the NIAC technique as a means of using even higher deposition processes, such as double-wire GMA.

REFERENCES

Aboulkhair, N.T., Simonelli, M., Parry, L., Ashcroft, I., Tuck, C., Hague, R., 2019. Progress in Materials Science 3D printing of Aluminium alloys : Additive Manufacturing of Aluminium alloys using selective laser melting. Prog. Mater. Sci. 100578. https://doi.org/10.1016/j.pmatsci.2019.100578

Adams, R.J., 2005. Solid-free-form fabrication process and apparatus including in-process workpiece cooling. US7326377B2.

Additive Manufacturing UK National Strategy 2018-2025, 2018. Report. https://doi.org/http://www.amnationalstrategy.uk/

Albrecht, B.P., Hsu, C., 2014. Additive manufacturing heating control systems and methods. US20150021815A1.

Ali, Y., Henckell, P., Hildebrand, J., Reimann, J., Bergmann, J.P., 2019. Wire arc additive manufacturing of hot work tool steel with CMT process. J. Mater. Process. Tech. 269, 109–116. https://doi.org/10.1016/j.jmatprotec.2019.01.034

Almeida, P.M.S., Williams, S., 2010. Innovative Process Model of Ti-6Al-4V Additive Layer Manufacturing Using Cold Metal Transfer (CMT), in: International Solid Freeform Fabrication Symposion. Austin, Tx, pp. 25–36.

APWorks, 2017. Scalmalloy ® Parameter setting Implementation schedule [WWW Document]. URL https://apworks.de/

ASTM, 2016. ASTM F3187 - 16 - Standard Guide for Directed Energy Deposition of Metals. ASTM Int. 1–22. https://doi.org/10.1520/F3187

Brandt, R., Bird, C., Neuer, G., 2008. Emissivity reference paints for high temperature applications. Meas. J. Int. Meas. Confed. 41, 731–736. https://doi.org/10.1016/j.measurement.2007.10.007

Cao, Y., Li, H., Liang, Z., Wang, D., 2017. Effect of Water Cooling on the Microstructure and Mechanical Properties of 6N01 Aluminum Alloy P-MIG-Welded Joints. J. Mater. Eng. Perform. 26, 3929–3938. https://doi.org/10.1007/s11665-017-2792-6

Cunningham, C.R., Flynn, J.M., Shokrani, A., Dhokia, V., Newman, S.T., 2018. Invited review article : Strategies and processes for high quality wire arc additive manufacturing. Addit. Manuf. 22, 672–686. https://doi.org/10.1016/j.addma.2018.06.020

Da Silva, C.L.M., Scotti, A., 2006. The influence of double pulse on porosity formation in aluminum GMAW. J. Mater. Process. Technol. 171, 366–372. https://doi.org/10.1016/j.jmatprotec.2005.07.008

Debroy, T., Wei, H.L., Zuback, J.S., Mukherjee, T., Elmer, J.W., Milewski, J.O., Beese, A.M., Wilson-heid, A., De, A., Zhang, W., 2018. Progress in Materials Science Additive manufacturing of metallic components – Process , structure and properties. Prog. Mater. Sci. 92, 112–224. https://doi.org/10.1016/j.pmatsci.2017.10.001

Denlinger, E.R., Heigel, J.C., Michaleris, P., 2015a. Residual stress and distortion modeling of electron beam direct manufacturing Ti-6Al-4V. Proc. Inst. Mech. Eng. Part B J. Eng. Manuf. 229, 1803–1813. https://doi.org/10.1177/0954405414539494

Denlinger, E.R., Heigel, J.C., Michaleris, P., Palmer, T.A., 2015b. Effect of inter-layer dwell time on distortion and residual stress in additive manufacturing of titanium and nickel alloys. J. Mater. Process. Technol. 215, 123–131. https://doi.org/10.1016/j.jmatprotec.2014.07.030

Derekar, K., Lawrence, J., Melton, G., Addison, A., Zhang, X., Xu, L., 2018. Influence of interpass temperature on wire arc additive manufacturing (WAAM) of aluminium, in: The 71st IIW Annual Assemply and International Conference. IIW, Bali.

Digital Alloys, 2019. Powder Bed Fusion [WWW Document]. Blog. URL https://www.digitalalloys.com/

Ding, D., Pan, Z., Cuiuri, D., Li, H., 2015. Wire-feed additive manufacturing of metal components: technologies, developments and future interests. Int. J. Adv. Manuf. Technol. 81, 465–481. https://doi.org/10.1007/s00170-015-7077-3

DMG-MORI, 2019. Additive Manufacturing machines [WWW Document]. wesite. URL https://en.dmgmori.com/products/machines/additive-manufacturing/powder-nozzle

Dutta, B., 2016. Method of high rate direct material deposition. US20160271732A1.

Farshidianfar, M.H., Khajepour, A., Gerlich, A., 2016. Real-time control of microstructure in laser additive manufacturing. Int. J. Adv. Manuf. Technol. 82, 1173–1186. https://doi.org/10.1007/s00170-015-7423-5

Fayolle, R.C., 2016. Cryogenic coolig of Wire Arc Additive Manufacturing.

Fischer, G., RÖHRICH, T., Haschke, I., 2015. Method for the additive production of a shaped body. EP3069804A2.

Foster, B.K., Beese, A.M., Keist, J.S., McHale, E.T., Palmer, T.A., 2017. Impact of Interlayer Dwell Time on Microstructure and Mechanical Properties of Nickel and Titanium Alloys. Metall. Mater. Trans. A Phys. Metall. Mater. Sci. 48, 4411–4422. https://doi.org/10.1007/s11661-017-4164-0

Frazier, W.E., 2014. Metal Additive Manufacturing : A Review 23, 1917–1928. https://doi.org/10.1007/s11665-014-0958-z

Fronius, 2014. Current welding practice: CMT Technology, 1st ed. Dusseldorf.

Geng, H., Li, J., Xiong, J., Lin, X., 2017. Optimisation of interpass temperature and heat input for wire and arc additive manufacturing 5A06 aluminium alloy. Sci. Technol. Weld. Join. 22, 472–483. https://doi.org/10.1080/13621718.2016.1259031

Gibison, I., Rosen, D.W., Stucker, B., 2010. Manufacturing, Additive Manufacturing Technologies: Rapid Portotypign to Direct Digital. Springer, New York. https://doi.org/10.1007/978-1-4419-1120-9

Gu, J., Ding, J., Williams, S.W., Gu, H., Ma, P., 2016. The effect of inter-layer cold working and post-deposition heat treatment on porosity in additively manufactured aluminum alloys. J. Mater. Process. Technol. 230, 26–34. https://doi.org/https://doi.org/10.1016/j.jmatprotec.2015.11.006

Guo, G., 2017. Electron beam fuse wire additive manufacturing device and control method thereof. CN107498043A.

Hagqvist, P., Sikström, F., Christiansson, A.K., 2013. Emissivity estimation for high temperature radiation pyrometry on Ti-6Al-4V. Meas. J. Int. Meas. Confed. 46, 871–880. https://doi.org/10.1016/j.measurement.2012.10.019

Haselhuhn, A.S., Buhr, M.W., Wijnen, B., Sanders, P.G., Pearce, J.M., 2016. Materials Science & Engineering A Structure-property relationships of common aluminum weld alloys utilized as feedstock for GMAW-based 3-D metal printing. Mater. Sci. Eng. A 673, 511–523. https://doi.org/10.1016/j.msea.2016.07.099

Henckell, P., Günther, K., Ali, Y., Bergmann, J.P., Scholz, J., Forêt, P., 2017a. The Influence of Gas Cooling in Context of Wire Arc Additive Manufacturing---A Novel Strategy of Affecting Grain Structure and Size, in: TMS The Minerals, M.& M.S. (Ed.), TMS 2017 146th Annual Meeting & Exhibition Supplemental Proceedings. Springer International Publishing, Cham, pp. 147–156.

Henckell, P., Günther, K., Ali, Y., Bergmann, J.P., Scholz, J., Forêt, P., 2017b. The In fl uence of Gas Cooling in Context of Wire Arc Additive Manufacturing - A Novel Strategy of Affecting Grain Structure and Size. TMS Miner. 147–156. https://doi.org/10.1007/978-3-319-51493-2

Herzog, D., Seyda, V., Wycisk, E., Emmelmann, C., 2016. Additive manufacturing of metals. Acta Mater. 117, 371–392. https://doi.org/10.1016/j.actamat.2016.07.019

Horgar, A., Fostervoll, H., Nyhus, B., Ren, X., Eriksson, M., Akselsen, O.M., 2018. Additive manufacturing using WAAM with AA5183 wire. J. Mater. Process. Tech. 259, 68–74. https://doi.org/10.1016/j.jmatprotec.2018.04.014

ISO/ASTM International, 2015. Standard Terminology for Additive Manufacturing – General Principles – Terminology. ISO/ASTM 52900. https://doi.org/10.1520/F2792-12A.2

Jamshidinia, M., Kovacevic, R., 2015. The influence of heat accumulation on the surface roughness in powder-bed additive manufacturing. Surf. Topogr. Metrol. Prop. 3, 14003. https://doi.org/10.1088/2051-672X/3/1/014003

Jia, Q., Rometsch, P., Cao, S., Zhang, K., Wu, X., 2019. Towards a high strength aluminium alloy development methodology for selective laser melting. Mater. Des. 174, 107775. https://doi.org/10.1016/j.matdes.2019.107775

Jiang, R., Kleer, R., Piller, F.T., 2017. Predicting the future of additive manufacturing : A Delphi study on economic and societal implications of 3D printing for 2030. Technol. Forecast. Soc. Chang. 117, 84–97. https://doi.org/10.1016/j.techfore.2017.01.006

Jorge, V.L., Gohrs, R., Scotti, A., 2017. Active power measurement in arc welding and its role in heat transfer to the plate 847–856. https://doi.org/10.1007/s40194-017-0470-9

Karlen, E., 2016. Thermal control for additive manufacturing. US20170355019A1.

Kellens, K., Mertens, R., Paraskevas, D., Dewulf, W., Duflou, J.R., 2017. Environmental Impact of Additive Manufacturing Processes : Does AM contribute

to a more sustainable way of part manufacturing ? Procedia CIRP 61, 582–587. https://doi.org/10.1016/j.procir.2016.11.153

Koksoy, O., Yalcinoz, T., 2006. Mean square error criteria to multiresponse process optimization by a new genetic algorithm. Appl. Math. Comput. 175, 1657–1674. https://doi.org/10.1016/j.amc.2005.09.011

Kou, S., 2002. Welding Metallurgy, 2nd ed. Wiley, New Jersey.

Larrosa, N.O., Wang, W., Read, N., Loretto, M.H., Evans, C., Carr, J., Tradowsky, U., Attallah, M.M., Withers, P.J., 2018. Linking microstructure and processing defects to mechanical properties of selectively laser melted AlSi10Mg alloy. Theor. Appl. Fract. Mech. 98, 123–133. https://doi.org/10.1016/j.tafmec.2018.09.011

Lei, Y., Xiong, J., Li, R., 2018. Effect of inter layer idle time on thermal behavior for multi-layer single-pass thin-walled parts in GMAW-based additive manufacturing. Int. J. Adv. Manuf. Technol. 96, 1355–1365. https://doi.org/10.1007/s00170-018-1699-1

Li, F., 2018. Thermoelectric Cooling-Aided Bead Geometry Regulation in Wire and Arc-Based Additive Manufacturing of Thin-Walled Structures. Appl. Sci. 8, 207. https://doi.org/10.3390/app8020207

Li, F., Chen, S., Shi, J., Zhao, Y., Tian, H., 2018. Thermoelectric Cooling-Aided Bead Geometry Regulation in Wire and Arc-Based Additive Manufacturing of Thin-Walled Structures. Appl. Sci. 8, 207. https://doi.org/10.3390/app8020207

Li, R., Chen, H., Zhu, H., Wang, M., Chen, C., Yuan, T., 2019. Effect of aging treatment on the microstructure and mechanical properties of Al-3 . 02Mg-0 . 2Sc-0 . 1Zr alloy printed by selective laser melting. Mater. Des. 168, 107668. https://doi.org/10.1016/j.matdes.2019.107668

Lockett, H., Ding, J., Williams, S., Martina, F., Lockett, H., 2017. Design for Wire + Arc Additive Manufacture : design rules and build orientation selection Design for Wire + Arc Additive Manufacture : design rules and build orientation selection 4828. https://doi.org/10.1080/09544828.2017.1365826

Lohar, A.K., Mondal, B.N., Panigrahi, S.C., 2010. Journal of Materials Processing Technology Influence of cooling rate on the microstructure and ageing behavior of as-cast Al – Sc – Zr alloy. J. Mater. Process. Tech. 210, 2135–2141. https://doi.org/10.1016/j.jmatprotec.2010.07.035

Lu, X., Zhou, Y.F., Xing, X.L., Shao, L.Y., Yang, Q.X., Gao, S.Y., 2017. Open-source wire and arc additive manufacturing system: formability, microstructures, and mechanical properties. Int. J. Adv. Manuf. Technol. 93, 2145–2154. https://doi.org/10.1007/s00170-017-0636-z

LumaSense, 2019. Infrared Thermometer Handbook.

Ma, Y., Cuiuri, D., Shen, C., Li, H., Pan, Z., 2015. Effect of interpass temperature on in-situ alloying and additive manufacturing of titanium aluminides using gas tungsten arc welding. Addit. Manuf. 8, 71–77. https://doi.org/10.1016/j.addma.2015.08.001

Manvatkar, V., De, A., Debroy, T., 2014. Heat transfer and material flow during laser assisted multi-layer additive manufacturing. J. Appl. Phys. 116, 1–8. https://doi.org/10.1063/1.4896751

Martina, F., Mehnen, J., Williams, S.W., Colegrove, P., Wang, F., 2012. Journal of Materials Processing Technology Investigation of the benefits of plasma deposition for the additive layer manufacture of Ti – 6Al – 4V. J. Mater. Process. Tech. 212, 1377–1386. https://doi.org/10.1016/j.jmatprotec.2012.02.002

Naware, G.N., 2014. Selective zone temperature control build plate. US20160096326A1.

Norrish, J., Cuiuri, D., 2014. The controlled short circuit GMAW process : A tutorial. J. Manuf. Process. 16, 86–92. https://doi.org/10.1016/j.jmapro.2013.08.006

Norsk Titanium, 2019. Rapid plasma depostion [WWW Document]. URL https://www.norsktitanium.com/

Pan, Z., Ding, D., Wu, B., Cuiuri, D., Li, H., Norrish, J., 2017. Arc Welding Processes for Additive Manufacturing : A Review. Trans. Intell. Weld. Manuf. 13–20. https://doi.org/https://doi.org/10.1007/978-981-10-5355-9_1

Peretti, M.W., Trapp, T., 2010. High temperature additive manufacturing systems for making near net shape airfoils leading edge protection, and tooling systems therewith. US20100242843A1.

Plotkowski, A., Rios, O., Sridharan, N., Sims, Z., Unocic, K., Ott, R.T., 2017. Evaluation of an Al-Ce alloy for laser additive manufacturing. Acta Mater. 126, 507–519. https://doi.org/10.1016/j.actamat.2016.12.065

Reis, R.P., Scotti, A., Silva, L.J. da, 2018. Active Cooling Technique for Additive Manufacturing.

Ríos, S., Colegrove, P.A., Martina, F., Williams, S.W., 2018. Analytical process model for wire + arc additive manufacturing. Addit. Manuf. 21, 651–657. https://doi.org/10.1016/j.addma.2018.04.003

Rodrigues, T.A., Duarte, V., Miranda, R.M., Santos, T.G., Oliveira, J.P., 2019. Current Status and Perspectives on Wire and Arc Additive Manufacturing (WAAM). Materials (Basel). https://doi.org/10.3390/ma12071121

Rometsch, P.A., Zhong, H., Nairn, K.M., Wu, X., 2014. Characterization of a laser-fabricated hypereutectic Al – Sc alloy bar. Scr. Mater. 87, 13–16. https://doi.org/10.1016/j.scriptamat.2014.05.021

Røyset, J., Ryum, N., 2005. Scandium in aluminium alloys 50, 19–44. https://doi.org/10.1179/174328005X14311

Ryan, E.M., Sabin, T.J., Watts, J.F., Whiting, M.J., 2018. The in fl uence of build parameters and wire batch on porosity of wire and arc additive manufactured aluminium alloy 2319. J. Mater. Process. Tech. 262, 577–584. https://doi.org/10.1016/j.jmatprotec.2018.07.030

Schmidtke, K., Palm, F., Hawkins, A., Emmelmann, C., 2011. Process and Mechanical Properties : Applicability of a Scandium modified Al-alloy for Laser Additive Manufacturing. Phys. Procedia 12, 369–374. https://doi.org/10.1016/j.phpro.2011.03.047

Shen, C., Pan, Z., Cuiuri, D., Ding, D., Li, H., 2017. Influences of deposition current and interpass temperature to the Fe3Al-based iron aluminide fabricated using wire-arc additive manufacturing process. Int. J. Adv. Manuf. Technol. 88, 2009–2018. https://doi.org/10.1007/s00170-016-8935-3

Shi, Y., Yang, K., Kairy, S.K., Palm, F., Wu, X., Rometsch, P.A., 2018. Effect of platform temperature on the porosity , microstructure and mechanical properties of an Al – Mg – Sc – Zr alloy fabricated by selective laser melting. Mater. Sci. Eng. A 732, 41–52. https://doi.org/10.1016/j.msea.2018.06.049

Silva, L.J., Reis, R.P., Scotti, A., 2019. The Potential of IR Pyrometry for Monitoring Interpass Temperature in Wire + Arc Additive Manufacturing. Evol. Mech. Eng. 1–4. https://doi.org/10.31031/EME.2019.03.000553

SLM Solutions, 2019. Case Report: Monolithic Thrust Chamber [WWW Document]. URL https://www.slm-solutions.com/fileadmin/user_upload/downloads/en/433EN19-05-

CellCore_web.pdf

SmarTech, 2018. Markets for Aluminum Alloys in Additive Manufacturing: 2018 to 2028. https://doi.org/https://www.smartechanalysis.com/reports/aluminum-alloys-am-18-2028/

Spierings, A.B., Dawson, K., Dumitraschkewitz, P., Pogatscher, S., Wegener, K., 2018. Microstructure characterization of SLM-processed Al-Mg-Sc-Zr alloy in the heat treated and HIPed condition. Addit. Manuf. 20, 173–181. https://doi.org/10.1016/j.addma.2017.12.011

Spierings, A.B., Dawson, K., Kern, K., Palm, F., Wegener, K., 2017. SLM-processed Sc- and Zr- modified Al-Mg alloy: Mechanical properties and microstructural effects of heat treatment. Mater. Sci. Eng. A 701, 264–273. https://doi.org/10.1016/j.msea.2017.06.089

Spierings, A.B., Schneider, M., 2011. Comparison of density measurement techniques for additive manufactured metallic parts. Rapid Prototyp. J. https://doi.org/10.1108/13552541111156504

Storn, R., Price, K., 1996. Differential Evolution - A simple and efficient adaptive scheme for global optimization over continuous spaces. https://doi.org/http://www1.icsi.berkeley.edu

Taendl, J., Orthacker, A., Amenitsch, H., Kothleitner, G., Poletti, C., 2016. Influence of the degree of scandium supersaturation on the precipitation kinetics of rapidly solidi fi ed Al-Mg-Sc-Zr alloys. Acta Mater. 117. https://doi.org/10.1016/j.actamat.2016.07.001

Taendl, J., Palm, F., Anders, K., Gradinger, R., Poletti, C., 2014. Investigation of the precipitation kinetics of a new Al-Mg-Sc-Zr alloy 796, 1038–1043. https://doi.org/10.4028/www.scientific.net/MSF.794-796.1038

Tang, Y., Liao, H., Liu, Y., 2017. Precipitation of ScAl 3 Phase During Solutionizing and Ageing of Hypoeutectic Al-Sc Alloys and its Impact to Mechanical Properties 877, 581–586. https://doi.org/10.4028/www.scientific.net/MSF.877.581

Thomas-Seale, L.E.J., Kirkman-brown, J.C., Attallah, M.M., Espino, D.M., Shepherd, D.E.T., 2018. International Journal of Production Economics The barriers to the progression of additive manufacture : Perspectives from UK industry. Int. J. Prod. Econ. 198, 104–118. https://doi.org/10.1016/j.ijpe.2018.02.003

Toda, H., Hidaka, T., Kobayashi, M., Uesugi, K., Takeuchi, A., Horikawa, K., 2009.

Growth behavior of hydrogen micropores in aluminum alloys during high-temperature exposure. Acta Mater. 57, 2277–2290. https://doi.org/10.1016/j.actamat.2009.01.026

TWI, 2019. WHAT IS ADDITIVE MANUFACTURING? - DEFINITION AND PROCESSES [WWW Document]. URL https://www.twi-global.com/technical-knowledge/faqs/what-is-additive-manufacturing

Wang, H., Jiang, W., Ouyang, J., Kovacevic, R., 2004. Rapid prototyping of 4043 Al-alloy parts by VP-GTAW. J. Mater. Process. Technol. 148, 93–102. https://doi.org/10.1016/j.jmatprotec.2004.01.058

Wang, J.F., Sun, Q.J., Wang, H., Liu, J.P., Feng, J.C., 2016. Effect of location on microstructure and mechanical properties of additive layer manufactured Inconel 625 using gas tungsten arc welding. Mater. Sci. Eng. A 676, 395–405. https://doi.org/10.1016/j.msea.2016.09.015

Williams, S.W., Martina, F., Addison, A.C., Ding, J., Pardal, G., Colegrove, P., 2016. Wire + Arc Additive Manufacturing. Mater. Sci. Technol. 32, 641–647. https://doi.org/10.1179/1743284715Y.0000000073

Wohlers Report 2019, 2019. Wohlers Report 2019. https://doi.org/https://wohlersassociates.com/2019report.htm

Wu, B., Ding, D., Pan, Z., Cuiuri, D., Li, H., Han, J., Fei, Z., 2017. Effects of heat accumulation on the arc characteristics and metal transfer behavior in Wire Arc Additive Manufacturing of Ti6Al4V. J. Mater. Process. Technol. 250, 304–312. https://doi.org/10.1016/j.jmatprotec.2017.07.037

Wu, B., Pan, Z., Ding, D., Cuiuri, D., Li, H., Fei, Z., 2018. The effects of forced interpass cooling on the material properties of wire arc additively manufactured Ti6Al4V alloy. J. Mater. Process. Technol. 258, 97–105. https://doi.org/10.1016/j.jmatprotec.2018.03.024

Xiong, J., Lei, Y., Chen, H., Zhang, G., 2017. Fabrication of inclined thin-walled parts in multi-layer single-pass GMAW-based additive manufacturing with flat position deposition. J. Mater. Process. Technol. 240, 397–403. https://doi.org/10.1016/j.jmatprotec.2016.10.019

Xiong, J., Zhang, G., 2014. Adaptive control of deposited height in GMAW-based layer additive manufacturing. J. Mater. Process. Technol. 214, 962–968. https://doi.org/10.1016/j.jmatprotec.2013.11.014

Xiong, J., Zhang, G., Qiu, Z., Li, Y., 2013. Vision-sensing and bead width control of a single-bead multi-layer part: Material and energy savings in GMAW-based rapid manufacturing. J. Clean. Prod. 41, 82–88. https://doi.org/10.1016/j.jclepro.2012.10.009

Xiong, J., Zhang, G., Zhang, W., 2015. Forming appearance analysis in multi-layer single-pass GMAW-based additive manufacturing. Int. J. Adv. Manuf. Technol. 80, 1767–1776. https://doi.org/10.1007/s00170-015-7112-4

Xiong, Z.Q., Zhou, X., Wang, Y., Qing, Z., 2015. Partial temperature control system for metal material 3D printing. CN104959606A.

Xu, X., Ding, J., Ganguly, S., Diao, C., Williams, S., 2018. Oxide accumulation effects on wire + arc layer-by-layer additive manufacture process. J. Mater. Process. Technol. 252, 739–750. https://doi.org/10.1016/j.jmatprotec.2017.10.030

YANAGIDA, N., KOIDE, H., 2008. Reduction of Residual Stress in Multi-layer Welded Plates by Applying Water-shower Cooling During Welding. J. Solid Mech. Mater. Eng. 2, 943–954. https://doi.org/10.1299/jmmp.2.943

Yang, D., Wang, G., Zhang, G., 2017. Thermal analysis for single-pass multi-layer GMAW based additive manufacturing using infrared thermography. J. Mater. Process. Technol. 244, 215–224. https://doi.org/10.1016/j.jmatprotec.2017.01.024

Yang, K. V, Shi, Y., Palm, F., Wu, X., Rometsch, P., 2018. Scripta Materialia Columnar to equiaxed transition in Al-Mg (-Sc) -Zr alloys produced by selective laser melting. Scr. Mater. 145, 113–117. https://doi.org/10.1016/j.scriptamat.2017.10.021

Yehorov, Y., Silva, L.J. da, Scotti, A., 2019. Balancing WAAM Production Costs and Wall Surface Quality through Parameter Selection : A Case Study of an Al-Mg5 Alloy Multilayer-Non-Oscillated Single. J. Manuf. Mater. Process. Artic. https://doi.org/https://doi.org/10.3390/jmmp3020032

Zhang, C., Li, Y., Gao, M., Zeng, X., 2018. Wire arc additive manufacturing of Al-6Mg alloy using variable polarity cold metal transfer arc as power source. Mater. Sci. Eng. A 711, 415–423. https://doi.org/10.1016/j.msea.2017.11.084

Zhang, H., Gu, D., Yang, J., Dai, D., Zhao, T., Hong, C., 2018. Selective laser melting of rare earth element Sc modi fi ed aluminum alloy : Thermodynamics of precipitation behavior and its in fl uence on mechanical properties 23, 1–12.

https://doi.org/10.1016/j.addma.2018.07.002

Zhao, T., Cai, W., Dahmen, M., Schaible, J., Hong, C., Gasser, A., Weisheit, A., Biermann, T., Kelbassa, I., Zhang, H., Gu, D., Henrich, J., 2018. Ageing response of an Al-Mg-Mn-Sc-Zr alloy processed by laser metal deposition in thin-wall structures. Vacuum 158, 121–125. https://doi.org/10.1016/j.vacuum.2018.09.052

Zou, J., Gaber, Y., Voulazeris, G., Li, S., Vazquez, L., Liu, L.F., Yao, M.Y., Wang, Y.J., Holynski, M., Bongs, K., Attallah, M.M., 2018. Controlling the grain orientation during laser powder bed fusion to tailor the magnetic characteristics in a Ni-Fe based soft magnet. Acta Mater. 158, 230–238. https://doi.org/10.1016/j.actamat.2018.07.064